ABSTRACT

COMPOSITE PARTICLE PRODUCTION
IN INTERMEDIATE ENERGY HEAVY ION COLLISIONS

By

Michael William Curtin

In this thesis, we present experimental and theoretical studies of composite fragment production in intermediate energy heavy ion collisions. Inclusive yield measurements were undertaken to differentiate between the various theoretical approaches. The reaction $^{14}N + ^{nat}Ag$ at incident energies of 20A, 30A, and 35A MeV leading to complex fragments in the range $3 \leq Z \leq 24$ was examined. Our theoretical studies had suggested that the production cross sections of such complex fragments might provide evidence for the occurrence of a liquid-gas phase transition in nuclear systems. Since other reactions mechanisms also lead to complex fragment production, these processes were also investigated.

The coalescence and thermal models, for example, predict complex fragment cross sections that depend on the proton production cross section raised to the power A, where A is the mass of the complex fragment. This formalism underpredicts our measured yields, but the discrepancy can be explained by other models. Several of these approaches are discussed, including Compound Nucleus Fission,

Cold Shattering of the Spectator, Mechanical Instability, a Coulomb Tunneling Model, as well as the Liquid-Gas Phase Transition. Possible applications of percolation theory, which also predict critical behavior, are discussed. The nonthermal nature of this theory, and related ramifications, could make it an important approach for nuclear collisions where the degree of thermalization is still a topic of current debate. The time scales are discussed as are several complicating experimental caveats.

The experimental data indicate that further experiments are required before a definitive conclusion can be reached regarding the occurrence of critical phenomena such as predicted in the phase transition theories. Our results suggest that further experiments on heavy ion reactions are necessary in the energy range 40A MeV $\leq E_{inc} \leq$ 100A MeV.

The critical behavior discussed in this thesis is less exotic than the phase transitions conjectured to occur at much higher incident energies, for example when hadronic matter is compressed and heated to a quark-gluon plasma. The significance of this work rests on the fact that it may help in understanding the conditions relating to this more exotic behavior and, in doing so, lead us to experimentally accessible signatures.

COMPOSITE PARTICLE PRODUCTION
IN INTERMEDIATE ENERGY HEAVY ION COLLISIONS

By

Michael William Curtin

A DISSERTATION

Submitted to
Michigan State University
in partial fulfillment of the requirements
for the degree of

DOCTOR OF PHILOSOPHY

Department of Physics and Astronomy

1985

ACKNOWLEDGMENTS

I would like to take this opportunity to express my deep gratitude to my mentor and friend Dr. David K. Scott for his guidance and support throughout this endeavor. I would also like to thank my close personal friend Dr. Hiroshi Toki for his guidance regarding the theoretical portion of this thesis. A collective "thanks" is in order to these individuals for one of the most challenging and rewarding pursuits of my life.

C.K. Gelbke deserves a special thanks for his willingness to advise me on many aspects of research. I would also like to thank my colleagues N. Anantaraman, S. Angius, G.F. Bertsch, D. Boal, C.B. Chitwood, G. Crawley, D. Fields, W. Friedman, C. Guet, L. Harwood, B. Hasselquist, B.V. Jacak, D. Klesch, Z.M. Koenig, R. Legrain, W.G. Lynch, M. Maier, A.D. Panagiotou, B. Pope, L. Richardson, O. Scholten, P.J. Siemens, H. Stoecker, T.J.M. Symons, M.B. Tsang, G.D. Westfall, and J.S. Winfield for their support during my graduate studies. For the facilities and support of NSCL, I am particularly grateful to Dr. Sam Austin and Dr. Henry Blosser and all the staff of NSCL who helped make this work a reality. I would also like to express my thanks and best wishes to all my fellow graduate students.

A special thank you is extended to my brother, Mark, for his constant support and for convincing me to undertake this thesis. For their constant love and understanding, I would like to thank my mother and father, brothers and sisters, my wife, Pat, and our children, Jim and Tracy.

I would also like to thank the James Balark family for all the love and encouragement during the course of this thesis.

TABLE OF CONTENTS

CHAPTER Page

LIST OF TABLES

LIST OF FIGURES

CHAPTER 1

INTRODUCTION

The primary motivation for the present endeavor is the interest in the equation of state of nuclear matter under extreme conditions of temperature and density. Figure 1.1 depicts the anticipated behavior of nuclear matter as a function of temperature, T, and density, ρ (CUG 84a). The current state of knowledge is restricted to essentially two points: (ρ_0, T = 0), i.e. normal nuclear density and zero temperature corresponding to the cold nuclear matter comprising nuclei of the matter around us; and the physically uninteresting, extremely dilute nuclear gas of (ρ = 0, T = 0). In light of the present knowledge, or lack thereof, it is most instructive to delineate boundaries where the domination of one aspect of physics gives way to another, thus resulting in a phase transition. Figure 1.1 denotes the current estimates of where the ambient temperature and density are sufficiently large that composite nuclear systems (liquid droplets) are no longer stable, resulting in a phase transition from a liquid to a hadronic gas composed primarily of individual nucleons. Further increases in density could result in the formation of free pions as opposed to the virtual pions familiar as a mediator of the nuclear force at low energy. Still further increases in temperature and density may liberate the constituent quarks and gluons comprising the

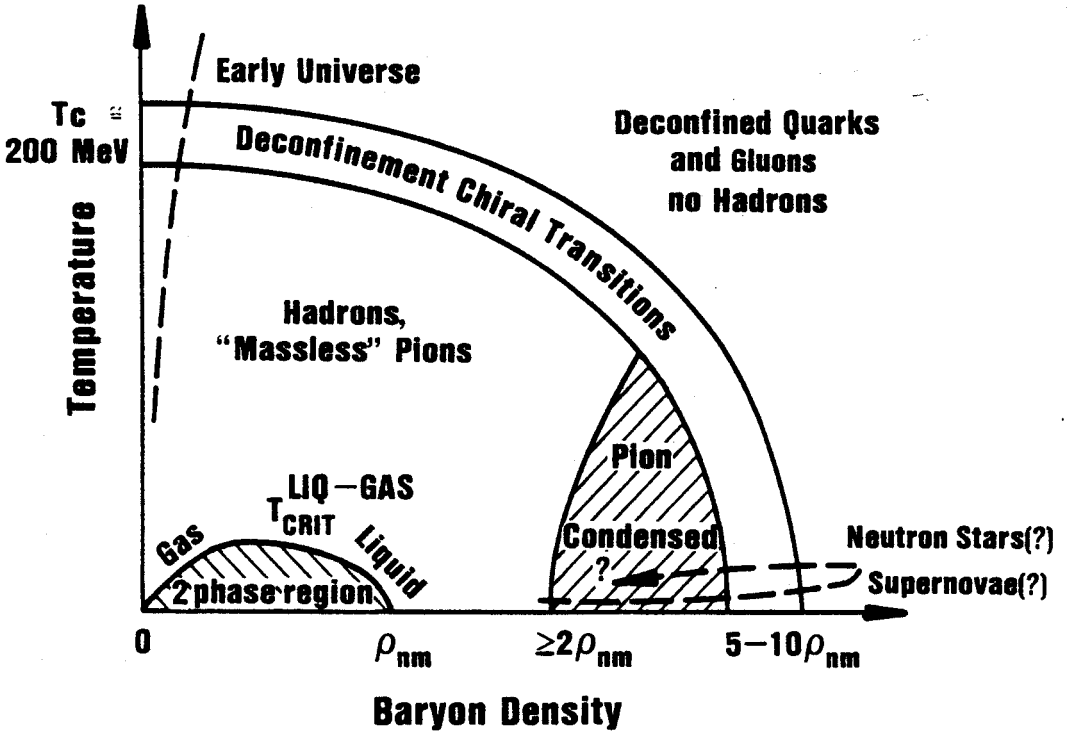

Figure 1.1 The anticipated behavior of hadronic matter as a function of density and temperature (CUG 84a).

individual nucleons, pions, and other particles. The finite width of the boundaries reflects not only the uncertainties associated with extrapolation to such extreme states from our present knowledge but also the belief that such transitions may not take place abruptly.

The topic of this thesis concerns composite particle production in intermediate energy heavy ion collisions, defined roughly as the energy range from 10A to 250A MeV. As alluded to earlier, composite particle production represents an unstable condition of nuclear matter for a temperature $T > T_c \cong 20$ MeV, i.e. the region of Figure 1.1 outside the two-phase region. The intermediate energy regime is conjectured to produce energy densities equivalent to temperatures roughly in the $5 \leq T \leq 50$ MeV range, thus providing a fertile testing ground for a liquid-gas phase transition. However, the interest in the intermediate energy regime is not confined solely to this phase instability, since collisions at intermediate energy are also expected to encompass regions where the average energy density per nucleon exceeds the binding energy per particle ($\cong 8$ MeV/A at $\rho = \rho_0$) as well as the Fermi energy ($\cong 38$ MeV for $\rho = \rho_0$), which marks the nominal boundary between the quantal behavior of fermions or bosons and classical physics. Another interesting threshold encompassed by nuclear collisions in this energy regime is the velocity of sound in normal density nuclear matter ($\cong .2c$).

Heavy ion collisions can serve as a possible probe of extreme states of nuclear matter, though by no means is their usefulness limited to this purpose. It is important to recall some characteristics of the heavy ion reaction mechanism which will be important in the interpretation of the observables. One important feature of heavy ion collisions, as opposed to proton induced collisions, is the possibility of a compressional phase. The overlap region between the projectile and the target of a heavy ion collision will produce densities of the order $2\rho_0$ while a corresponding collision involving a proton will result in a system where $\rho \cong \rho_0$. One generally anticipates that the energy density will increase with increasing incident energy, for both proton and heavy ion induced collisions, although the amount of energy deposited may saturate, a phenomenon commonly referred to as limiting fragmentation.

The inherent ephemeral nature of collision phenomena may introduce complications in their use as a probe of static or quasi-static descriptions of nuclear matter. Possible measures of the transient nature of such collisions are the interaction times or the decay time of the resultant system which are energy dependent. A measure of the time necessary for quasi-static behavior to manifest itself is the relaxation time of the system. It has been established for relatively low energy collisions that compound nuclear complexes are formed with subsequent emission of radiation characteristic of global equilibration; on the other hand, collisions at higher energy exhibit only localized equilibration in the nuclear

fireball or hot spot (SCO 80). If time scales are considered relevant then dynamics may also influence the physical observables. Several dynamical scenarios are being developed which demonstrate the resultant modifications to quasi-static behavior; these include various hydrodynamical descriptions (STO 81) and intranuclear cascade codes (BER 81). However, one very interesting, inherently dynamical, self-consistent field theoretical model has recently been developed (KNO 84) which predicts dynamical instabilities during the expansion phase that follows the compressional phase in a heavy ion collision.

To understand one of the major advantages of such a dynamical description it is necessary to digress for a moment. Experimentally, the detection of nuclear fragments occurs at $\rho \cong 0$. However, since strongly interacting nucleons have relatively short interaction ranges, when their separation becomes commensurate with the internucleon separation, the system is said to have "frozen out." Aside from final state interactions and sequential decays, the fragments then travel undisturbed to the detectors. Thus the physics observed at the detectors is reminiscent of the physics which occurred at $\rho = \rho_f$, rather than at $\rho = 0$. The freeze out density is a loosely defined term and is most likely dependent on fragment mass and energy density. It is also likely that the freeze out mechanism is not very abrupt. The mass and energy dependences of the freeze out density can be ascertained from coincidence experiments (CHI 85). The dynamical model obviates the necessity of

a freeze out concept, since it models each individual collision directly. From our point of view in this thesis, it is intriguing that the result of such a calculation predicts critical behavior of mass spectra similar to that predicted in quasi-static macroscopic approaches and in the same general temperature range. Due to the finite number effects, however, the transition is broadened considerably (GOO 83).

As stated earlier, for increasing incident energy the fraction of the system which equilibrates may decrease. Figure 1.2 illustrates schematically how this localization of the deposited energy may occur. If fragments are emitted on the average before attainment of global equilibrium, then these fragments will carry a signature of emission from a localized source. This behavior is depicted in Figures 1.2b and c. Figure 1.2a reflects the condition of global equilibration and Figure 1.2d illustrates the fireball geometry where the geometric overlap of the projectile and target defines three distinct entities. Firstly, a projectile remnant composed of projectile nucleons whose trajectories do not coincide with the target nucleon trajectories, may be formed. This projectile-like fragment will possess a velocity near the beam velocity and will carry a small transverse momentum. Secondly, the target remnant will be composed of fragments travelling with a very small velocity compared to the projectile velocity. These fragments are classified as spectators. We now consider the intermediate participant nucleons. These are comprised of both projectile and target

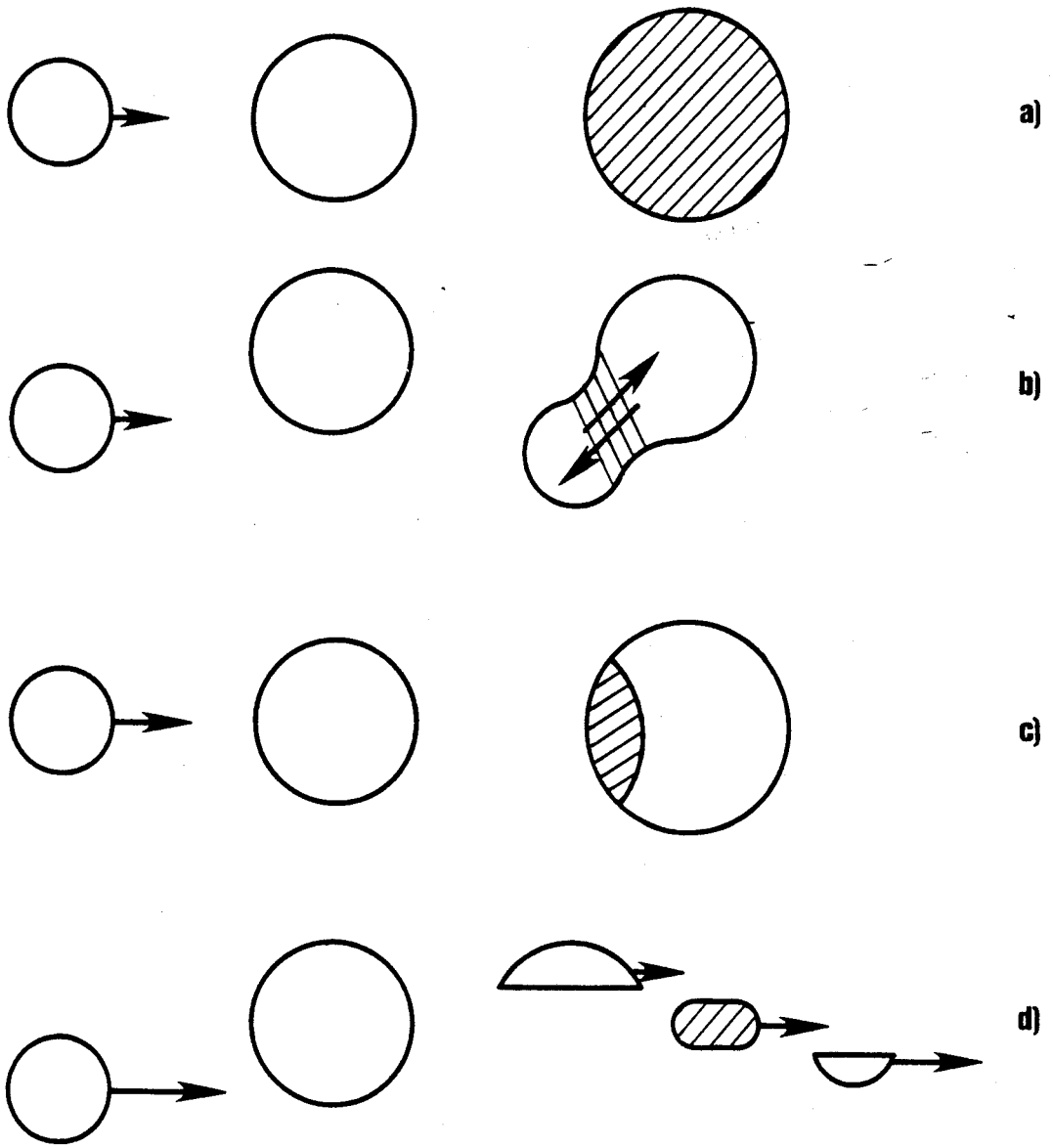

Figure 1.2 **Illustration of nuclear collisions at various energies and impact parameters. a) At relatively small incident energy the projectile involved in a central collision produces a compound nucleus where the energy density has sufficient time to equilibrate. b) Peripheral collisions at low incident energies must equilibrate different degrees of freedom across the neck of the dinuclear system; thus the degree of equilibration will vary depending on energy, impact parameter and relaxation time scales. c) In this collision the time scales do not permit global equilibration prior to "break-up." d) A fireball geometry where the high energy density region breaks away. Shaded regions denote higher than normal energy densities.**

nucleons in the overlap region, possessing a velocity intermediate between that of the projectile and that of the target. If a sufficient number of collisions takes place among the constituent participant nucleons, the system will achieve thermalization. Thus, the participant system forms a heated, dense, finite system of nuclear matter. The gross features of the fireball, as this system is generally referred to, are determined by simple kinematical considerations. The inelasticity of the collision determines the amount of energy supplied to the thermal degrees of freedom of the system. Proton emission is described utilizing a Boltzmann distribution of the nucleon velocities. Composite particle production was initially described by superimposing a coalescence mechanism upon the statistical distribution of nucleon momenta, i.e. if the relative momenta of the two nucleons lie within a sphere of radius defined by p_0 (the coalescence radius in momentum space) then the nucleons form a composite fragment such as a deuteron. Larger fragments are formed in an analogous manner (MEK 81).

At incident energies far in excess of typical nuclear binding energies, for example in high energy collisions (E > 250A MeV) at the Bevalac, the fireball model works quite well (GOS 77). However, it is less clear for the intermediate energy regime ($10A\ MeV \leq E \leq 100A\ MeV$) that this approach remains valid. Rather, the localization, if it occurs, in this energy domain may be described by hot spot formation (FIE 84). With the advent of accelerators capable of accessing this energy regime, the intrinsic

interest in critical phenomema and in energy localization, for example, has been rekindled. A multitude of physically relevant benchmarks regarding nuclear matter fall into this realm, e.g. the Fermi Energy ($\cong$ 38 MeV), velocity of sound ($v \cong .2c$), and the critical temperature ($\cong$ 20 MeV).

Let us consider some of the interesting speculations. Nuclear scattering experiments demonstrate that the nuclear force has both a long range attractive and a short range repulsive nature. It is well known from mechanics and from atomic and molecular physics that such forces give rise to regions of instability. In nuclear matter the nuclear incompressibility modulus, K, plays a crucial role in determining the boundary between the stable and unstable regimes. Phenomenological parameterizations (ZAM 73) of the nuclear force indicate the region for which the nuclear matter should be unstable. However, the manner in which the instability manifests itself is a subject of current debate. A mechanical instability (BER 83) pictures the disassembly as a large scale monopole oscillation along a given isentrope until the system enters an unstable region whereupon it fractures into light composite fragments. The proponents of models of liquid-gas phase transitions (CUR 83a; FIN 82; MIN 82) envision an evolution of the system where compression leads to the formation of the liquid component and the ensuing expansion gives rise to the gaseous component, the constituent ratios of which are determined by the temperature and density of the system. The system proceeds until it reaches the freeze-out density (MEK 81) where the

liquid and gas primary distribution is "frozen." The theory further contends that the fragments thus produced travel undisturbed, aside from final state interactions, to the detectors. If the temperature is sufficiently high at freeze-out then only a gaseous system will remain since the system can no longer support a liquid phase.

Another interesting model (AIC 84a; AIC 84b) has been proposed which describes the evolution of the system in terms of a localized, hot subset of nucleons which emits energetic nucleons. These in turn are absorbed by the surrounding cold nuclear matter thus exciting it above the Coulomb energy threshold necessary for the cold nuclear matter to shatter. The latter is similar in nature to the shattering of glass, thereby displaying an aspect of the nucleus characteristic of a solid as opposed to a liquid or gas. These concepts led to the experiments to measure fragment production which are described in this thesis.

The thesis is organized in the following manner. In Chapter 2 we examine two types of nuclear instabilities. First, we discuss a liquid-gas phase instability and the predicted complex fragment yield of such a model. Second, we discuss a mechanical instability. We then focus our attention on the relevant time scales for each of these phenomena. We estimate the time necessary for each to develop and compare to the time estimated for disassembly. In addition, we will discuss briefly several complicating factors such as Coulomb tunneling effects on mass yields, finite number effects, evaporation and final state effects and how each will modify conclusions and

predictions. Chapter 3 describes other theories of complex particle production; early statistical models (thermal and coalescence), as well as Compound Nucleus Fission and the Cold Shattering Model are discussed, together with the associated predictions of the resultant fragments. Subsequently, in Chapter 4 our experiments on complex fragment production in heavy ion reactions are described. In Chapter 5 the results and interpretations of the experiments are presented, and placed in the context of other experiments. Detailed comparisons of the data are made with the predictions of the Compound Nucleus Model, the Cold Shattering Model, and Liquid-Gas Model. In Chapter 6 we present our conclusions regarding the different models, and suggest future experiments and theoretical avenues to pursue.

In conclusion, our present knowledge of nuclear matter centers around ($\rho \cong 0$, $T \cong 0$) and ($\rho_0 \cong .17$ fm^{-3}, $T \cong 0$), thus indicating that the logical course to pursue entails investigating phenomena relatively close to familiar conditions, where theoretical extrapolations and experimental complications are minimal. It is our belief that an understanding of a lower density, lower temperature phase transition can serve as a springboard to explore even more exotic and interesting states of nuclear matter. (A recent review is given by Cugnon (CUG 84a).)

CHAPTER 2

CHEMICAL AND MECHANICAL INSTABILITIES

2.1 Introduction

In this chapter we examine the chemical and mechanical instabilities associated with hot, dense nuclear matter. Time scales relevant to these instabilities will also be discussed. Most of the contents of this chapter are the theoretical contribution of the author to the field.

First, the chemical instability will be examined utilizing a Skyrme interaction. (A simpler treatment has been given by Boal (BOA 84b).) Since this approach does not readily yield information regarding experimental observables, it was necessary to augment our investigation using a macroscopic approach. Our phenomenological approach to phase instabilities also stimulated the application of percolation theory to nuclear collisions, and we, therefore, include a brief description of the underlying tenets and predictions. Surface and Coulomb effects on the liquid-gas phase instability are also presented. Second, the mechanical instability is presented in a manner analogous to the chemical instability and the alternate physical interpretation of the negative incompressibility region is emphasized. The experimental observables are then explored. Several effects that could influence the application of this theory to nuclear systems are enumerated. Finally, the time scales

relevant to thermal and chemical equilibration are compared to typical nuclear transit times and the oscillation times characteristic of the mechanical instability.

2.2 Chemical Instability

2.2.1 Theoretical Formulation for Nuclear Physics

To derive the condition for a liquid-gas instability, we start from the relation (CUR 83a)

$$\rho = \frac{4}{(2\pi)^3} \int d^3k \left[1 + \exp\left(\frac{\frac{k^2}{2m} - \mu}{T} \right) \right]^{-1} , \qquad (2.2.1)$$

from which the chemical potential, μ, is determined as a function of the density ρ and the temperature T. The thermal contribution to the internal energy is given by

$$\frac{E_T}{V} = \frac{4}{(2\pi)^3} \int d^3k \, \frac{k^2}{2m} \left[1 + \exp\left(\frac{\frac{k^2}{2m} - \mu}{T} \right) \right]^{-1} , \qquad (2.2.2)$$

using the calculated values of μ. The pressure due to the thermal motion is then $2E_T/3V$ corresponding to a zero point pressure of $\frac{2}{5} \varepsilon_F(\rho)$, where ε_F is the Fermi energy. The total pressure is the sum of the thermal pressure and the pressure, P_v, due to the interaction among the constituents of the system. To derive P_v we express the energy per nucleon in the form (ZAM 73) obtained from a Skyrme type interaction, ignoring the effective mass contribution,

$$\frac{E_V}{A} = -\bar{A}\rho + \bar{B}\rho^{\sigma+1} \qquad (2.2.3)$$

where $\bar{A}$ and $\bar{B}$ are constants determined by the constraint $E/A = -16$ MeV (for nuclear matter) where $\rho = \rho_0$, together with the further condition for stability of normal density nuclear matter, $\partial(E/A)/\partial\rho = 0$.

Solving for $\bar{A}$ and $\bar{B}$ with $\varepsilon_F(\rho = \rho_0) = 38$ MeV and $\sigma = 2/3$ we find $\bar{A}\rho_0 = 74.2$ MeV and $\bar{B}\rho_0^{5/3} = 35.4$ MeV. In general $\bar{A}$ and $\bar{B}$ have some temperature dependence but here we assume that the thermal and interaction energies and pressures are separable. The pressure due to the interaction (at $T = 0$) is $\rho^2\ (E/A)/\partial\rho$, resulting in

$$\frac{P_V}{\rho} = -\bar{A}\rho + \frac{5}{3}\bar{B}\rho^{5/3} \quad . \qquad (2.2.4)$$

The total pressure as a function of density for constant temperature is plotted in Figure 2.2.1, which shows that the equation of state has the form typical of a Van der Waal's system with liquid and gaseous phases. For the unphysical region (shown only for $T = 15$ MeV) where the slope is negative (implying a negative incompressibility) a Maxwellian construction is employed, along which the liquid and gas phases coexist. The region of coexistence is indicated in Figure 2.2.1. The range of densities compatible with coexistence becomes smaller as the temperature increases until the apex of the coexistence region coincides with the inflection point of the critical temperature curve. At this critical

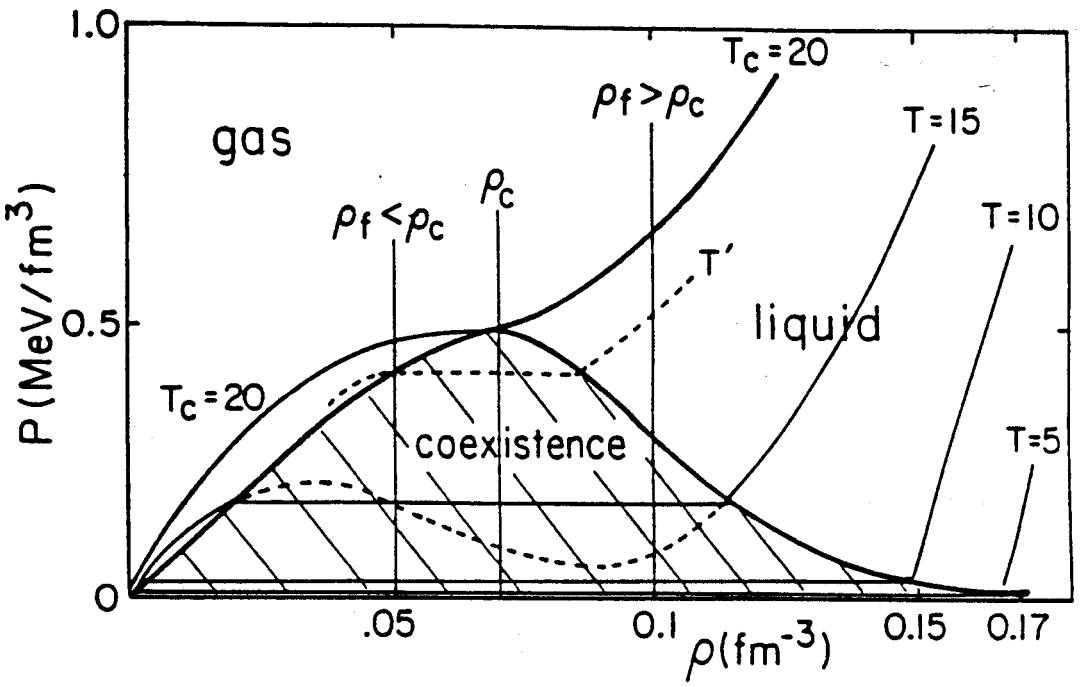

Figure 2.2.1 **Nuclear pressure versus density for fixed temperature is plotted. Solid curves indicate paths traversed by a system with fixed T. Liquid, gas, and coexistence (hatched) regions are indicated. The significance of ρ_f, ρ_c, and T' are discussed in the text.**

temperature, $T_c \cong 20$ MeV, the coexistence of liquid and gas phases is possible only at $\rho_c = 0.07$ fm^{-3} and only a gaseous phase exists for all higher temperatures. Our results are in good agreement with recent calculations (FRI 81; ROP 82).

Our choice of parameters leads to an incompressibility of 312 MeV ($K \cong 168 + 216\ \sigma$; PRE 75). Current estimates from nuclear monopole excitations indicate that the incompressibility is approximately 210 MeV (SER 80). In our calculation we let E/A = -16 MeV (ignoring surface effects) and $\sigma = 2/3$ in the Skyrme interaction. The thermodynamic treatment implies a large system and hence E/A is approximately fixed at -16 MeV. If σ is allowed to change to reproduce K = 210 MeV, a critical temperature of 17 MeV is predicted.

In order to discuss the observable consequences of the phase instability at T_c, several points must be assessed. First, the relevance of the isotherms in Figure 2.2.1 to the actual evolution of the disassembling nuclear system must be assessed. According to cascade model calculations (GUD 79) at incident energies $\leq$ 250A MeV, the temperature does not vary rapidly as a function of time and consequently the time evolution of the system may be considered isothermic for a temperature in the critical region of 20 MeV, corresponding to incident energies of $\cong$ 100A MeV. In contrast to the cascade model, hydrodynamical calculations indicate that entropy, as opposed to temperature, may remain constant during expansion. Recent hydrodynamical calculations (STO 81) indicate that constant temperature in the critical range is, however, a

plausible assumption. In this section we assume that a constant temperature is appropriate to the disassembly process.

Finally, we must note that during the disassembly phase of the hot region, the density decreases until the thermal freeze out density (ρ_f) is reached. This density is roughly defined when the mean free path becomes commensurate with the physical size of the hot region. Collisions cease at ρ_f and the fragments travel undisturbed to the detectors aside from final state interactions (MEK 81). To observe both liquid and gas phases at a given temperature, the Maxwellian construction must encompass the region of freezeout, defined by ρ_f. If ρ_f is large then the system will be in the liquid phase at freeze out, whereas if ρ_f is small only the gas phase will exist signifying that the system has traversed the coexistence portion of the isotherm and the liquid phase no longer exists.

In the event that $\rho_f < \rho_c$ the system will enter the gas phase prior to freeze out leading to an erroneous interpretation of T' as the critical temperature T_c (CUR 83a). Further inspection of Figure 2.2.1 indicates that for $\rho_f \geq \rho_c$ the temperature T_c will be correctly identified. It is physically unlikely that freeze out will occur for densities greater than the critical density since this is a density for which the liquid phase exists, and therefore an interaction is required in contradiction to the nature of the freeze out concept.

The arguments presented do not at present lend themselves readily to predictions of complex fragment yields. Hence it is necessary to examine a macroscopic model for specific, experimentally accessible predictions of a liquid-gas phase transition.

2.2.2 Macroscopic Approach

The probability of forming a cluster of size A is (FIS 67)

$$Y(A) \propto A^{-k} e^{(\mu - F)/T} \tag{2.2.5}$$

where F is the Helmholtz free energy and

$$F = E - TS \ . \tag{2.2.6}$$

If the energy and entropy are divided into volume and surface components, they are expressed mathematically as

$$E = e_V A + e_S A^{2/3} \tag{2.2.7}$$

$$S = s_V A + s_S A^{2/3} \ ,$$

where e_V, e_S, s_V, s_S are the specific volume and surface energy and entropy, respectively. The probability can be rearranged in the following convenient manner:

$$Y(A) \propto A^{-k} \cdot x^{A^{2/3}} \cdot y^A \tag{2.2.8}$$

where

$$x = \exp\left\{-\left(\frac{e_S - Ts_S}{T}\right)\right\} \tag{2.2.9}$$

$$y = \lambda \exp\left\{-\left(\frac{e_V - Ts_V}{T}\right)\right\} \qquad (2.2.9)$$

$$\lambda = \exp(\mu/T) \quad .$$

The set of points $\{\sigma\}$ at which condensation occurs satisfy the relations

$$y_\sigma = 1 \qquad x_\sigma = 1 \qquad (2.2.10)$$

whereby $Y(A)$ is determined as

$$Y(A) \propto A^{-k} \quad . \qquad (2.2.11)$$

This power law dependence is not confined solely to the critical point. If $\rho_f < \rho_c$ the power law dependence would still hold in this formulation, albeit at a temperature $T' < T_c$ (see Figure 2.2.1). The condensation points $\{\sigma\}$ constitute the boundary between the gaseous and coexistence regions and are illustrated in Figure 2.2.2. The surface free energy is zero at the critical point. Thus, the surface component of eq. (2.2.6) yields

$$T_c = \frac{e_S(T_c)}{s_S(T_c)} \qquad (2.2.12)$$

and hence the surface physics determines the critical behavior. For regions other than those of condensation, the following relations hold:

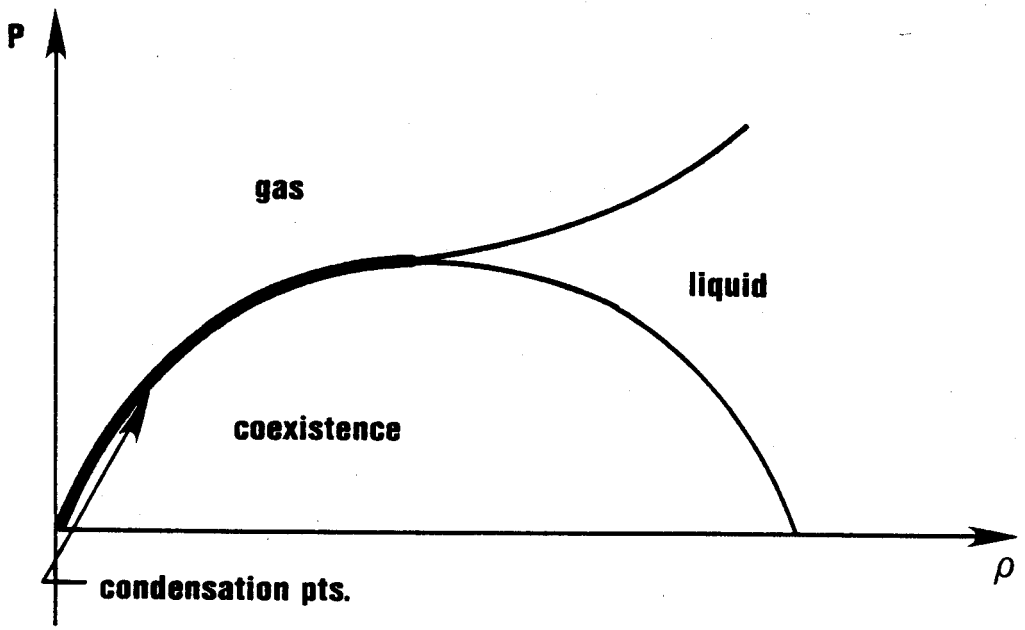

Figure 2.2.2 **The boundary between the gaseous and coexistence regions is emboldened. This interface constitutes the set of points where condensation begins .**

$y < 1$ gaseous phase

$y > 1$ liquid phase

$x < 1$ $T < T_c$

$x = 1$ $T = T_c$

$x > 1$ $T > T_c$.

The possibility of a phase transition in an equilibrated nuclear system was previously considered theoretically in a number of papers (CUR 83a; PAN 84; PAN 85; DAN 79 and references therein). Examination of light-ion production cross sections over a wide range of incident energies has indicated that it will also be necessary to measure intermediate mass fragment cross sections in order to obtain an unambiguous experimental signature of phase transitions (CUR 83a). It has already been suggested in a number of recent papers that the power law dependence, $Y(A) \cong A^{-\tau}$, of the fragment distributions may constitute a signature for the occurrence of phase transition phenomena near a critical point (MIN 82; FIN 82; HIR 84). The widely differing systems which exhibit this characteristic power law dependence suggest that phase transitions are not specific to the projectile-target combination, but dependent only on the energy per particle imparted to the interacting system. However, the temperatures of the reported systems vary between about 8 MeV (CHI 83) and 15 MeV (FIN 82). Clearly, all of these systems cannot be near the critical point.

To understand the temperature dependence, we first fitted the existing data on fragment distributions with a power law dependence of the form $Y(A) \cong A^{-\tau}$, where τ is the "apparent" exponent. In this approximation, the effects of any temperature-dependent factors are absorbed into the power law exponent. Therefore, this apparent exponent will vary with the temperature.

For some of the analyzed data the temperature of the system has been extracted from moving source fits to the fragment energy distributions (see e.g. Fields et al. (FIE 84)). Where the temperature was not determined in this manner, we determined it either from the slope of the tail of the 90° fragment energy distributions, or from the ideal Fermi gas, assuming the size of the emitting system to be in the range of 2 to 3 times the largest emitted fragment mass. The fragment masses used to determine the power law exponent were in the range of $3 \leq Z \leq 22$ for all systems; care was taken to avoid contributions from the tail of possible fission fragments. Table 1 summarizes the data used and the values obtained by the fit.

In Figure 2.2.3 we plot the apparent exponent, τ, determined from a least-squares fit to the fragment distributions as a function of the temperature of the emitting system. Nominal error bars of $\pm$ 1 MeV were used in our analysis. We observe a dramatic temperature dependence of the apparent exponent, which decreases as the temperature increases to about 11-12 MeV, after which the trend reverses. The exponent reaches a minimum value of about 1.7 at a temperature in the region of 11-12 MeV, which may be indicative of a

Table 1. Summary of the data used and the values of the apparent exponent obtained from the power-law fit to the fragment distributions.

System	Energy (GeV)	A or Z Range	Temperature (MeV)	Angular Range (degrees)	Exponent (± 0.2)	Reference
p + Ag	0.21	$3 \leq Z \leq 8$	6.0 ± 1.	20, 90, 160	4.1(4.7)[a]	GRE 80
p + Ag	0.30	$3 \leq Z \leq 8$	6.7 ± 1.	20, 90, 160	3.7(4.3)	GRE 80
p + Ag	0.48	$12 \leq A \leq 25$	8.2 ± 1.	20 - 160	3.2	GRE 83
p + Ag	4.9	$6 \leq Z \leq 18$	14.0 ± 1.	90[b]	2.4	WES 78
p + Kr	80-350	$12 \leq A \leq 30$	14.5 ± 1.	34[b]	2.9	FIN 82
p + Xe	80-350	$12 \leq A \leq 30$	15.0 ± 1.	34[b]	2.9	FIN 82
p + U	4.9	$6 \leq Z \leq 11$	13.5 ± 1.	20, 90, 160	1.9[c]	WES 78
p + U	5.5	$3 \leq Z \leq 11$	12.6 ± 1.	20 - 160	1.7(1.8)	POS 71
C + Ag	0.36	$4 \leq Z \leq 22$	8.3 ± 1.	40 - 70	2.6(2.6)	CHI 83
C + Ag	0.18	$3 \leq Z \leq 13$	7.2 ± 1.	50 - 70	3.0(3.2)	CHI 83
C + Au	0.36	$3 \leq Z \leq 11$	7.7 ± 1.	50 - 120	2.8(2.8)	CHI 83
C + Au	0.18	$4 \leq Z \leq 11$	6.2 ± 1.	50 - 120	3.8(3.7)	CHI 83

[a]The apparent exponent, τ, obtained with the restricted range of masses, $Z \geq 5$, is shown in parentheses.

[b]An almost isotropic (to about 20%) angular distribution was assumed in obtaining the integrated total cross section.

[c]Cross sections for Z = 6, 7, 8, taken from POS 71, were normalized to the 4.9 GeV data (WES 78) in order to extend the Z range. This makes the POS 71 data compatible with the other data but double-weights the WES 78 Z = 6, 7, and 8 data.

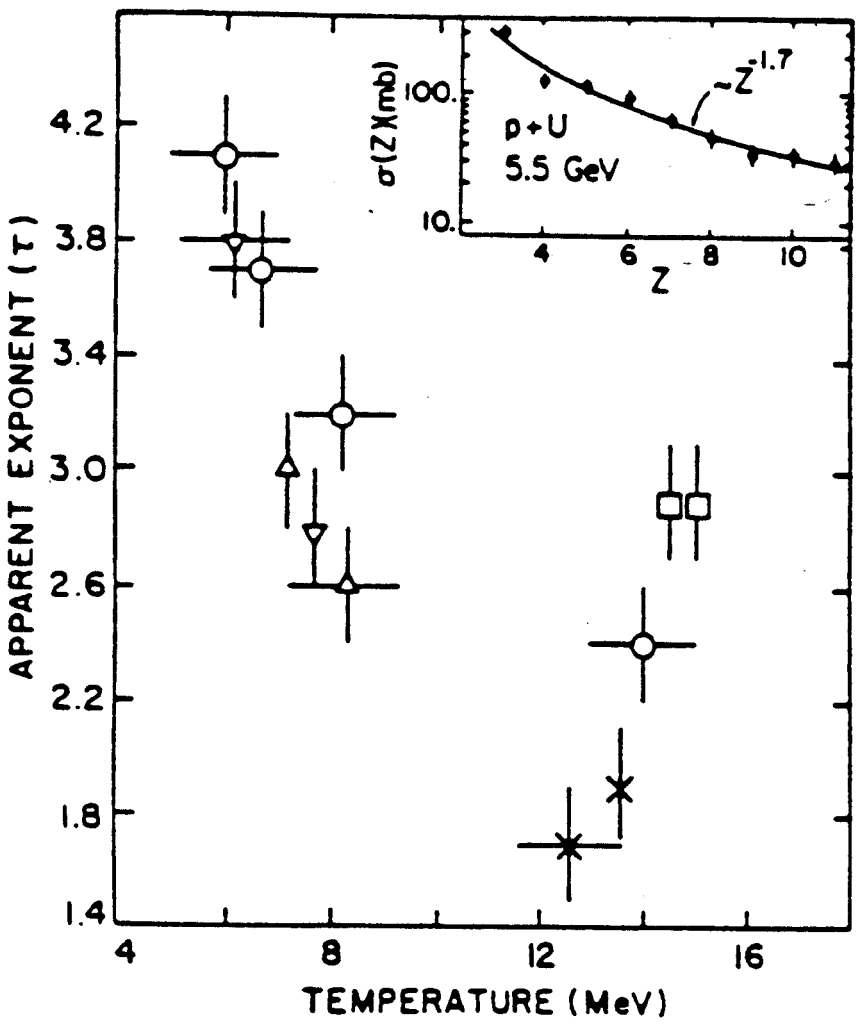

Figure 2.2.3. **The apparent exponent, τ, of the power law fit to the fragment distributions as a function of the temperature, T. The inset shows a typical power law fit to a fragment distribution (PAN 84).**

phase transition as we show shortly. This conclusion is in disagreement with the result T_c = 3.3 MeV (MIN 82), obtained from the isotope distributions, but it is in agreement with calculations for finite nuclear systems, which predict T_c in the range of 9-13 MeV (JAQ 83; JAQ 84). It is possible that the temperatures deduced from isotope distributions require correction for the effects of sequential decay.

Since the deexcitation processes of the emitted fragments may make it difficult to obtain accurate information from lighter fragments, we restricted the range of the fragment charge to $Z \geq 5$ to obtain the power law apparent exponent (see Table 1). This new set of data produced the same dramatic features as the full set shown in Figure 2.2.3.

This behavior of the temperature dependence of the fragment yield prompted us to fit the fragment distributions with expressions obtained from a theory of condensation in excited nuclear matter, in which the probability for fragment formation of size A is given by (see eqs. (2.2.8) and (2.2.9))

$$Y(A) \propto A^{-k} \exp\left\{ \frac{-a_s'(T)A^{2/3} - a_v'(T)A + \mu(T)A}{T} \right\} \qquad (2.2.13)$$

where k is the critical exponent, $a_s'(T) = e_s(T) - Ts_s$ is the surface free energy per particle, $a_v'(T) = e_v(T) - Ts_v$ is the volume free energy per particle, and $\mu(T)$ is the chemical potential per particle. The above relation can be written in the following form:

$$Y(A) \propto A^{-k} x^{A^{2/3}} y^{A} \tag{2.2.14}$$

where

$$x = \exp\left[\frac{-a_s'(T)}{T}\right]$$

$$y = \exp\left\{-\left[\frac{a_v'(T) - \mu(T)}{T}\right]\right\}. \tag{2.2.15}$$

In the region $T < T_c$, where gas and liquid phases coexist, the sum of the volume energy per particle in the liquid phase and the Gibbs free energy per particle in the gaseous phase is equal to zero, i.e., $a_v'(T) - \mu(T) = 0$. Therefore, the exponential factors are $y = 1$ and $x < 1$, and the probability $Y(A)$ can be written as

$$Y(A) \propto A^{-k} \exp\left[\frac{-a_s'(T)A^{2/3}}{T}\right]. \tag{2.2.16}$$

At the critical point, determined by $T = T_c$, the surface free energy term is equal to zero, $a_s'(T) = 0$, and in addition $a_v'(T) - \mu(T) = 0$. Therefore, both exponential factors give $x = 1$ and $y = 1$, and the probability assumes the pure power-law form

$$Y(A) \propto A^{-k} \quad . \tag{2.2.17}$$

Finally, for $T > T_c$, corresponding to a gaseous phase, we assume that the surface free energy is very small, $a_s'(T) \cong 0$, while

$a_v'(T) - \mu(T) > 0$. Therefore, the exponential factors are $x \cong 1$ and $y < 1$, and the probability $Y(A)$ assumes the form

$$Y(A) \propto A^{-k} \exp\left\{ - \frac{[a_v'(T) - \mu(T)]A}{T} \right\}. \qquad (2.2.18)$$

We note that the exponential factors x and y, at temperatures $T < T_c$ and $T > T_c$, respectively, modulate the power-law dependence of the fragment distribution. Figure 2.2.4 illustrates the expected behavior of cross section versus fragment mass for temperatures less than, greater than, and equal to the critical temperature (SIE 83).

We parameterized the temperature dependence of the surface free energy as

$$a_s'(T) = c(1 - T/T_c)^2 \qquad (2.2.19)$$

where $c = 18.4$ MeV since $a_s'(T = 0) = 18.4$ MeV, the cold nuclear matter surface free energy, and $a_s'(T = T_c) = 0$. For the volume and the Gibbs free energies we take

$$a_v'(T) - \mu(T) = b(1 - T/T_c)^2 \qquad (2.2.20)$$

where b is a coefficient, the value of which is not known a priori; a value in the range 8-10 MeV was determined by the fitting routine. A least-squares fit to the fragment distributions was undertaken by using expressions (2.2.16) and (2.2.18) with the parameterizations (2.2.19) and (2.2.20), respectively, and letting

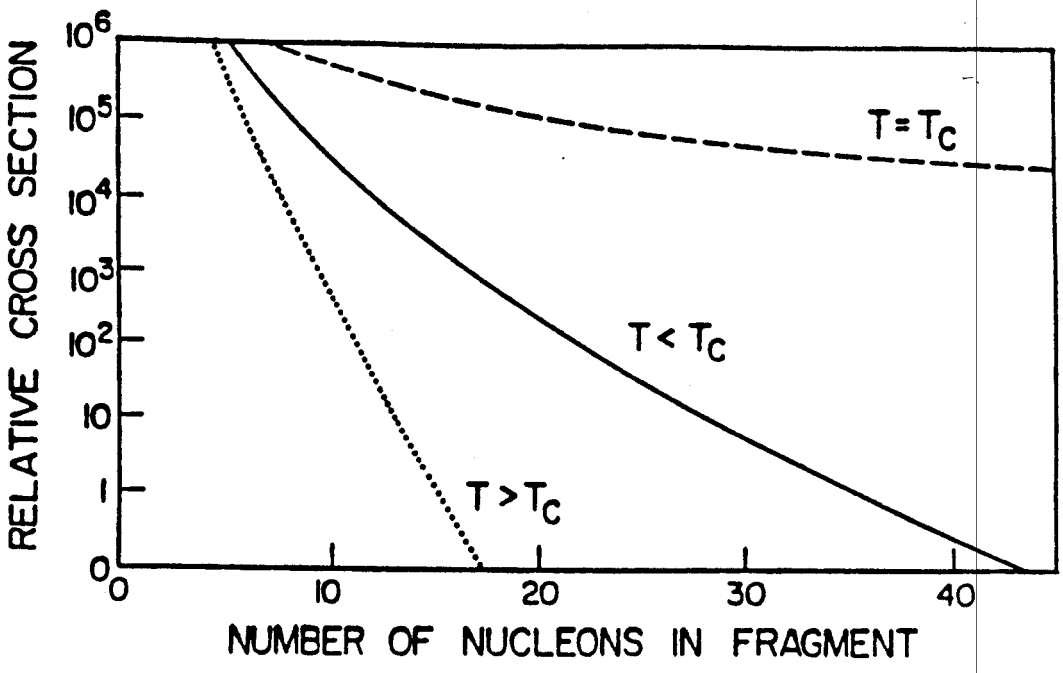

Figure 2.2.4 **Relative cross-sections as a function of fragment mass for three isotherms: one for a temperature less than, one greater than, and one equal to the critical temperature (SIE 83).**

the exponent, k, take successively the values 1.6, 1.7, 1.8, 2.0, 2.33 to yield corresponding T_c values. For the temperature of each system we used $T = T' \pm 1$ MeV, where T' is the averaged temperature for all emitted fragments used in each fit. This variation in T, resulting from the uncertainty in establishing the temperature of the source, produced a variation in the calculated T_c ($\pm$ .5 MeV).

Figure 2.2.5 shows the extracted critical temperature as a function of the critical exponent, k. We observe that for k between 1.7 and 1.8 the calculated T_c values for both $T < T_c$ and $T > T_c$ coincide, while for both lower and higher k values they diverge. We are, therefore, inclined to accept $k \cong 1.7$ as the critical exponent and $T_c = 12.0 \pm 0.2$ MeV as the critical temperature. The uncertainty in the critical temperature allows the possibility that the critical exponent k may take on values between 1.7 and 1.8, which is lower than the theoretical minimum value 2.0 for an infinite system (FIS 67). This lower value may reflect the finite nature of the systems considered and needs further theoretical investigation. We note, however, that this choice of parameterization reproduces the essential features of Figure 2.2.3. Calculations of thermal properties of nuclei, using the thermal Hartree-Fock approximation and the Skyrme III interaction (SAU 76), yield a critical temperature $T_c = 12.58$ MeV, close to the temperature extracted by our analysis.

The similarity of the power-law dependence ($2.5 < \tau < 2.7$) of the fragment distributions at very different temperatures ($8 \leq T \leq 15$ MeV) can now be understood in our picture; these points lie on

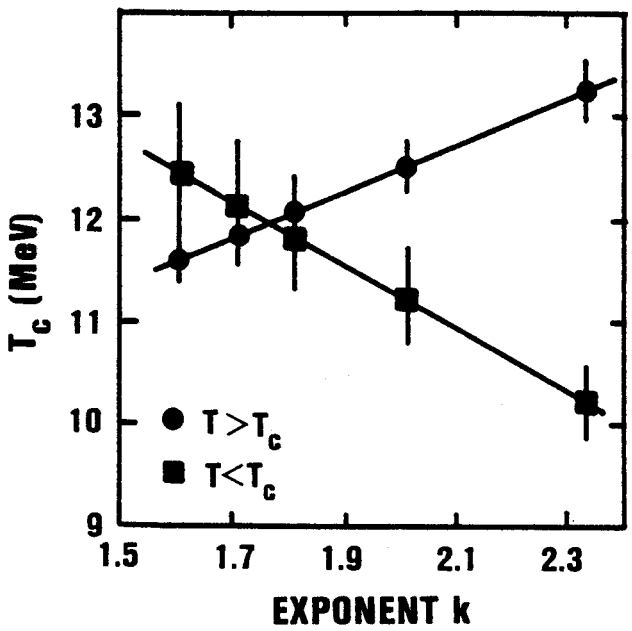

Figure 2.2.5. **The extracted critical temperature as a function of the critical exponent for temperatures less than and greater than the critical temperature (PAN 84).**

either side of the critical temperature and the power-law is about equally modified by the temperature-dependent exponential factors x and y, implying that the surface and volume contributions have approximately equal importance in determining mass distributions.

In this section it has been essential to assume the formation of thermalized hot matter of nuclear dimensions in the temperature range of 5 to 20 MeV. Furthermore, we have to rely on the freeze out concept, which ensures that the experimentally observed mass distributions reflect the configuration at the freeze out density of nuclear matter. Although both of the above concepts are generally accepted at very high energies (E > 250A MeV), they have to be confirmed by careful examination of the experimental data at intermediate energies. It is very encouraging, however, to find that the simple ansatz, taken from the theory of condensation, works very well in this wide energy range and for very different systems.

Our analysis made use of fragment distributions from widely different systems and with appreciable uncertainty in the temperature of the source. To circumvent this inherent difficulty it is preferable to choose a single projectile-target combination and measure fragment yields as a function of the incident energy in the region roughly corresponding to the critical temperature, i.e. from approximately 9 to 14 MeV. From such a study one may also be able to infer more accurately the form of the T dependence of the free energies very close to T_c, providing information concerning the equation of state of nuclear systems.

2.2.3 Percolation Theory

It is important to note that a liquid-gas phase transition is not the only theory which predicts a power law dependence of the yields of the form given in eq. (2.2.11). Recently, it has been suggested that a nonthermal phase transition based on percolation theory could also exhibit this behavior (BAU 85; CAM 85). (An excellent review is given by Stauffer (STA 79).) The percolation theory presented is not the work of the author. Figure 2.2.6 compares the prediction of a percolation calculation with experimental data (CAM 85). In this approach the nuclear matter is described in terms of a set of lattice sites. Two different interpretations based on percolation theory have been proposed. One describes the critical behavior in terms of the normalized probability that bonds between adjacent sites are broken (BAU 85) while the other refers to the normalized probability that a given lattice site is occupied (CAM 85).

The basic approach is as follows. Define p as the normalized probability that a site is occupied. If $p = 1$ then all sites are occupied and the cluster exists as one macroscopic droplet. Conversely, if $p \cong 0$ then most sites are vacant and lattice sites behave independently, thus resembling a gaseous state. Now let us explore the region $0 < p < 1$. A pictorial representation is shown in Figure 2.2.7. For a given system, the value of p fixes the global number of occupied sites which are randomly distributed between possible lattice sites. Only nearest neighbor bonds are

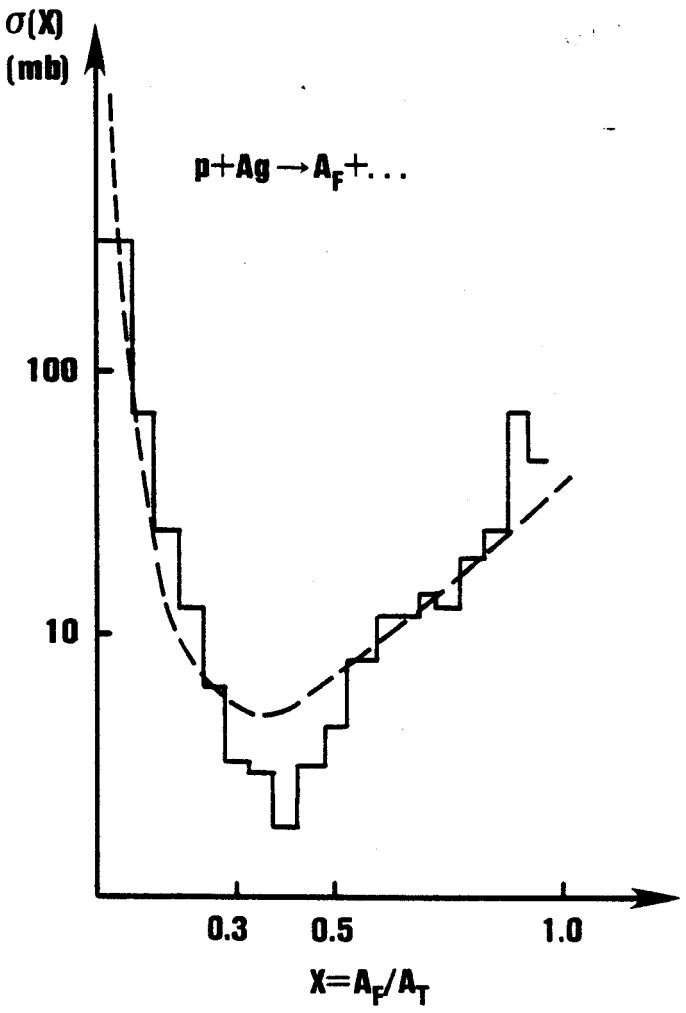

Figure 2.2.6. The mass yield of fragments A_F produced in the reaction $p+Ag \rightarrow A_F+\ldots$ at high energy. The dashed line denotes the data, and the histogram the predictions using percolation theory (CAM 85). The horizontal axis gives the ratio of the fragment mass A_F to the target mass A_T, where $A_T = 109$.

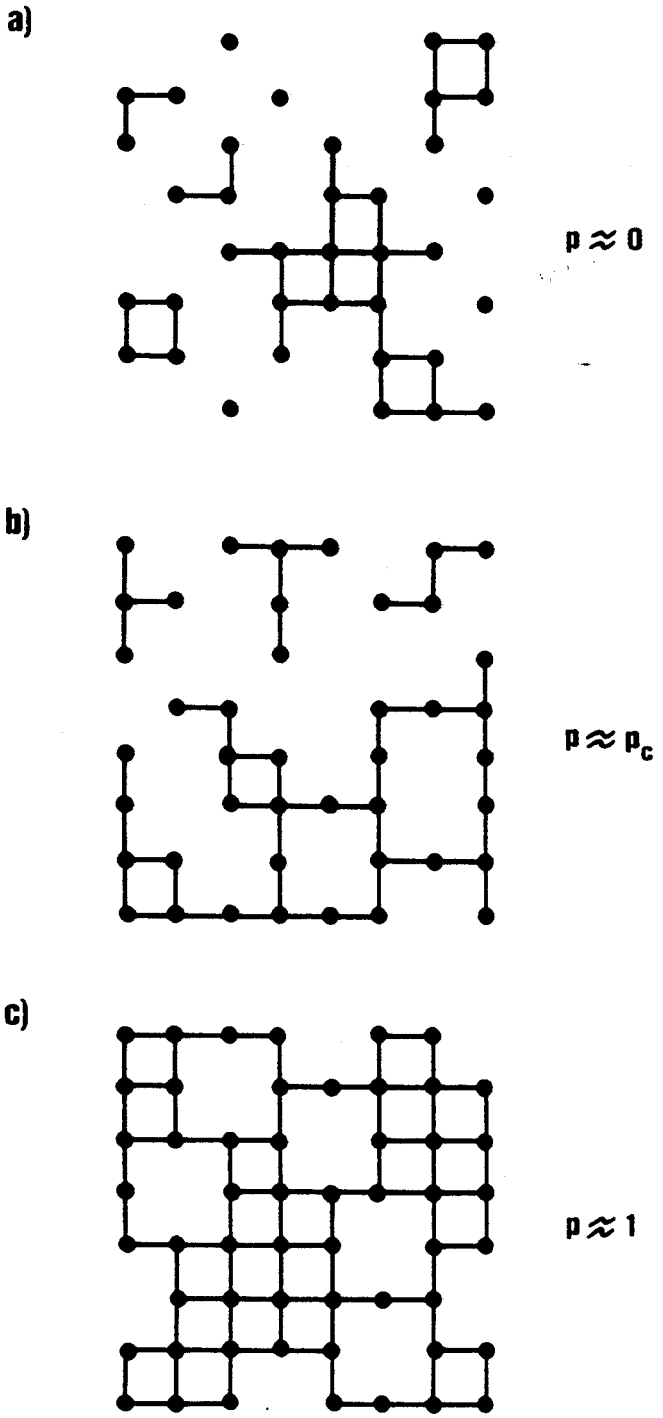

Figure 2.2.7 **Illustration of the percolation phase transition. Three cases are shown for $0<p<1$ where p is the fraction of sites occupied in a lattice. a) The $p\sim 0$ case where many small fragments exist with no single large cluster, b) $p\approx p_c$, and c) $p\approx 1$ where one large connected cluster exists.**

permitted. All interconnected lattice sites are considered part of the same entity which we will identify with a fragment. For an infinite lattice, where $p > p_c$, one large cluster exists whereas for $p < p_c$ no such cluster is found. Hence the system exhibits critical behavior as a function of p, in much the same way a liquid gas system behaves as a function of temperature. However, it is important to realize that nowhere does this theory mention thermalization or chemical equilibrium. Finite systems exhibit a noticeable softening of the percolation transition as can be seen upon examination of Figure 2.2.8. However, typical heavy ion systems should exhibit a clear differentiation between the $p < p_c$ and $p > p_c$ regimes. The experiment studied in this thesis (N + Ag) corresponds to an 11 x 11 percolation lattice, intermediate to the first two cases illustrated in Figure 2.2.8.

The percolation theory is a purely geometrical theory while the physical observables of a heavy ion collision are subject to the constraints of nuclear physics. The following constraints were imposed on the percolation theory in an effort to adapt it to nuclear collisions:

1) The nearest neighbor interparticle distance must be ≤ 2.5 fm.

2) $$|\vec{p}_i - \frac{1}{A_F} \sum_{k=1}^{A_F} \vec{p}_k| \leq p_F$$

where

p_i = nucleon momentum

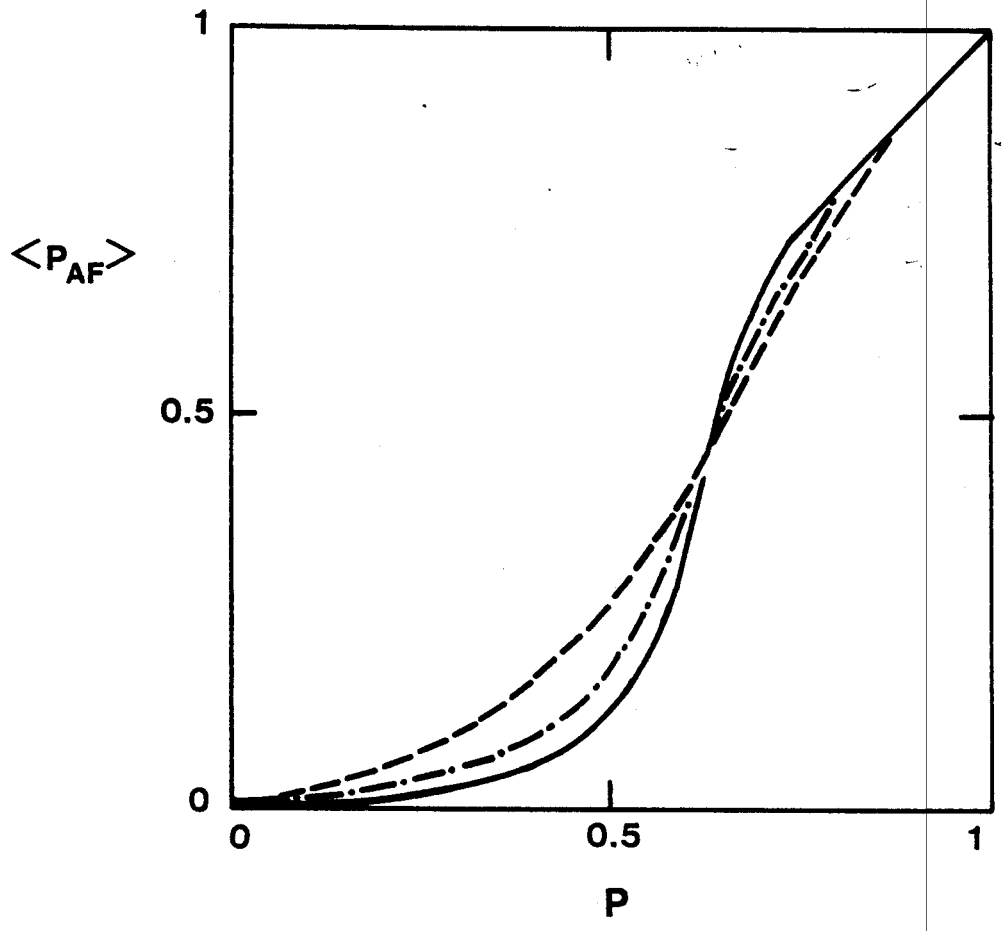

Figure 2.2.8 **Average largest cluster size (normalized to the number of lattice sites) for square lattices containing: 8 x 8 sites (dashed line); 14 x 14 sites (dash dot) and 20 x 20 sites (continuous line). An infinite system would correspond to a theta function ($<p_{AF}>= 0$ for $p<p_c$ and $<p_{AF}> = 1$ for $p>p_c$). The experimental conditions of the experiments in this thesis would correspond to an 11 x 11 site square lattice (CAM 85) .**

A_F = number of nucleons in the fragment

p_F = Fermi momentum

3) $r_{A_F} \leq (1 + .15) r_o A_F^{1/3}$.

(The last condition prevents counting of fragments which possess excessive surface excitation energies.) Figure 2.2.9a illustrates the effects of these constraints. The importance of the dimension of the lattice under consideration is discernible in Figure 2.2.9b. Recall that an important characteristic of nuclear matter is saturation. The number of nearest neighbor sites differs for different physical geometries (such as a simple cubic versus body-centered cubic). The investigation of different physical configurations in an attempt to simulate the saturation effects present in nuclear matter might also be of value.

The determination of the best fit to the predicted yields with an apparent exponent as function of p is shown in Figure 2.2.10. The resemblance to both the liquid-gas phase transition prediction and the data presented in Figure 2.2.3 is apparent. For an estimate of the equivalent temperature where critical behavior sets in, note that the occupation of each site corresponds to the release of $\cong$ 8 MeV and hence the total energy supplied to the system is 8Np, where N is the total number of possible lattice sites and here Np is the number of occupied sites. The energy of a system of A fermions at temperature T is given by $AT^2/8$, and we may identify A with number of vacancies in the system, i.e. N(1 - p). Thus we see

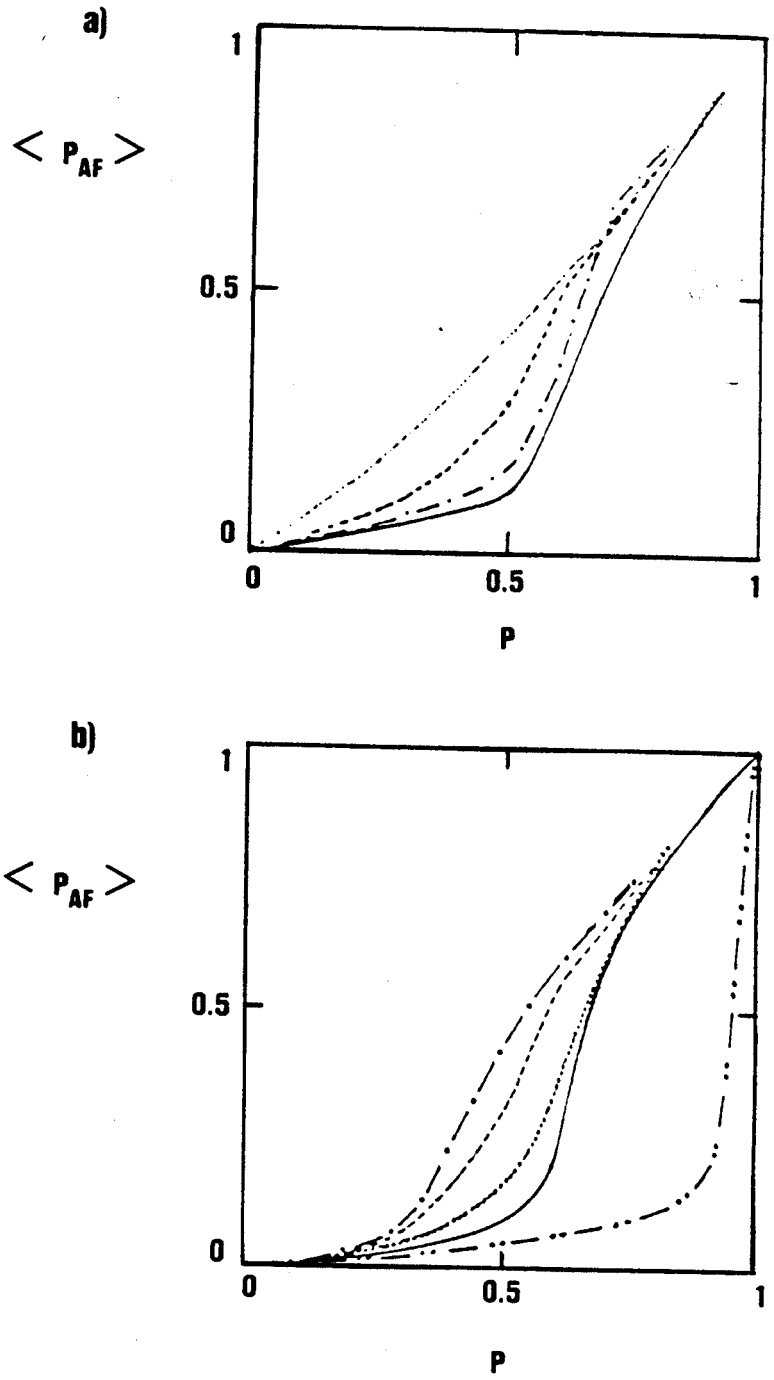

Figure 2.2.9. a) Results of a percolation theory with imposed constraints designed to simulate nuclear effects (see text). Constraint 1 only (dashed), constraint 2 only (dotted), constraint 3 only (dash-dot) and all three constraints imposed (continuous line) are shown. b) The effects of dimension are shown: 1-dimensional lattice (dash-dot-dot), 2-dimensional (dotted) and 3-dimensional (dash-dot). In each case the lattice possesses 109 sites. A 3-dimensional continuous medium (dashed) is also shown (CAM 85).

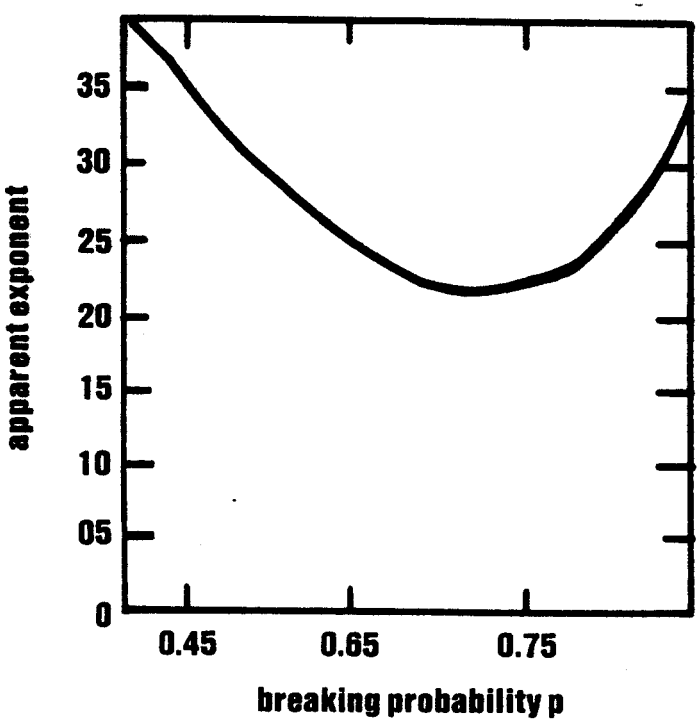

Figure 2.2.10. **The apparent exponent is plotted as a function of p, the probability of breaking bonds in the lattice (BAU 85).**

that the effective critical temperature associated with a percolation theory is $8(p_c/1 - p_c)^{1/2}$. Examination of three-dimensional systems yields a value $p_c \cong 0.7$ corresponding to a critical behavior in the vicinity of 12 MeV effective critical temperature. This result is in good agreement with the experimental data. It is, of course, incorrect to interpret this quantity as a true temperature; rather it allows the reader to relate this theory to the framework we have used to describe the data.

2.2.4 Complicating Factors

The preceding section dealt primarily with infinite nuclear matter properties. For real nuclei, there are a number of complicating factors which will lead to a misinterpretation of T_c from experimental data. In this section we explore a few of the most important factors.

The importance of surface properties can be deduced from observation of nuclear binding energies. We know that the binding energy per nucleon in real nuclei is approximately 8 MeV rather than the value of 16 MeV characteristic of nuclear matter. The nuclear force saturates and hence "sees" only neighbors within a given radius; a nucleon residing in the interior portion of a nucleus has a full complement of nearest neighbors whereas a nucleon residing near the surface has less than the allowable maximum of nearest neighbors. We assume here that the surface effects are the largest contributor to systematic errors in determining binding energies from nuclear matter considerations, though other effects will become

significant when discussing critical phenomena. If we reassess our estimation of the critical temperature we would estimate that $8.1 \leq T_c(\text{finite}) \leq 13$ MeV (JAQ 83; JAQ 84) while ρ_c remains essentially unchanged.

It is also important to comment that, even in finite matter, surfaces can exist such as a bubble interface with a liquid, or conversely a liquid droplet within a gaseous environment. At the critical point the free energy of the surface contribution is identically zero. Hence

$$F(T_c,\rho_c) = E(T_c,\rho_c) - T_c S(T_c,\rho_c) = 0 \qquad (2.2.21)$$

implying

$$T_c = \frac{E(T_c,\rho_c)}{S(T_c,\rho_c)} \quad .$$

Thus we see that the critical behavior is a true surface effect. Indeed this behavior is indicative of the condensation points (the coexistence-gas boundary) in general. It is obvious therefore that the surface effects are inherently important.

Coulomb and isospin asymmetry effects can also become important near the critical point since the differences between the "nuclear matter" pressure and the gas pressure tend to zero as does the surface pressure. Figure 2.2.11 illustrates the competing pressures within a droplet. As the system approaches the critical temperature, $P_{nm} - P_{gas} \to 0$ and $P_s \to 0$ leaving the Coulomb pressure unbalanced (BON 84). Examination of Figure 2.2.12 illustrates how this effect can alter the definition of an unbound droplet thus

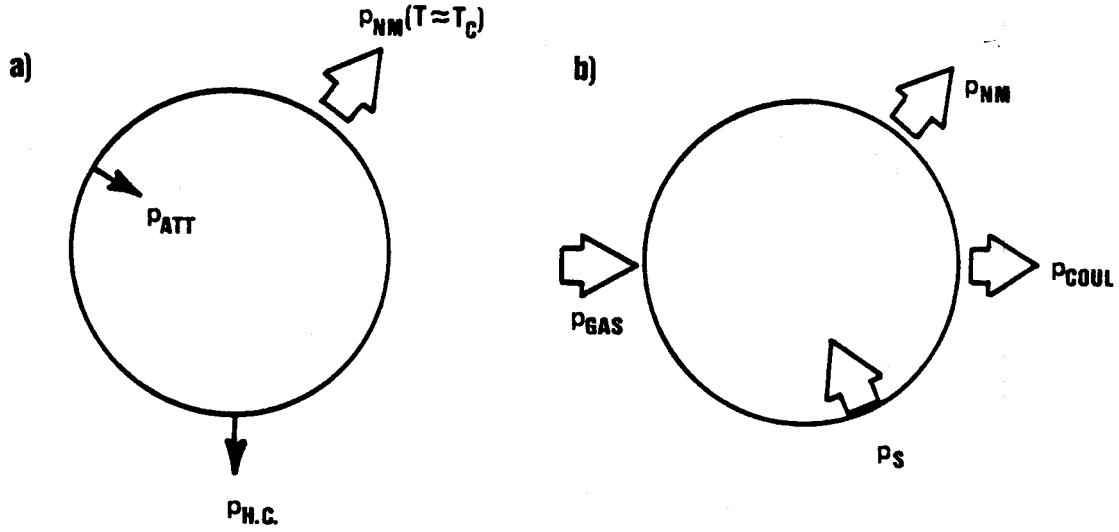

Figure 2.2.11. **The pressure on a nuclear droplet is illustrated. In a) the balancing attractive and hard core repulsive potentials which comprise the nuclear matter pressure are shown; and in b) the other pressures such as surface, Coulomb, and external gas pressures are shown.**

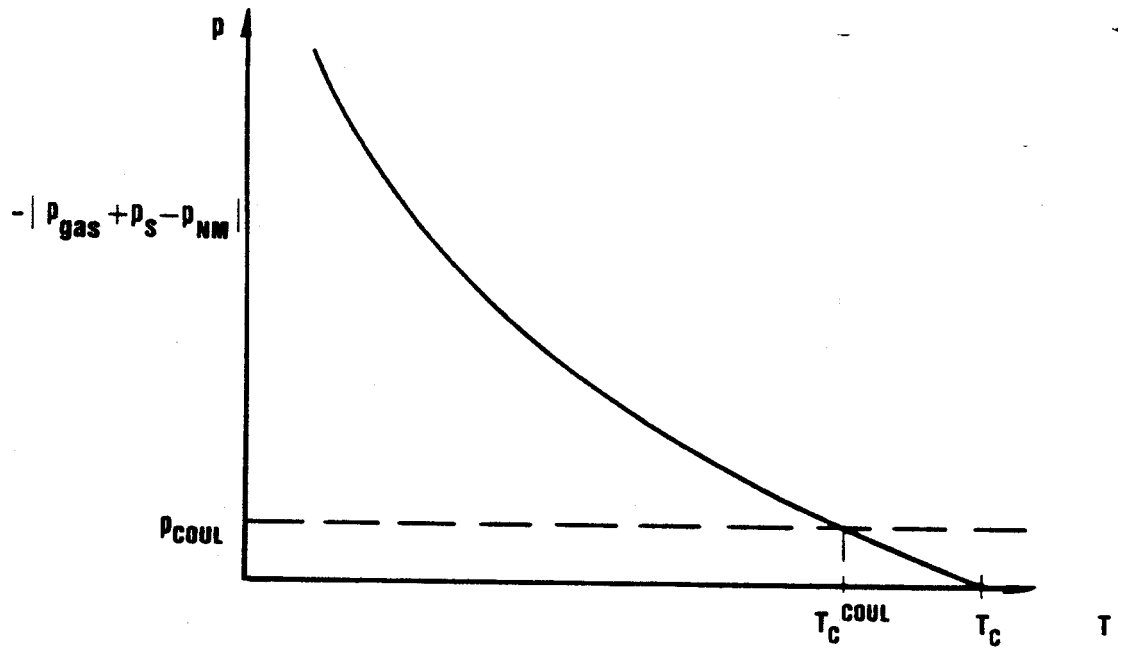

Figure 2.2.12. Pressure on a nuclear droplet (excluding the Coulomb pressure) as a function of temperature (solid line). As can be seen from observation of the critical behavior, the Coulombic pressure can be important. T_c^{COUL} is the critical temperature when Coulomb effects are taken into account.

causing an abrupt disassociation at T_c^{COUL} as opposed to a more gradual disassociation at T_c. The effect is most important near the critical point, since $P_{coul} >> P_{gas} + P_s - P_{nm}$.

It is important to note that as ρ_f decreases the internal Coulomb pressure will actually increase even though the average density decreases. This behavior arises because the density of the liquid, ρ_ℓ, increases as ρ_f decreases thereby increasing the proximity of the charged nucleons and enhancing the repulsion within the droplet. It is therefore conceivable that the Coulomb unbinding effects could propagate to regions far removed from the critical point.

The estimates of T_c range from 16-20 MeV (JAQ 84) in one phenomenological approach and between 8 and 13 MeV in another (BON 84). The discrepancies between different formulations are attributed to the imprecision inherent in the determination of the parameters based on information derived at $T = 0$ and $\rho = \rho_0$.

A further complicating factor comes from finite number effects which will tend to soften any abrupt transition. A thorough examination of this complication can be found in the work of Goodman et al. (GOO 83).

2.3 Mechanical Instability

2.3.1 General Formulation

In the preceding sections the unphysical portion of the pressure versus density isotherms were avoided by employing a Maxwellian construction to eliminate the undesired region ($K < 0$). The

motivation underlying this construction comes from the fact that the unphysical region is indicative of a chemical instability of the system at the phase separation. Such a chemical instability is not the only interpretation of the unphysical behavior of the nuclear equation of state. It is possible that matter might also undergo a mechanical instability similar to the shattering of hot nuclear matter (BER 83; CUR 83b).

We shall now describe the theory of a mechanical instability. The effects of damping are neglected initially; however these effects will be taken into account in Section 2.3.3. The derivation begins by evaluating the excitation energy per nucleon as a function of the density. First, the chemical potential must be derived from the density:

$$\rho = \frac{4}{(2\pi)^3}\int d^3k \left[1 + \exp\left(\frac{\frac{k^2}{2m} + E_V - \mu}{T}\right)\right]^{-1} \qquad (2.3.1)$$

where the potential energy is obtained from the Skyrme interaction (ignoring effective mass corrections):

$$\frac{E_V}{A} = -\bar{A}\left(\frac{\rho}{\rho_0}\right) + \bar{B}\left(\frac{\rho}{\rho_0}\right)^{5/3} . \qquad (2.3.2)$$

The constants $\bar{A}$ and $\bar{B}$ can be determined from nuclear matter properties in the following manner. The total energy is the sum of the thermal and potential energy contributions ($E = E_T + E_V$), which for $T = 0$ has the form

$$\frac{E}{A} = \frac{3}{5}\epsilon_F\left(\frac{\rho}{\rho_0}\right)^{2/3} - \bar{A}\left(\frac{\rho}{\rho_0}\right) + \bar{B}\left(\frac{\rho}{\rho_0}\right)^{5/3} \qquad (2.3.3)$$

where ϵ_F is the Fermi energy of normal nuclear matter ($\cong$ 38 MeV). Nuclear matter considerations require E = -16A MeV and $\partial(E/A)/\partial\rho = 0$ at $\rho = \rho_0$ and T = 0. The values obtained are $\bar{A}$ = 74.2 MeV and $\bar{B}$ = 35.4 MeV (CUR 83b). The thermal contribution to the system can be calculated using

$$\frac{E_T}{V} = \frac{4}{(2\pi)^3}\int d^3k\ \frac{k^2}{2m}\left[1 + \exp\left(\frac{\frac{k^2}{2m} + E_V - \mu}{T}\right)\right]^{-1} . \qquad (2.3.4)$$

Utilizing thermodynamics one can calculate the entropy and pressure from the following relations

$$S = \int_0^E \frac{dE}{T} \qquad (2.3.5)$$

$$P = \rho^2\left(\frac{\partial E}{\partial \rho}\right)_S . \qquad (2.3.6)$$

The results are presented in Figure 2.3.1, where several isentropes are plotted as a function of the density. From the initial excited compressed state formed in a heavy ion collision the system will oscillate along an isentrope in a harmonic fashion similar to a monopole oscillation in the absence of collision damping. If, during the oscillation, the pressure becomes positive then the system will disassociate. In practice, if the incident projectiles are protons or heavy ions they are expected to create conditions of

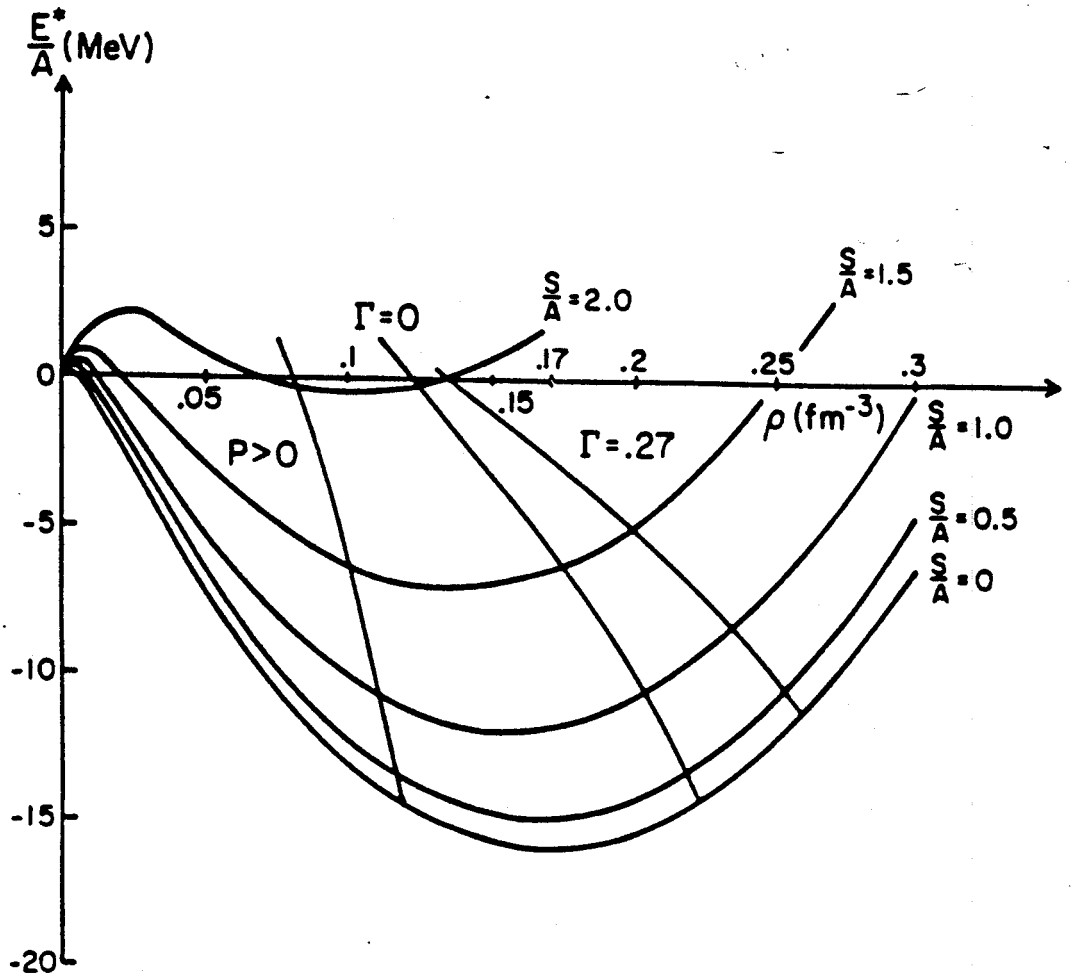

Figure 2.3.1. The energy per nucleon versus density for various values of the entropy per nucleon. The unstable region (P>0) is indicated. This region is defined by the condition that the system will evolve, or has evolved, to a condition such that the pressure remains positive; hence the system disassembles. Two boundaries for the overstressed region are drawn: no damping (labelled $\Gamma = 0$) and minimal damping ($\Gamma = 0.27$) (CUR 83b).

normal or greater than normal nuclear densities, respectively. It is therefore possible to define an overstressed region such that, under harmonic oscillation, the system will enter the region where the pressure will become positive on the return portion of the oscillation. The unstable ($P > 0$) region defines the conditions of temperature and density for which the system will disassemble and this region is also depicted in Figure 2.3.1.

To understand the conditions under which the system will disassemble it is necessary to refer to Figure 2.3.2 which illustrates the functional dependence of the pressure on the density. Focusing attention on the isentrope with $S/A = 0$ it is seen that for normal nuclear density the pressure is zero as expected. Decreasing density corresponds to decreasing pressure until a maximal negative pressure point is reached, whereupon the pressure increases with further decrease of the density. Once the pressure exceeds zero the pressure of the system remains positive for all further decrements in the density. Stable equilibrium is attained only when the pressure is zero and where the energy is a local minimum. A system, characterized by values of ρ and S/A, such that it is located along the negative incompressibility portion of the isentrope (indicated in Figure 2.3.2), will move toward the lower density, zero pressure point. Once the system attains zero pressure it has acquired an outward momentum and the energy is not a local minimum; hence the system continues to expand until the density approaches zero (see Figure 2.3.3). Therefore the boundary of the unstable zone is

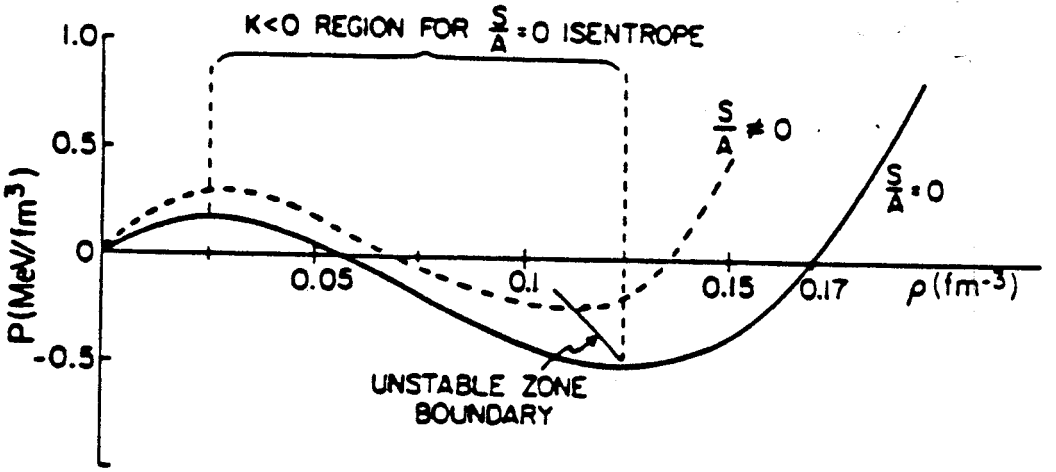

Figure 2.3.2. **Pressure versus density is plotted for S/A = 0 and S/A ≠ 0 isentropes to illustrate the dynamical reasoning utilized in defining the unstable region boundary. The negative incompressibility region of the S/A = 0 isentrope is indicated to identify the portion of the isentrope for which the system will evolve to lower densities and increasing pressure until the pressure becomes postive. Since the pressure remains positive for all lower densities the system is unstable. The unstable region boundary deduced from different isentropes was discussed for Figure 2.3.1 (CUR 83b).**

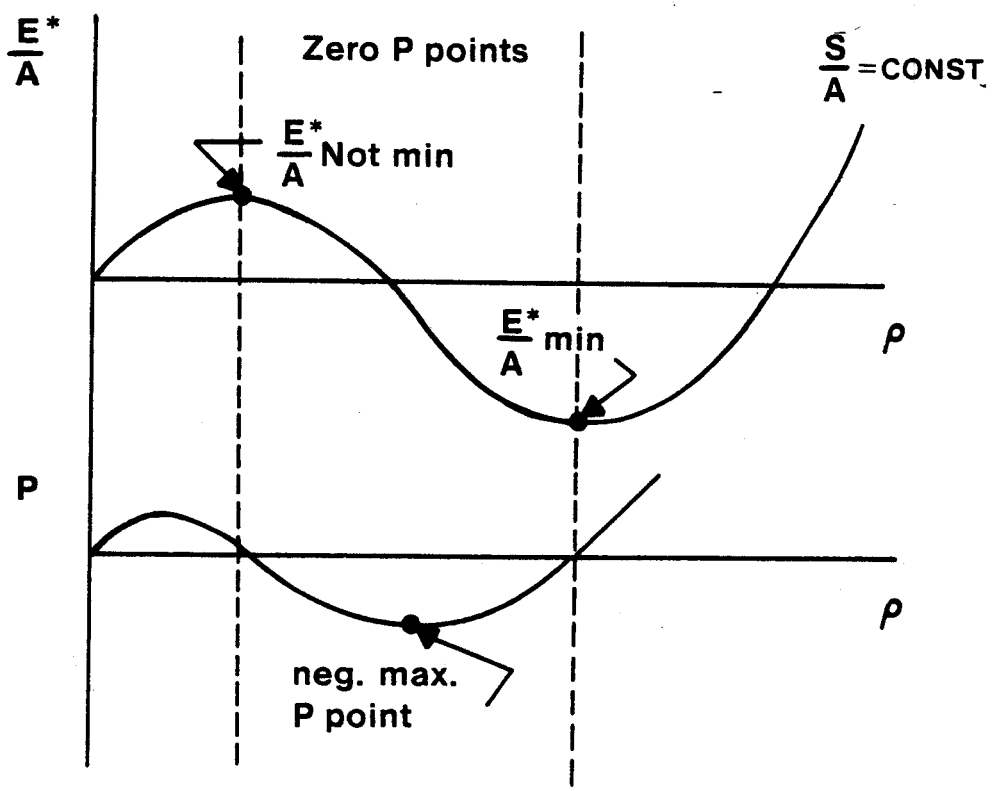

Figure 2.3.3 **The excitation energy per nucleon and pressure are shown for a given isentrope as a function of the density. The excitation energy extrema are depicted and the corresponding zero pressure points to illustrate their stable and unstable nature described in the text.**

defined by successive points of maximal negative pressure for increasing isentropes (see Figure 2.3.2).

The system still possesses negative excitaiton energy and therefore is likely to disassemble into light bound clusters. Since a deuteron is favored from entropy considerations, but is severely disfavored energetically, it is most likely that the system will disassemble into slightly heavier fragments, most probably alpha particles.

2.3.2 Experimentally Determinable Quantities

One experimentally determinable feature may be the relatively rapid onset of deuteron and proton production. The region of instability encompasses a region of negative excitation energy which indicates that the resultant breakup must produce bound clusters consistent with the average negative excitation energy at the unstable boundary. We note that the α-particle has an average binding energy of 7.1 MeV/nucleon which is commensurate with the average binding energy per nucleon of heavier nuclei and yet is still favored by considerations of entropy. As the incident energy is increased, the entropy and temperature also increase, thereby increasing the average kinetic energy of the participants, where they become less off shell. Once the average negative excitation energy is $\cong$ 1 MeV/ nucleon, deuteron production becomes feasible. With a small additional investment of incident energy the individual nucleons will come on shell resulting predominantly in nucleon production.

Another feature of the mechanical instability is the expected marked difference between proton and heavy ion induced reactions. Proton induced reactions prepare the system essentially at ρ_0, i.e. with no compression, whereas the heavy ion induced reaction may lead to significant compression and a reduction of the incident energy per nucleon necessary to traverse the boundary of the overstressed region.

Since proton induced collisions will not produce an initial compressed system, any subsequent oscillation would appear to be prohibited. One must note, however, that the oscillation occurs because the system is at a nonequilibrium density. In a proton induced collision, the entropy increases but the density remains essentially constant. However, the equilibrium density for an isentrope decreases as a function of increasing entropy. In other words, the equilibrium density of the new isentrope ($S/A \neq 0$) moves out from under the point of normal nuclear density and zero entropy.

To adequately describe the behavior within this framework, the system should have an entropy such that $S/A < 2$; the dynamics become featureless for larger entropies (BER 81; BER 83). The intermediate energy regime should therefore provide an ideal experimental testing ground for such an instability.

2.3.3 Caveats

There are at least three obvious complicating factors which may obscure the manifestation of the mechanical instability in heavy ion collisions.

Firstly, damping will modify the conclusions (CUR 83b). The empirical full width at half maximum (FWHM) of the monopole excitation is typically 4 MeV for an excitation energy of 15 MeV (YOU 81). Let us define the damping constant Γ as the ratio of the full width at half maximum of the monopole excitation and the excitation energy of the oscillation. In Figure 2.3.1 the overstressed region is redefined assuming that the damping constant remains fixed at $\Gamma = 0.27$ (reflecting $T = 0$ damping) and is not a function of temperature. Note that the minimum temperature required for the system to reach the unstable region can be determined from information contained in Figure 2.3.1. The minimum excitation energy of the overstressed region occurs at the intersection of the overstressed region boundary and the $S/A = 0$ isentrope. Since energy is conserved, the line of constant energy can be followed to the boundary of the unstable region, allowing the corresponding temperature to be deduced from the corresponding density and energy. The resulting minimum observable temperature for a disassembly of this nature is 5.5 MeV. This is the minimum amount of energy transferred from the collective motion to the random thermal motion, consistent with the damping deduced from the width of the monopole oscillation. This damping process also generates entropy, the minimum values of which can be calculated in a fashion similar to the minimum temperature; the final entropy at the boundary of the unstable region is 0.9. Hence a mechanical instability generates a minimum temperature of 5.5 MeV and a minimum entropy of 0.9 prior to disassembly. The

minimum excitation energy of the overstressed region is 4.75 MeV above the binding energy of normal nuclear matter (E = -16A MeV) and $\rho \cong 1.5\ \rho_0$. The minimum incident energy required for an equal mass projectile and target system is 4 times this excitation energy, i.e. 19A MeV. If this incident energy is insufficient to generate a system of $1.5\ \rho_0$ then the experimental minimum will be even larger (CUR 83b). Initial entropies of greater than 2.0 appear to be much less affected than lower values of the initial entropy; hence our results do not contradict the cascade model calculations performed at higher energies which predict that entropy remains essentially constant during the expansion process (BER 81).

A second complication concerns possible coupling to the continuum, more commonly referred to as evaporation. This process may modify the conclusions on account of the fact that the evaporated particles carry away energy and modify the density and entropy profiles. Since the evaporation time is comparable to the expansion time, the probability of evaporating a nucleon is significant (CUR 83b). The evaporation also affects the treatment of damping, leading to the following modification. The damping constant ($\Gamma \cong 0.27$) is attributable to both the damping and coupling to the continuum in approximately equal partitioning. The monopole oscillation is a $T \cong 0$, small amplitude phenomenon, while the large amplitude oscillation occurs at much higher temperatures; thus the Pauli Blocking factor is reduced hence further enhancing the collision damping aspects. Thus, as we move generally upward on the

energy and pressure versus density diagram it is anticipated that collision damping will become increasingly important.

Thirdly, there exists the possibility that a liquid-gas phase transition may develop as we discussed in Section 2.2, thus modifying the behavior expected in our simple treatment of a mechanical instability.

2.4 Time Scales

2.4.1 Thermal Equilibration

First, we will obtain an estimate of the time required for thermalization and then compare this time to the time required for the system to disassemble based on experimentally determined excitation energies of monopole oscillations. Estimating the time required for thermalization from the average velocity of the nucleons and the mean free path yields

$$t_{equil} \cong \left(\frac{1}{\rho\sigma_{NN}}\right) \cdot \frac{1}{v} \qquad (2.4.1)$$

where σ_{NN} ($\cong$ 20 mb) is the average nucleon-nucleon cross section corrected for Pauli Blocking (DIG 80). The average velocity of the incoming projectile in the intermediate energy regime, (20A MeV $\leq E_{inc} \leq$ 100A MeV), is $0.7v_F \leq v_{inc} \leq 1.6v_F$, while the average nucleon velocity of a target nucleon is $\cong 0.8v_F$. Hence $v \cong v_F$ is a reasonable value to assign v in eq. (2.4.1). The density varies depending on the projectile; a minimum density of

$\rho \cong \rho_0 = 0.17\ fm^{-3}$ will be considered here. The resulting equilibrium time is

$$t_{equil} \cong 3 \cdot 10^{-23}\ sec \qquad (2.4.2)$$

which is less than or of the order of the nuclear transit time for intermediate energy projectiles.

Comparison of the derived equilibrium time estimate with the compression and subsequent expansion times will indicate whether thermalization is relevant to the present discussion (CUR 83b). Since a harmonic oscillator period is amplitude independent it is possible to draw an analogy between the small amplitude monopole oscillation and the large amplitude oscillation encountered in the compression and expansion phases of the participant region of a heavy ion collision. More sophisticated calculations of the large amplitude oscillation are in general agreement with the estimation made here (CUG 84b). The energy associated with monopole oscillations in medium mass nuclei is (YOU 81),

$$E_{monopole} \cong \hbar\omega_0 \cong 15\ MeV \qquad (2.4.3)$$

resulting in a half oscillation period,

$$\tau_{monopole} = \frac{\pi}{\omega_0} \cong 1.4 \cdot 10^{-22}\ sec \qquad (2.4.4)$$

which is consistent with cascade estimates of disassembly times (KRU 83). Note that the thermal equilibration may also take place along the compression phase of the oscillation.

Since the thermal equilibration time is a factor of 10 smaller than the corresponding oscillation period of the system, the thermal models are not inconsistent with the time scales associated with the decay of the participant region.

2.4.2 Chemical Equilibration

As we discussed previously, it is also possible that during the process of rarefaction, following the initial compression, the system may enter a state of lower than normal nuclear density, where the conditions of temperature and density necessary for a liquid-gas coexistence may develop. If heavy ions are to be adequate probes of these states, two conditions must be satisfied: the thermalization time and the time necessary for this state to develop must be less than or of the order of the disassembly time. Firstly, we assume that the system has a sufficiently short mean free path to allow the system to equilibrate in a time commensurate with the collision time of the heavy ions (see the preceding section). Secondly, any phase transition, for example a liquid-gas phase instability, must establish itself prior to disassembly if it is to have a discernible experimental consequence. It is important therefore to estimate the time scale for the system to disassemble and to compare it with the time scale necessary for the establishment of chemical equilibrium (CUR 83b).

If a "chemical" instability, such as a liquid-gas phase instability, is to exist there must be sufficient time for equilibration to be established across the phase boundary. The time required for

this equilibration to occur is of the same order as the evaporation time. To estimate the evaporation time we use the expression characteristic of thermionic emission. Thus, the current density can be expressed as (BLA 74),

$$J = \frac{em}{2\pi^2\hbar^3} T^2 (1 - r) e^{-W/T} \qquad (2.4.5)$$

where r is the quantum mechanical reflection coefficient (taken as 0), W is the work function (taken between 0 MeV and 8 MeV), and T is the temperature. By definition

$$J = \frac{\Delta q}{\Delta t} \cdot \frac{1}{A} \qquad (2.4.6)$$

where A is the surface area of the emitting source. If we set $\Delta q = e$ (equivalent to the emission of one nucleon) then $\Delta t = \tau_{evap}$. Assuming a spherical geometry, so that $A = 4\pi R^2$ where $R \cong 3.5$ fm as determined from the participant-spectator model for intermediate impact parameters (SCO 81) and consistent with determinations from pion interferometry measurements (NAG 81), the evaporation time for a single nucleon is found to be,

$$\tau_{evap} \cong 3.5 \times 10^{-21} \frac{1}{T^2} \cdot e^{W/T} \quad (\text{sec}) \quad . \qquad (2.4.7)$$

The resulting values are given in Table 2. The values for W = 8 MeV are in good agreement with results deduced from empirical

Table 2. Nucleon evaporation times as a function of temperature assuming work functions of 8 MeV and 0 MeV.

T (MeV)	5	10	15	20
t ($\times 10^{-22}$ sec), W = 8 MeV	6.9	0.78	0.27	0.13
t ($\times 10^{-22}$ sec), W = 0 MeV	1.4	0.35	0.16	0.09

fits to the measured widths of compound nuclei for A = 20-100 (BOH 70). Comparing the evaporation time with the time required for disassembly we find that for $T \geq 8.1$ MeV (henceforth referred to as the breakeven temperature for W = 8 MeV) the liquid-gas phase instability may develop. The range of breakeven temperatures, deduced from work functions of 0 MeV and 8 MeV, are given in Table 3 as a function of sequential evaporation times required to achieve chemical equilibrium.

Since the liquid-gas phase instability exists only for temperatures below the critical temperature and above the breakeven temperature, it is likely that if the breakeven temperature were higher than the critical temperature, the liquid-gas instability would never develop. The critical temperature of 20 MeV, predicted in (CUR 83a), assumed a binding energy per nucleon in nuclear matter of 16 MeV compared to the phenomenological binding energy per nucleon of 8 MeV for finite nuclei. A more thorough treatment of this question and of effective mass considerations is given in (JAQ 84), where it is shown that in finite nuclei the predicted critical temperature lies between 8.1 MeV and 13.4 MeV depending on the choice of effective mass. Thus for temperatures above 8 MeV the liquid-gas instability may develop and there is sufficient time for it to do so.

A more thorough treatment is given by Cugnon (CUG 84b) where the incompressibility is allowed to vary as a function of the density. The times for the decompression phase alone are,

Table 3. Breakeven temperatures as a function of the number of sequential evaporations and the work function. The numbers in parentheses are breakeven temperatures determined from an estimate of the time scale of $\cong 5 \cdot 10^{-22}$ sec (CUG 84b).

No. of sequential evaporations	Minimum $T_{b.e.}$ (MeV) (W = 0 MeV)	Maximum $T_{b.e.}$ (MeV) (W = 8 MeV)
1	5.0 (2.6)	8.1 (5.5)
3	8.7 (4.6)	12.1 (7.7)
10	15.8 (8.4)	19.4 (11.8)

$$t_{expansion} \cong 3\text{-}5 \cdot 10^{-22} \text{ sec} \qquad (2.4.8)$$

which are approximately a factor of 2-3 times larger than in the harmonic oscillator approximation. This is expected since, by definition, the unstable solution must enter the region where $K < 0$, i.e. where the restoring force will become zero. Thus the "oscillation" period tends to infinity, whereas in the harmonic oscillator approximation, K is a constant determined by the curvature of the isentrope at the equilibrium density, which in the monopole example is $K(\rho = \rho_0) = 210$ MeV. The breakeven temperatures are calculated (CUR 83b) for several cases utilizing the results obtained when these effects are incorporated. It is interesting to note from Table 3 that emission could occur (without damping) at T = 2.6 MeV.

Collision damping has been neglected throughout this discussion. As mentioned earlier, damping will not alter the definition of the unstable region, however it will alter the definition of the overstressed region. A simple approach to the problem begins with the equation for a damped, nondriven oscillator,

$$\ddot{x} + \gamma\dot{x} + \omega_0^2 x = 0 \qquad (2.4.9)$$

where

$$x = \rho - \rho_{min}(S)$$

and γ is the viscous damping coefficient. In addition, we define

$$\bar{\Gamma} = \frac{\gamma}{(\omega_0^2 - \frac{\gamma^2}{4})^{1/2}} \quad .$$

where $\bar{\Gamma}$ is the damping coefficient (assumed constant) and ω_0 is frequency of the undamped harmonic oscillator.

The damping factor results in an enhancement of the time required for the system to reach the breakup region. The enhancement factor is

$$\Delta\tau = \tau - \tau(\bar{\Gamma} = 0) = [(1 + \frac{1}{4}\bar{\Gamma}^2)^{1/2} - 1] \quad \tau(\bar{\Gamma} = 0) \tag{2.4.10}$$

resulting in an enhancement of about 37%. Since Pauli Blocking decreases with increasing temperature, the damping constant should also increase, further increasing the time available for chemical equilibration. The effects of different damping constants are tabulated in Table 4.

In concluding this section, it is interesting to note that recent TDHF calculations, which are much more sophisticated than the simple treatments given here, show a fragment clustering that may signal droplet formation setting in at times of $\cong$ 48 fm/c or $1.6 \cdot 10^{-22}$ sec (STR 84).

Table 4. Breakeven temperatures for various values of the normalized damping constant and work function assuming emission of a single nucleon.

$\bar{\Gamma}/\Gamma$ ($T \cong 0$)	0	5	10	20
$T_{breakeven}$ (MeV), W = 8 MeV	8.1	7.6	6.9	5.8
$T_{breakeven}$ (MeV), W = 0 MeV	5.0	4.6	3.9	2.9

CHAPTER 3

OTHER THEORIES AND COMPLICATING FACTORS

3.1 Introduction

In this chapter, we focus on other theories which predict complex fragment yields. These approaches do not rely on the mechanical and chemical instabilities characteristic of the theories described in the previous chapter. Complicating effects which make experimental measurements difficult to interpret are also discussed. Firstly, the conventional statistical models are described. The single phase thermal and coalescence model assumptions and predictions are stated. Although these models give similar predictions, they are based on different physical interpretations which are explored. These approaches are followed with a description of binary reactions. In particular, compound nucleus fission is described and the basic predictions are given. Thirdly, the cold shattering model is considered. This two step dynamical process is explained and the assumptions inherent in the yield predictions are given. A contrast between the predictions of complex fragment yields of this model and the macroscopic liquid-gas model is pointed out. Finally, complicating factors which obscure the ready interpretation of experimental results with the theories currently available are considered. Coulomb tunneling effects are predicted

and their characteristic behavior compared to the data. Although the system "freezes out" as it expands which, as we noted in Chapter 2, indicates that the fragments no longer interact, sequential decays can continue to change the primary distributions. Therefore, these effects are also touched upon. A discussion of in-medium effects is also given in this section.

3.2 Conventional Statistical Models

3.2.1 Classical Single Phase Thermal Model

If the incident energy is sufficiently large ($E \geq 400A$ MeV) the emission in the source rest frame may be adequately described by a Boltzmann distribution. In the momentum representation (MEK 81),

$$\frac{d^3N_A}{dp_A^3} = \frac{V}{h^3} g_A e^{(\mu_A - \varepsilon_A)/T} \tag{3.2.1}$$

where g_A is a spin degeneracy factor, A is the mass of the composite fragment, and Z, N are the number of protons and neutrons respectively.

Assuming

$$\mu_A = N\mu_n + Z\mu_p \qquad \varepsilon_A = N\varepsilon_n + Z\varepsilon_p$$

$$M_A \cong NM_n + ZM_p \tag{3.2.2}$$

$$p_A = Ap_p \qquad p_p = \text{momentum of a proton}$$

we obtain

$$\frac{d^3N_A}{dp_A^3} = \frac{V}{h^3} g_A e^{(Z\mu_p + N\mu_n)/T} e^{-\varepsilon_A/T}$$

$$= \frac{V}{h^3} g_A (\lambda_p e^{-\varepsilon_p/T})^Z (\lambda_n e^{-\varepsilon_n/T})^N \qquad (3.2.3)$$

$$= \frac{V}{h^3} g_A \left(\frac{h^3}{Vg_p} \cdot \frac{d^3N_p}{dp_p^3}\right)^Z \left(\frac{h^3}{Vg_n} \cdot \frac{d^3N_n}{dp_n^3}\right)^N .$$

Furthermore, it is assumed that the momentum distributions of neutrons and protons are identical apart from a constant scale factor, R_{np}, which reflects the ratio of neutrons to protons present in the system. Thus,

$$\frac{d^3N_A}{dp_A^3} = \left(\frac{h^3}{V}\right)^{A-1} \frac{g_A}{2^A} R_{np}^N \left(\frac{d^3N_p}{dp_p^3}\right)^A . \qquad (3.2.4)$$

3.2.2 Coalescence Model

In contrast to the single phase gaseous thermal model of the preceding section, we now explore a coalescence model prediction of complex fragment production. A comparison is made between the two models at the end of this section.

The coalescence model is based on the assumption that any proton and neutron emitted with a relative momentum less than $p_0(d)$, the maximum coalescence momentum consistent with deuteron production, will coalesce to form a deuteron. Similarly, if a proton and

two neutrons are emitted whose relative momenta all lie within a sphere of radius $p_0(t)$, the maximum coalescence momentum consistent with triton production, a triton will be formed. If all composites are formed in this manner then the coalescence radii are inherent properties of the composite produced and are independent of the size of the projectile and target.

The predicted distribution of this theory (MEK 81) is

$$\frac{d^3N(Z,N)}{dp_p^3} = \left(\frac{N_t + N_p}{Z_t + Z_p}\right)^N \cdot \frac{(\frac{4}{3}\pi p_0^3)^{A-1}}{Z!N!} \cdot \left(\frac{d^3N_p}{dp_p^3}\right)^A \qquad (3.2.5)$$

where

N_t = number of neutrons in the target

N_p = number of neutrons in the projectile

Z_p = number of protons in the projectile

Z_t = number of protons in the target

N = number of neutrons in the composite

Z = number of protons in the composite

A = number of nucleons in the composite .

Caution must be used when interpreting the coalescence radius, p_0, since it contains at least two implicit factors. For two particles to form a deuteron the spin assignments must also be correct. Most light nuclei have no bound excited states, and therefore the portion of randomly oriented spins having the correct combinations to form a ground state composite is $(2S + 1)/2^A$. Thus we may define

a "new" coalescence radius ($\tilde{p}_0$) which has the geometrical factors removed in the following manner:

$$(p_0^3)^{A-1} = A^3 \cdot \frac{(2S+1)}{2^A} \cdot (\tilde{p}_0^3)^{A-1} \quad . \tag{3.2.6}$$

Thus we arrive at a result similar to the thermodynamical model, i.e.

$$\frac{d^3N(Z,N)}{dp_p^3} = \left(\frac{N_t + N_p}{Z_t + Z_p}\right)^N \cdot A^3 \cdot \frac{(2S+1)}{2^A} \cdot \frac{(\frac{4}{3}\pi\tilde{p}_0^3)^{A-1}}{Z!N!} \cdot \left(\frac{d^3N_p}{dp_p^3}\right)^A \quad . \tag{3.2.7}$$

Figures 3.2.1a and 3.2.1b contrast the different physical interpretations of the related volumes in the two models. The coalescence volume ($\tilde{p}_0 \cong h/[2\pi L]$ from the uncertainty principle) is characteristic of the composite system formed, whereas the thermal freeze out volume is the volume at which the mean free path of a participant is commensurate with size of the system, i.e. the participants no longer collide and exchange energy and momentum.

Both the single gaseous and coalescence models predict that the cross section for producing a fragment of mass A depends on the cross section for a single nucleon raised to the power A. However, as can be ascertained from Figure 3.2.2, this behavior is exhibited only at incident energies in excess of 150A MeV, where the fragment yield does indeed fall off monotonically with increasing mass in

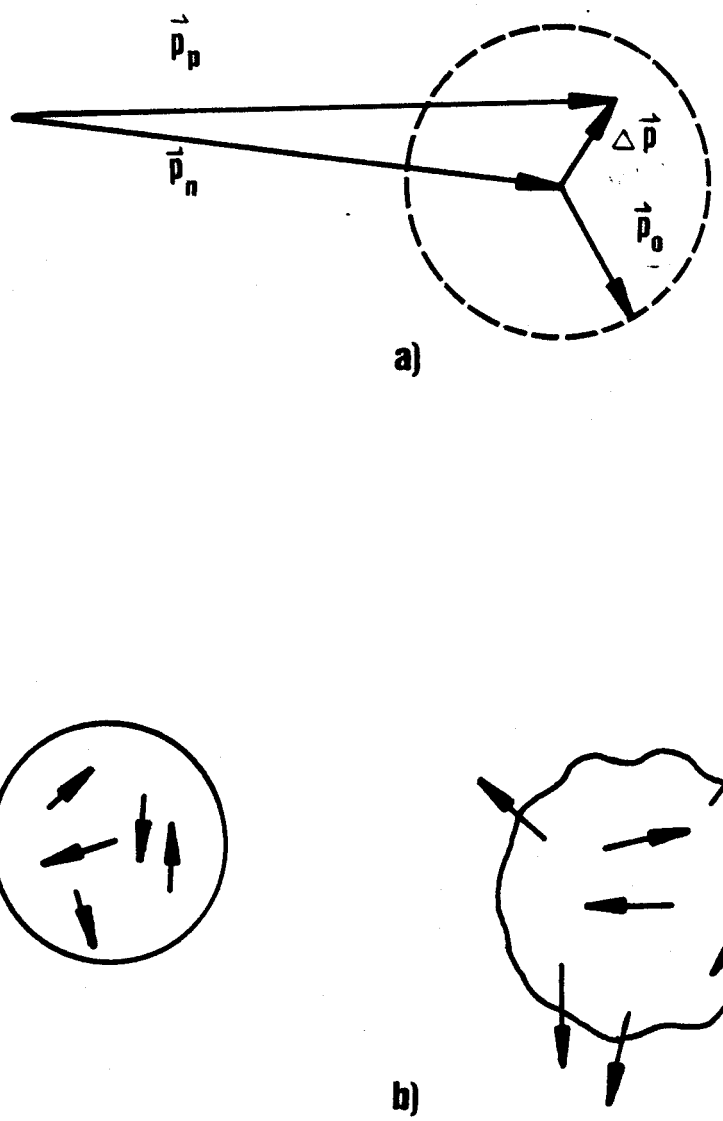

Figure 3.2.1. **Physical interpretations of a) the coalescence momentum space representation where p_p and p_n are the proton and neutron momenta and b) the physical space representation of the single phase thermal model as a function of time.**

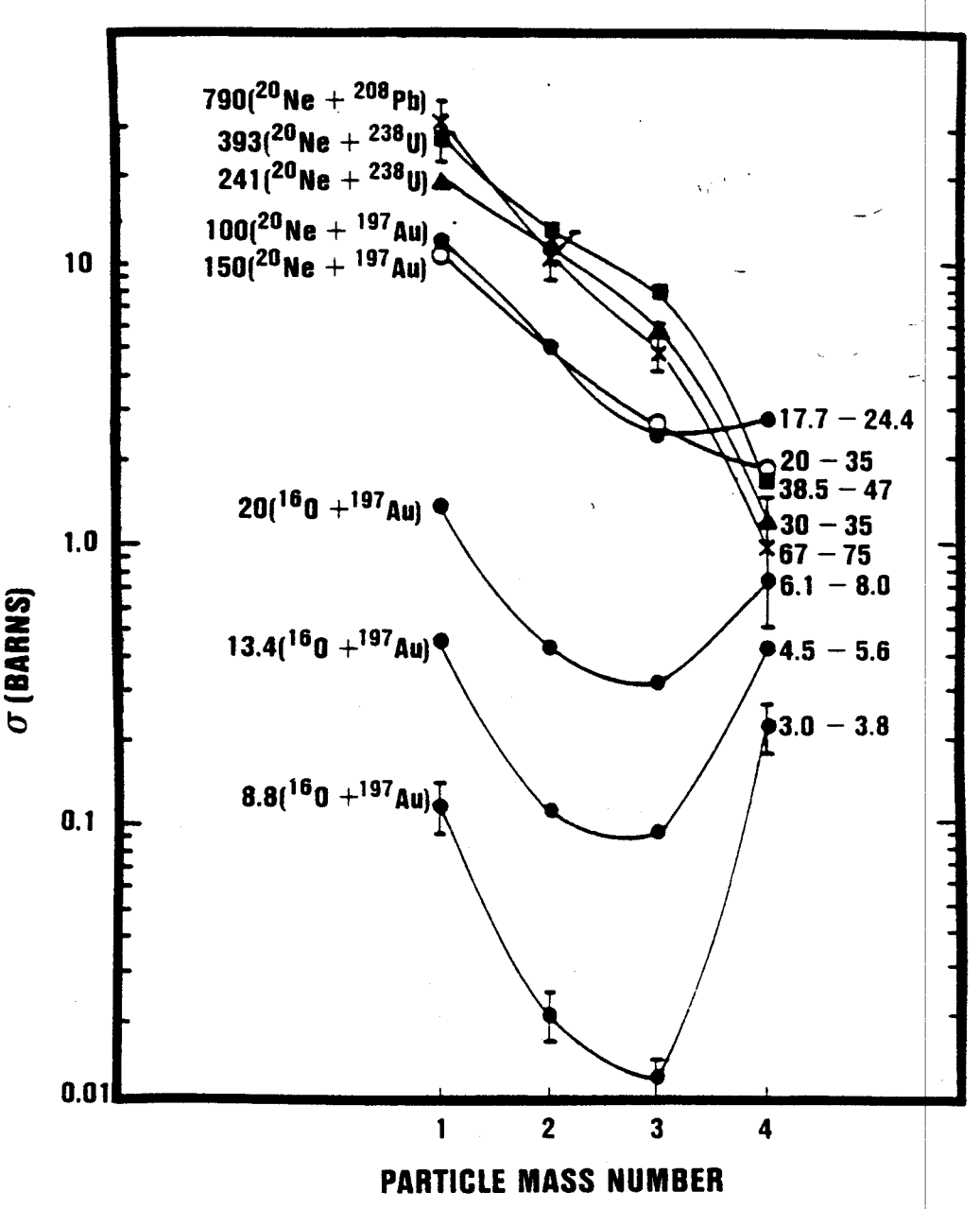

Figure 3.2.2. **Cross-sections for the production of light fragments (A=1–4) in reactions induced by ^{20}Ne and ^{16}O are plotted for a range of incident energies (shown on the left) and equivalent temperatures (right). Error bars are indicated for highest (x) and lowest (●) incident energies.**

contrast to the behavior at lower incident energies (CUR 82a). The behavior at energies below 150A MeV indicates the presence of other reaction mechanisms. Indeed, the increase in α-particles provided the original motivation for exploring the liquid-gas phase transition. However, there can also exist ambiguities due to binding energy considerations, as discussed by Curtin et al. (CUR 82b; CUR 83a), which led to the idea that measurements of heavier fragments would be required to resolve the ambiguities.

3.3 Compound Nucleus Fission

The principle focus of this thesis is on multifragmentation. However, it is important when discussing inclusive yield measurements to bear in mind also the possibility of binary reactions. For example, a compound nucleus may form (for simplicity we assume the $\ell = 0$ case) and then proceed to fission after reaching global equilibrium.

The energy required to liberate a fragment of charge Z_F and mass A_F from the recoiling system (Z_R, A_R) is (NOR 80)

$$\Delta E = E(Z_F,A_F) + E(Z_R,A_R) + V_{CB} - E_{(CN)}(Z_{TOT},A_{TOT}) \; . \qquad (3.3.1)$$

In the liquid droplet model,

$$E(Z,A) = [1 - 1.79(\frac{N - Z}{A})^2] \; . \; (-a_v A + a_s A^{2/3}) + \frac{3}{5} \frac{e^2 Z^2}{r_0 A^{1/3}}$$

$$- \frac{\pi^2}{2} \frac{e^2}{r_0} (\frac{\alpha}{r_0})^2 \frac{Z^2}{A} \qquad (3.3.2)$$

where

a_v = 15.677 MeV $\qquad$ r_0 = 1.205 fm

a_s = 18.56 MeV $\qquad$ α = .546 fm .

The Coulomb Barrier energy in the approximation of touching spheres is,

$$V_{CB} = \frac{1.44\ Z_F Z_R}{0.5 + 1.36(A_F^{1/3} + A_R^{1/3})} \quad \text{(MeV)}. \tag{3.3.3}$$

The results of the calculation of ΔE in eq. (3.3.1) are displayed in Figure 3.3.1. The yields are anticipated to behave as (SOB 85b; MOR 85)

$$\sigma_F = \sigma_0 \exp(-\Delta E/T_{CN}) \tag{3.3.4}$$

where T_{CN} is the compound nucleus temperature. Also, in this type of reaction, $d\sigma/d\Theta$ plotted versus $\Theta_{C.M.}$ of the compound system will be flat.

3.4 Cold Shattering Model

Another possible interpretation of intermediate mass fragment production in heavy ion collisions involves the breakup of the cold spectator residues (AIC 84a; AIC 84b). The basic idea is as follows. A high energy projectile impinges upon a stationary target which reaches thermal equilibrium and creates a hot, dense fireball involving the geometrically overlapping nucleons referred to as

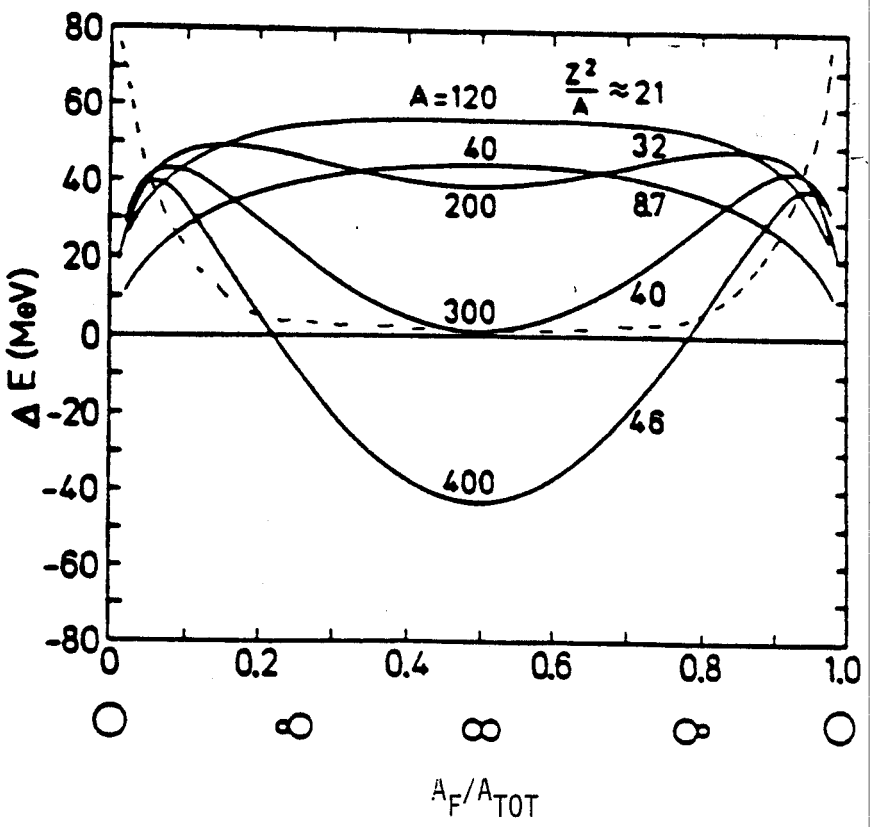

Figure 3.3.1. **The energy released in compound nucleus formation as a function of the ratio of emitted fragment charge to the total compound nucleus charge. The cross-sections are assumed to vary as $\sigma_z = \sigma_0 \exp(-\Delta E/T)$ and are indicated for A = 120 by the dashed line (NOR 80).**

participants. The fireball proceeds through the surrounding cold nuclear matter causing global destabilization and emitting nucleons into the spectator material. The nucleon velocity distribution is assumed to have a Maxwellian form characteristic of the fireball temperature. If, perchance, the mean free path is sufficiently short, then the nucleon may be absorbed, thus creating a local excitation which, if coupled with the global destabilization, may be great enough to overcome the Coulomb Barrier. A fragment can subsequently be emitted. The destabilized matter then cracks and breaks apart emitting large, relatively cold pieces of nuclear matter with kinetic energy imparted to the system from the participant nucleon minus the energy required to break the requisite nuclear bonds in liberating the fragment. The fragment may also evaporate a few nucleons since it is excited, albeit at a low level. The participant region will decay essentially emitting light particles (protons to alphas). This type of breakup has been described as analogous to the shattering of glass.

One of the significant differences between this model and the models of the mechanical and chemical instabilities presented in the preceding chapter is that the primary distribution of fragments is composed of essentially cold nuclear matter. Hence it should give rise to less sequential emission than the correspondingly hotter primary fragments produced in the theories of chemical and mechanical instability. The emitting source is also moving slower than the counterpart in the other theories. In the event this model

is correct, then heavy fragment production has no relevant informational content regarding nuclear matter under extreme conditions but is rather an artifact of the type of probe we are utilizing, i.e. heavy ion collisions.

The shape of the yield versus charge curve can be derived from maximal entropy considerations and charge conservation. The physical mechanism consists of a simple two step process. First, the projectile drills a hole in the target nucleus knocking out Z_{fast} nucleons in the forward direction and leaving Z_0 nucleons in the system, where

$$Z_0 = Z_P + Z_T - Z_{fast} \cdot \tag{3.4.1}$$

Secondly, the system of Z_0 charges decays into any possible combination of fragments thus maximizing the entropy. The prediction of yields as a function of fragment charge for this theory is

$$\sigma(Z) = \frac{\sigma_0}{e^{1.28Z/\sqrt{Z_0}} - 1} \cdot \tag{3.4.2}$$

We note that if the condition

$$\frac{1.28Z}{\sqrt{Z_0}} >> 1 \tag{3.4.3}$$

holds then the last term of the denominator in eq. (3.4.2) is negligible; hence

$$\ln\sigma \cong -\frac{1.28}{\sqrt{Z_0}} Z + \ln \sigma_0 \ . \qquad (3.4.4)$$

Thus, we see that there exists a marked difference between the prediction of this theory and a liquid-gas theory which gives rise to the form (see eq. (2.2.17) and Fisher (FIS 67)),

$$\ln \sigma \cong -\tau \ln Z + \ln \sigma_0 \ . \qquad (3.4.5)$$

Eq. (3.4.2) should exhibit an approximately linear behavior for large Z with slight upward curvature for the low Z fragments when displayed on a semi-log plot.

3.5 Complicating Factors

3.5.1 Introduction

The ensuing discussion will emphasize the mechanisms that may disturb the system before freeze out. One effect that influences nuclear matter possessing a net charge is Coulomb Tunneling. Another effect which influences physical observables prior to freeze out is the in-medium corrections. Since actual experimental observables are measured at macroscopic distances ($\rho \cong 0$), it is also necessary to bear in mind that the subsequent, post-freeze-out behavior of the system may effect the actual measurement. One possibility is that subsequent evaporation effects could alter the resultant distribution, thus shifting the average fragment mass to lower values. The anticipated effects of these processes will be elaborated upon in the following sections.

3.5.2 Coulomb Tunneling Effect on Mass Yield

The effect of Coulomb Tunneling as a function of mass, or more specifically of charge, and of energy of the emitted fragment is derived in this section. (More extensive treatments are given by Boal (BOA 84a).)

In a nucleus-nucleus collision, the nucleons which undergo a sufficient number of multiple scattering processes will thermalize. We assume a Boltzmann-like distribution with a primary mass distribution of the form A^{-k}, where k is a constant independent of incident energy. Since the Coulomb Barrier that a given fragment experiences is dependent on its charge and on the charge of the remnant, the resultant distribution will depend on Z_f and A_f. Assuming that the fragment N/Z ratio reflects the projectile-target combination, A_f can be deduced for any Z_f value. The dependence on incident energy arises since the distance through which the fragment must tunnel decreases as a function of increasing fragment energy. As the incident energy increases the temperature will increase thus populating higher energy states more frequently and reducing the attenuation due to Coulomb effects.

Figure 3.5.1 illustrates the Coulomb Barrier for a given fragment and remnant; along the ordinate the probability of populating a given energy for a given temperature, and hence fixed incident energy, is also shown. Since each fragment energy "sees" a different Coulomb Barrier tunneling distance, it is necessary to integrate over energy for a fixed fragment mass to obtain the

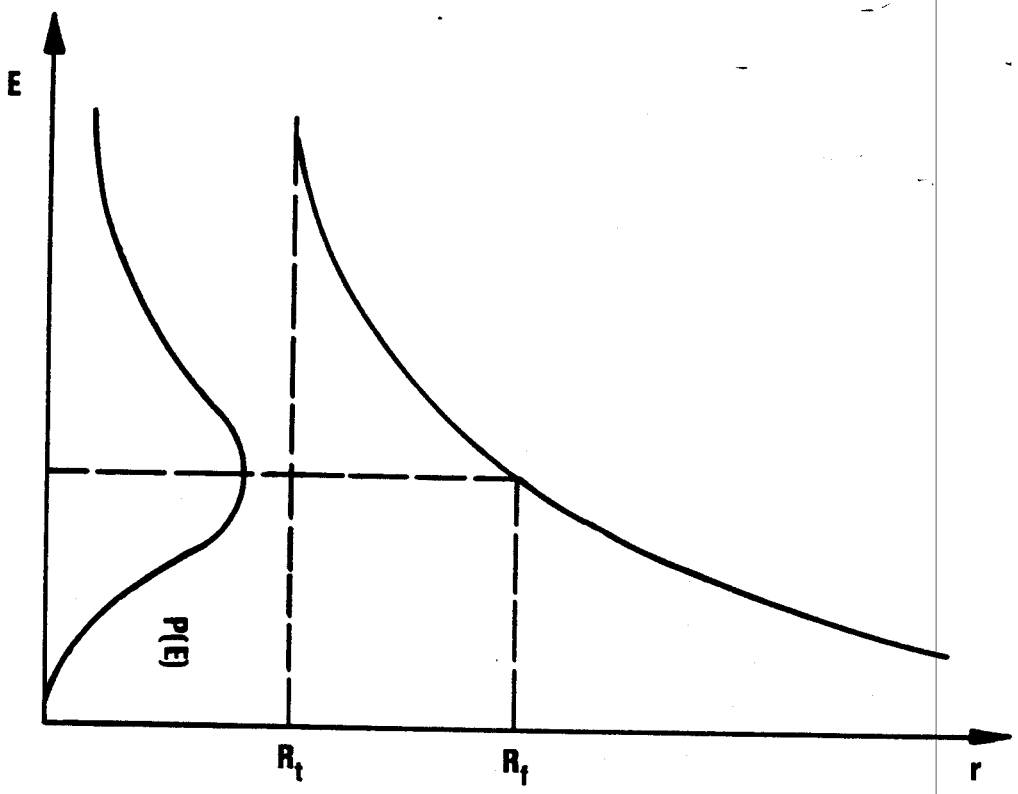

Figure 3.5.1. **The Coulomb Barrier as a function of distance r is displayed. A Maxwellian energy distribution characteristic of a given temperature is shown along the ordinate as an indication of the number of fragments that will reach the Coulomb Barrier at any given energy.**

temperature dependence of the percentage of fragments emerging from the system.

The transmission coefficient is

$$T = \exp\left\{-2\int_{R_T}^{R_F} dr \left[\frac{2mc^2}{(\hbar c)^2}(V - E)\right]^{1/2}\right\} \qquad (3.5.1)$$

where R_T and R_F are pictured in Figure 2.8.1 and are given mathematically as

$$R_T \cong 0.5 + 1.36[A_F^{1/3} + (A_S - A_F)^{1/3}] \quad (\text{fm}) \qquad (3.5.2)$$

$$R_F = \frac{Z_F(Z_S - Z_F)}{E} \cdot e^2 = \frac{V_C R_T}{E}$$

where V_C, the Coulomb Barrier energy, is

$$V_C = \frac{Z_F(Z_S - Z_F)e^2}{R_T} \quad . \qquad (3.5.3)$$

The potential energy V is assumed to have the form

$$\begin{aligned} V &= \frac{V_C R_T}{r} && r \geq R_T \\ &= 0 && r < R_T \ . \end{aligned} \qquad (3.5.4)$$

A calculation of the transmission coefficient yields

$$T = \exp\left\{-2\frac{(2M_pc^2A_FE^{1/2}}{\hbar c}\left[-R_T\left(\frac{V_C}{E}-1\right)^{1/2}+\frac{V_CR_T}{E}\cdot\right.\right.$$

$$\left.\left.\sin^{-1}\left(\left(1-\frac{E}{V_C}\right)^{1/2}\right)\right]\right\}. \tag{3.5.5}$$

For a given mass A,

$$A_F^{-\tau} = A_F^{-k}\left[\int_0^{\nu(V_c)} d\nu\, P(\nu)T + \int_{\nu(V_c)}^{\infty} d\nu\, P(\nu)\right] \tag{3.5.6}$$

where τ is the apparent exponent of the observed yield. Conservation of probability implies

$$\int_0^{\nu(V_c)} d\nu\, P(\nu) + \int_{\nu(V_c)}^{\infty} d\nu\, P(\nu) = 1 \tag{3.5.7}$$

hence

$$A_F^{-\tau} = A_F^{-k}\left[1 + \int_0^{\nu(V_c)} d\nu\, P(\nu)(T-1)\right] \tag{3.5.8}$$

assuming perfect transmission for velocities greater than $\nu(V_c)$.

Integrating over the Boltzmann distribution, one obtains

$$A_F^{-\tau} = A_F^{-k}\chi \tag{3.5.9}$$

where

$$\chi = 1 + \int_0^{\left(\frac{2V_c}{931A_F}\right)^{1/2}} d\beta \cdot 4\pi\left(\frac{A_F 931}{2\pi T}\right)^{3/2} \cdot \beta^2 \exp\left[\frac{-A_F \cdot 931 \cdot \beta^2}{2T}\right]$$

$$\cdot \left\{ \exp\left[-2\,\frac{931 A_F \beta}{197} \cdot \left[R_T \left(\frac{2V_c}{A_F \cdot 931 \cdot \beta^2} - 1 \right)^{1/2} + \frac{2V_c R_T}{A_F 931 \beta^2} \right.\right.\right.$$

$$\left.\left.\left. \cdot \sin^{-1}\left(\left(1 - \frac{A_F 931 \beta^2}{2V_c} \right)^{1/2} \right) \right] \right] - 1 \right\}. \qquad (3.5.10)$$

A calculation of this quantity for different masses allows a fit of the resultant yields to a power law dependence, and leads to the behavior illustrated in Figure 3.5.2. Obviously the Coulomb effects always lead to decreasing value of τ with increasing energy, in contrast to the experimental data which suggests a decrease followed by an increase.

3.5.3 In-Medium Corrections, Evaporation and Final State Interactions

It is appropriate and instructive to discuss the background effects that will tend to obscure the idealized signatures of the reaction mechanisms described in the preceding sections of this chapter.

In-medium corrections occur prior to freeze out and can alter physical observables such as gamma or particle emission. If the ambient energy is sufficiently low, composites may form and come into thermodynamical equilibrium with the surrounding nucleon gas.

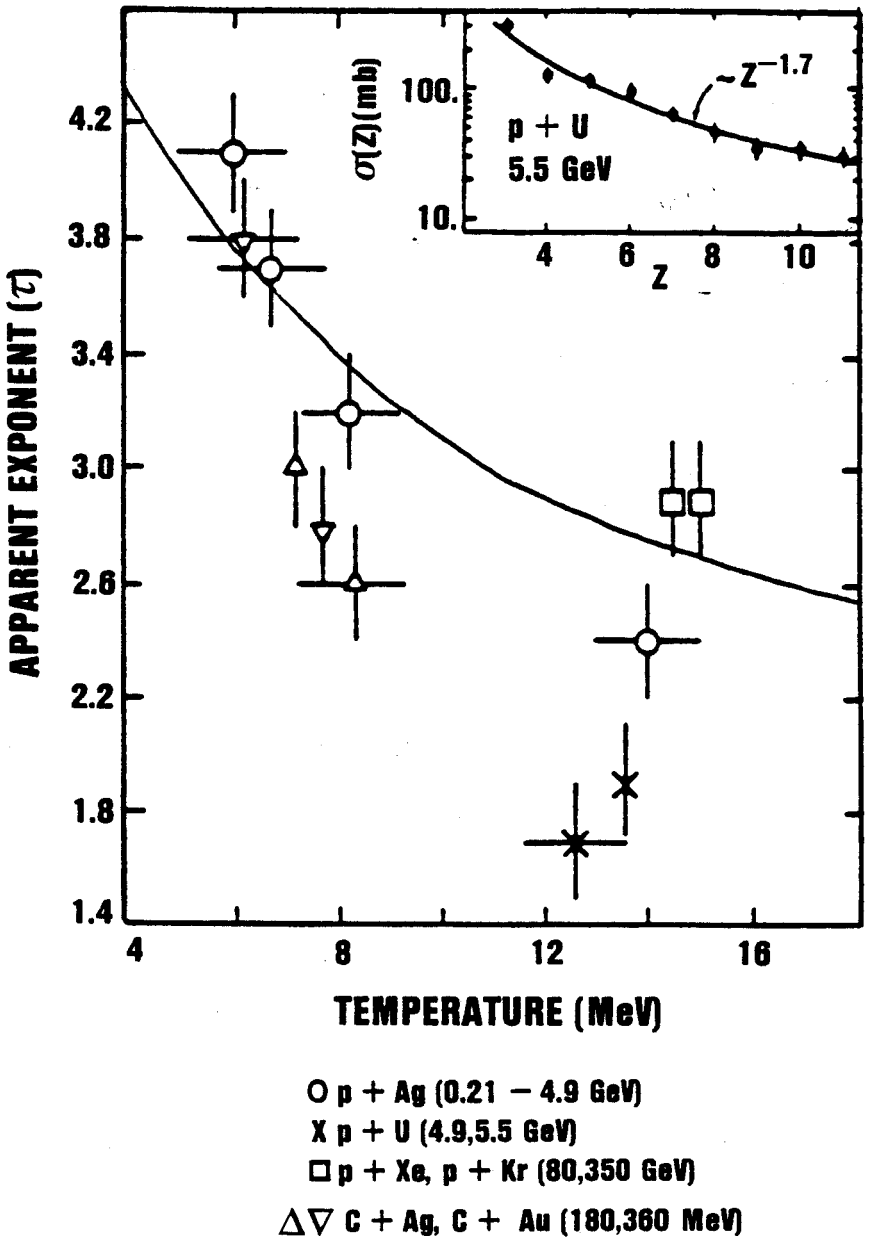

Figure 3.5.2. The apparent exponent as a function of temperature for a system characterized by a fixed A^{-k} (k = constant) initial distribution which is subsequently subjected to the Coulomb tunneling effects described in the text (solid line). The Coulomb tunneling prediction is compared to the data given in Table 1.

It is important to note that the internal temperature of the composite is equal to the ambient nucleon gas temperature and therefore the density is not that of a nucleus residing in the vacuum (where $\rho = \rho_0 \cong 0.17\ fm^{-3}$). Figure 3.5.3 illustrates the two different situations, while Figure 3.5.4 denotes the density and temperature associated with the liquid and gaseous components of a coexistence mixture. An important point is that the composites illustrated ($\overline{Li}^*$, $\overline{Li}^{g.s.}$) in Figure 3.5.3 are at a different density and temperature than their vacuum counterparts. In fact, if the vacuum counterparts were placed in the nucleon gas they would be thermodynamically unstable; they exist even out of the range of metastability for most temperatures if not for all temperatures.

Examination of Figure 3.5.5 illustrates how the potential well, and hence the excited state levels, will change as the system expands until it traverses the freeze out density whereupon Figure 3.5.5c becomes applicable. Since emission can occur anywhere along the evolution, the distribution of gamma radiation can possess a sampling from each stage. Figure 3.5.6 shows a possible dynamical path of the participant region which would generate the conditions depicted in the preceding figure.

In-medium corrections are inherent to an equilibrium liquid-gas coexistence and cannot be neglected, especially when attempting to describe droplet structure characteristics such as γ emission. It will ultimately be necessary to perform a self-consistent Brueckner-Hartree-Fock calculation to ascertain the perturbations

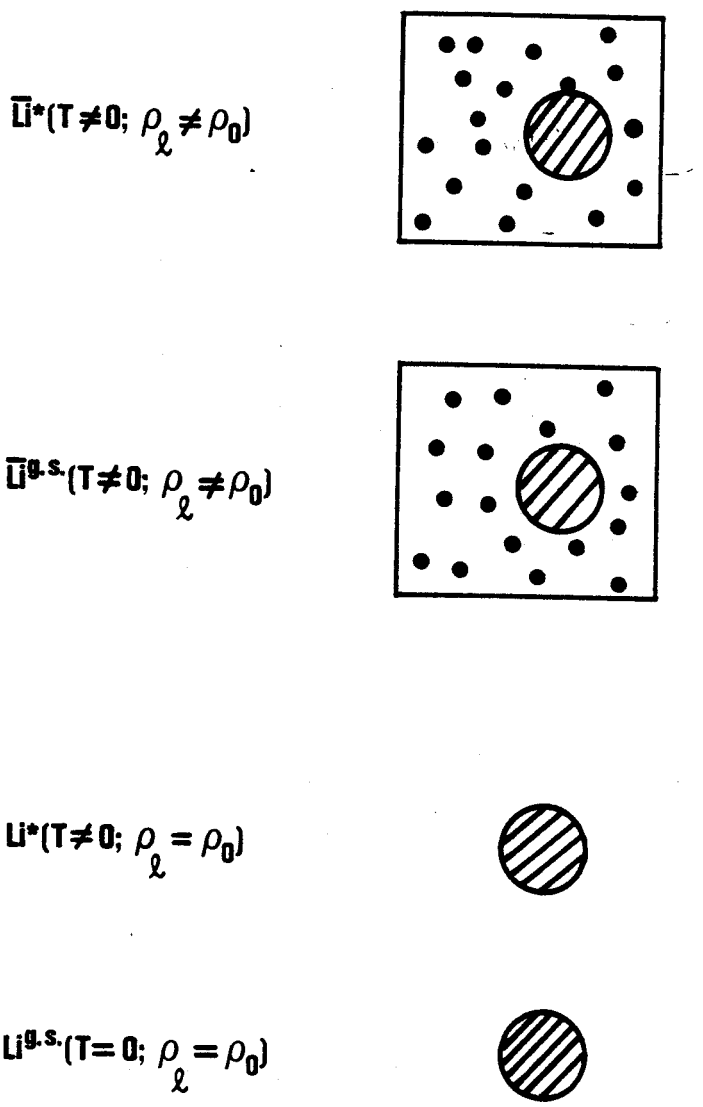

Figure 3.5.3. a) The $\bar{Li}^*$ and $\bar{Li}^{g.s.}$ states are depicted in-medium. Note that the liquid density is not the normal nuclear density. b) The Li^*, $Li^{g.s.}$ pair of in vacuo states are also represented. Note that here the density is that of normal nuclear matter.

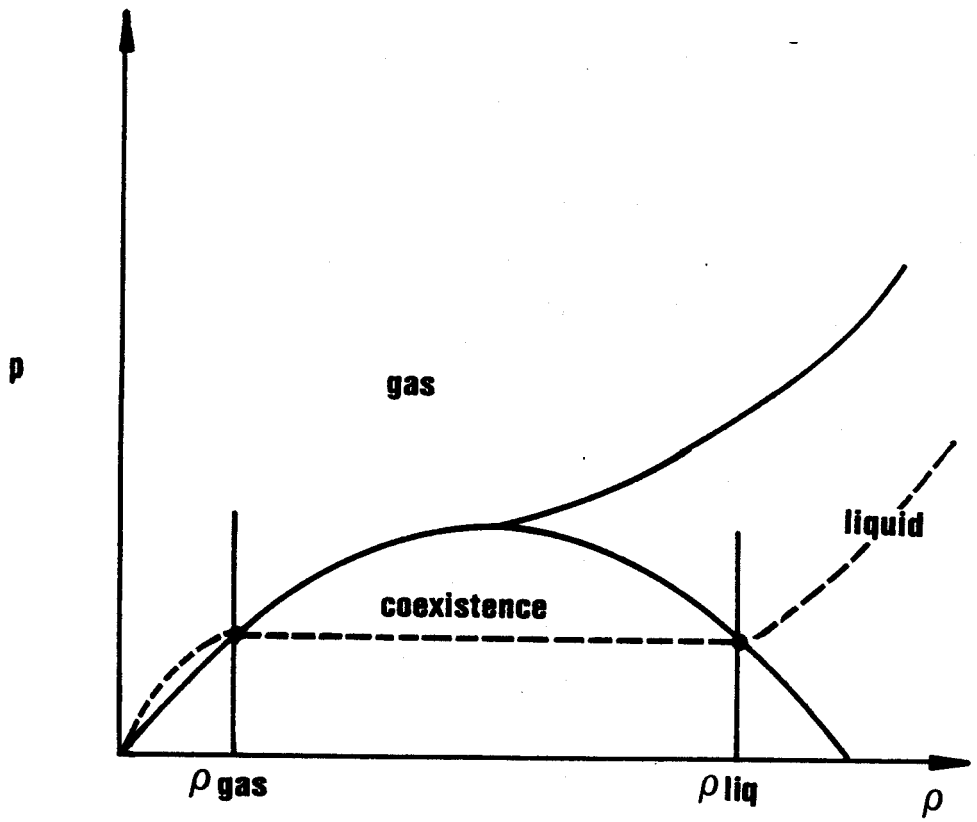

Figure 3.5.4. **The pressure vs. density diagram for a liquid-gas coexistence region indicating the expected density range for the fragment clusters produced in a coexistence mixture.**

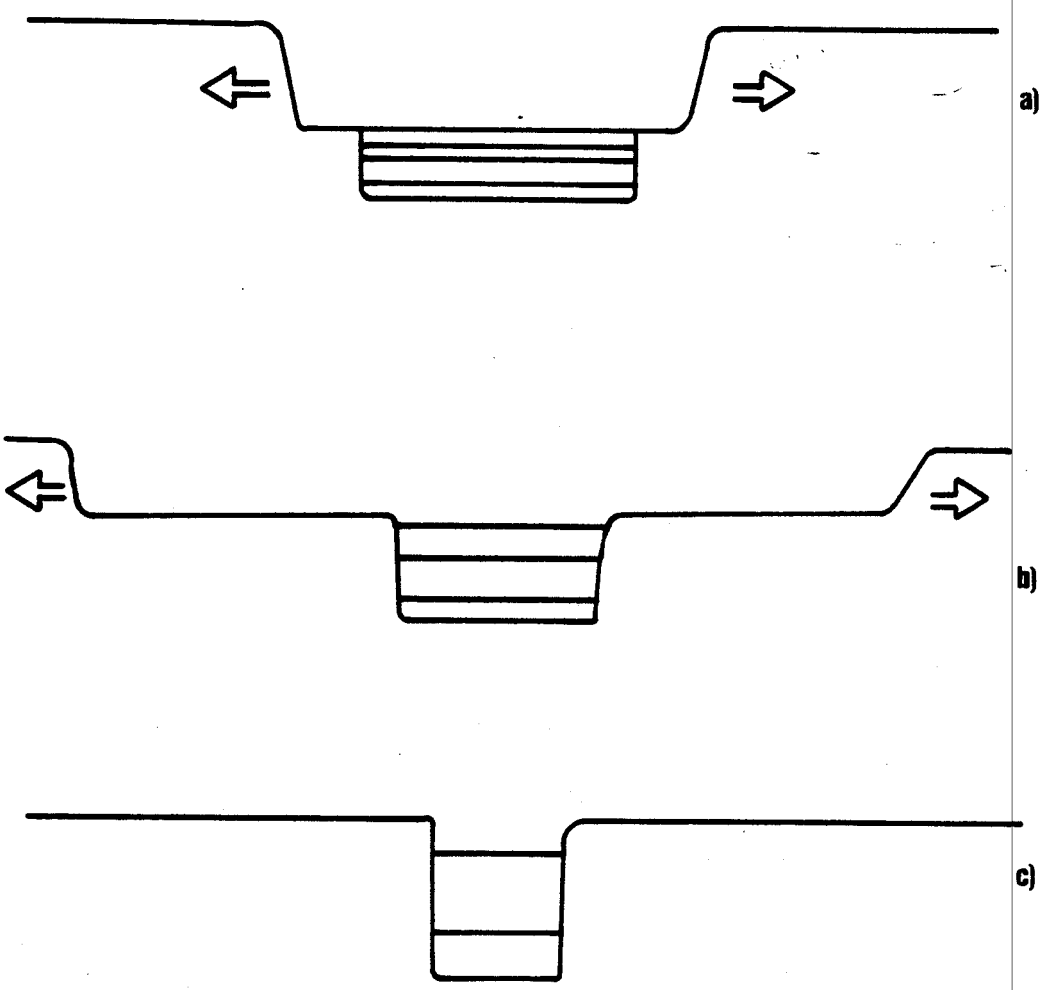

Figure 3.5.5. **The distorted energy levels of a droplet whose density is not normal are illustrated in a potential well diagram. The expanding system will traverse the conditions depicted in a), b), and finally c). Since emission can occur anywhere along the evolution, the distribution of gamma radiation can possess a sampling from each stage.**

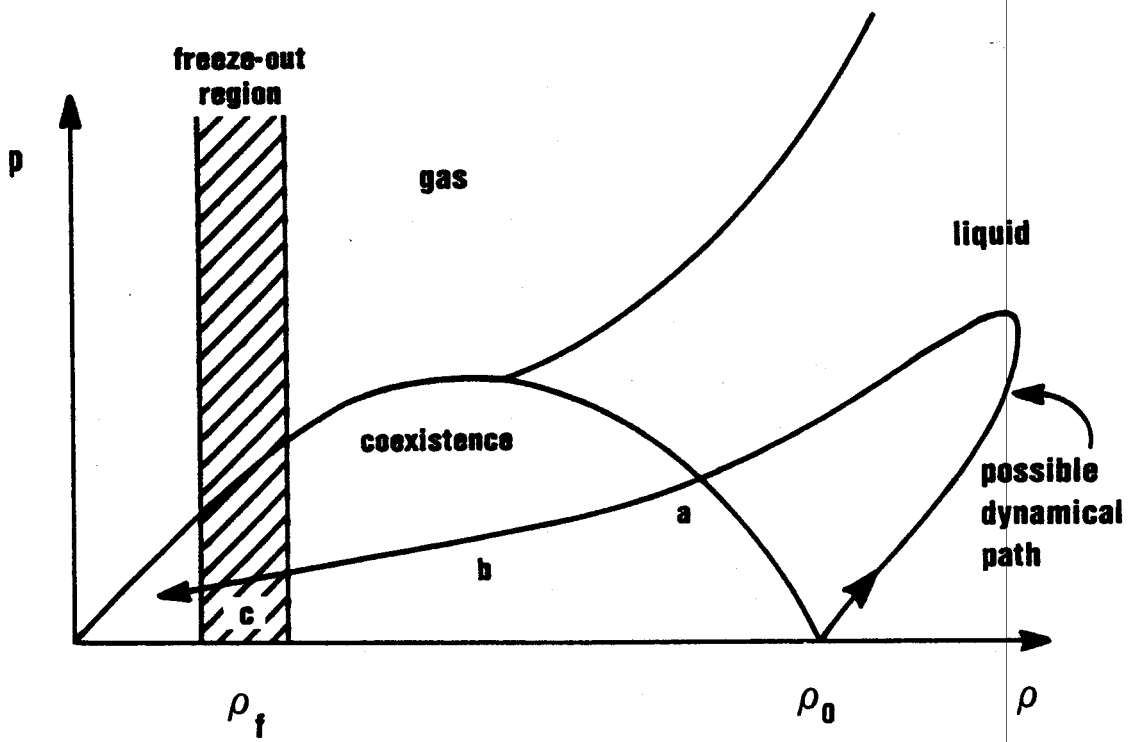

Figure 3.5.6. **A possible dynamical path of a hot, dense nuclear system produced in a heavy ion induced collision. Points a, b, and c correspond to conditions depicted in Figure 3.5.5.**

induced due to ρ and T and then subsequent calculations describing the dynamical aspects so that the values of ρ, T for the ambient environment can be ascertained. An experiment was recently performed which attempted to measure the temperature of the interaction region by measuring the relative population of two low lying nuclear states (see MOR 84 and the further brief description given in Chapter 6). Utilizing the Boltzmann factor

$$P(E_1; E_2) = e^{-(E_2-E_1)/T} \tag{3.5.11}$$

the temperature can be deduced once the relative populations of the two energy levels are known. This experiment deduced the relative populations by observing a γ emission characteristic of the energy separation of two levels of a nucleus, the energy levels of which had been determined from earlier experiments. Temperatures deduced in this manner were much lower than temperatures determined from moving source fits to the double differential cross sections. However, as explained in the preceding paragraphs, the separation of the energy levels of this "nucleus" may change due to in-medium corrections. This calls into question the validity of using the characteristic γ-emission to determine the relative populations of the two states. Hence, although this method of measuring temperature superficially appears more reliable than the conventional method of utilizing the slope of the energy spectra, in practice the derived temperatures must be viewed with caution. Indeed, recent studies by Pochodzalla et al. (POC 85) have extended the approach to

the measurement of the relative populations of states in ^{5}Li and ^{8}Be through subsequent particle decay. They find that the deduced temperatures depend on the type of decay particle. As a final caution we note that it is also necessary to describe composite-composite interactions if the number of composites produced is not negligible compared to proton and neutron production.

Another complication may develop if, as one intuitively believes, the freeze out is dependent on the mean free path. Since different composite systems have different mean free paths, due in part to different geometrical sizes, the freeze out density may therefore be fragment dependent. It is also related to the number of nucleons present since the composites must freeze out from the surrounding system of nucleons with which they are in equilibrium. Thermal models utilize a freeze-out concept to describe the point at which the constituents of the system no longer interact with one another and beyond which they travel undisturbed to the detectors. Thus all the interactions that transpire after ρ_f tend to obscure the physics at ρ_f.

As described in the discussion of chemical equilibrium time scales (Section 2.4), the higher the internal energy, the higher the temperature, and the greater the deviation of a given fragment cross-section from the primary distribution. This implies that sequential evaporation following a mechanical or chemical instability will exhibit greater deviations from the primary distribution than the target-like fragments produced in the Cold Shattering Model.

For intermediate mass fragments, the most likely evaporation will be a proton or an alpha particle, leaving a large residue. If the primary fragment evaporates only a few times, then the primary distribution will generally shift to lighter masses by 1-4 nucleons while the light ions ($1 \leq A \leq 4$) will possess the primary distributions combined with contributions from the entire intermediate mass regime (see Figure 3.5.7). For this reason it is more advantageous to study intermediate mass fragments when attempting to observe a liquid-gas phase transition. Signatures of a mechanical instability are likely to be more apparent in light fragment production and are consequently the most difficult to observe. Even very light systems can break up, for example $^3He \rightarrow t + p$ and $t \rightarrow d + p$, thus obscuring even further the primary distribution of light particles. This effect, together with sequential freeze out densities, will tend to obscure correlations between different fragments.

Coalescence can also obscure the physics since single nucleons can form composites if they possess small relative momenta (see Section 3.2.2). This process is totally dominated by statistical emission patterns at ρ_f and hence should be present as a background. In fact, the coalescence model should always be the limiting behavior of both the single phase and liquid-gas thermal models as the incident energy increases to high values.

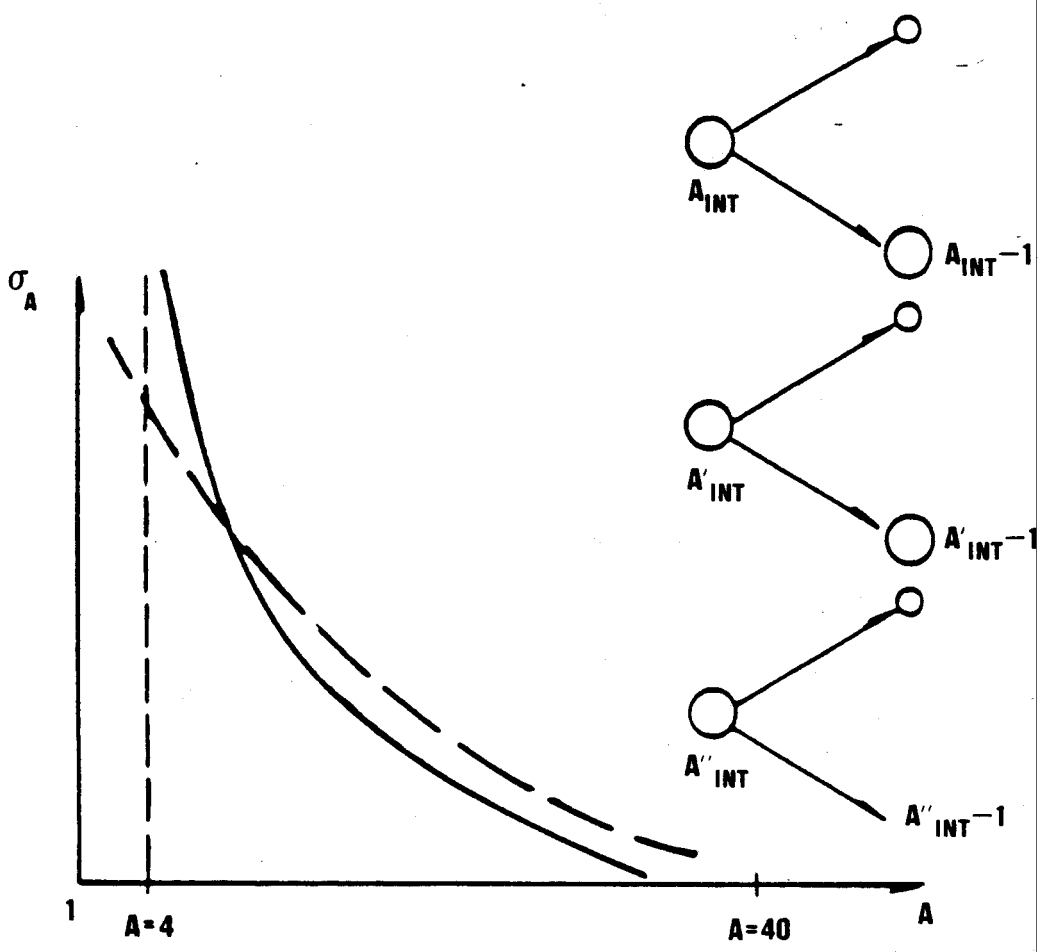

Figure 3.5.7. **The anticipated primary and secondary fragment distributions as a function of mass are displayed by dashed and solid lines, respectively. It is anticipated that the sequential decays will resemble thermal, asymmetric fission hence producing copious light fragments and only slightly reducing the anticipated heavy fragment yields.**

CHAPTER 4

EXPERIMENTS AND DATA ANALYSIS

4.1 Introduction

Initially the experimental program was designed to study the behavior of light fragments produced in collisions of heavy ions in the intermediate energy range. A large body of data was studied over a wide range of incident energies (CUR 83a and references therein; WES 82; WES 83). Upon examination of these light fragment data, which appeared to possess a spatially localized signature, we noticed that the lower incident energy data exhibited some interesting and possibly profound behavior (see Figure 3.2.2). The yield of alpha particles relative to proton yields increased as the incident energy decreased, in contradiction to the coalescence mechanism which explained composite particle production at higher incident energies (CUR 83a). These light fragment experiments led to the speculation that a liquid-gas phase transition might occur in heavy ion collisions. However, binding energy effects obscured any clean interpretation, and hence it was decided that the production of heavier fragments might be less ambiguous (CUR 82a).

The philosophy of the heavy fragment experimental program consisted of measuring the inclusive yield of complex fragments as a function of incident energy for a given projectile-target

combination. The Purdue-Fermi Lab and other groups had provided data from proton induced reactions over a large range of energies, which were interpreted as evidence for a liquid-gas phase transition (FIN 82; MIN 82). However, as we noted earlier, the proton may not provide enough compression or energy deposition to create conditions necessary for differentiating between different models.

We studied reactions with a relatively light projectile on a medium heavy target nucleus (^{14}N + ^{nat}Ag) at energies of 20A, 30A, and 35A MeV using the Superconducting Cyclotron at MSU. The experiments were designed to measure inclusive yields of heavy fragments of charge $6 \leq Z \leq 24$.

Since a significant difference between the Cold Shattering, Coulomb Tunneling, the Mechanical Instability, and Liquid-Gas Models is that the first two deal primarily with charge distributions, and the second two deal primarily with mass distributions (see Chapter 2 and Chapter 3), it behooves us to attempt isotopic separation as well as charge identification. Furthermore, since the main objective was to ascertain total yields it is also desirable to measure energy spectra down to the Coulomb Barrier energy. The range of incident and emitted particles and energies required a variety of separate detector arrangements comprising telescopes of ion chambers (IC), solid state detectors (SSD), as well as a time of flight apparatus (TOF). The experiment was therefore designed to measure both a wide range of energies of emitted fragments and a large range of charge ($6 \leq Z \leq 24$).

4.2 NSCL Experiment (^{14}N + ^{NAT}Ag; 20A, 30A, 35A MeV)

4.2.1 Facilities

The experiment was performed with the superconducting K500 cyclotron at the National Superconducting Cyclotron Laboratory (NSCL) on the Michigan State University campus. The K500 (Phase I) cyclotron consists of a three sector superconducting cyclotron with a conventional PIG ion source. Eventually the K500 will inject beams into a much larger K800 (Phase II) cyclotron which should be capable of accelerating nuclei as heavy as Uranium over the entire intermediate energy regime. At present, however, the K500 is a "stand alone" cyclotron.

The experiment was performed in the scattering chamber on the S320 Spectrograph beam line. Figure 4.2.1 illustrates the floor plan for the experimental area.

4.2.2 Detectors

Four separate detector systems were used consisting of: two TOF systems, a three element SSD telescope, and one IC-SSD telescope. These systems are briefly described in turn.

Firstly, two TOF detector systems were positioned in the wedge, with a general design similar to the system described by Spieler (SPI 82). The order in which detectors are discussed reflects the detected particle trajectory. The start detectors were Argonne designed microchannel plate (MCP) assemblies (CUR 82c). The first ΔE detector was a gas filled ion chamber of $\cong$ 10 cm gas path length (see Table 5 for exact values and relevant quantities). The

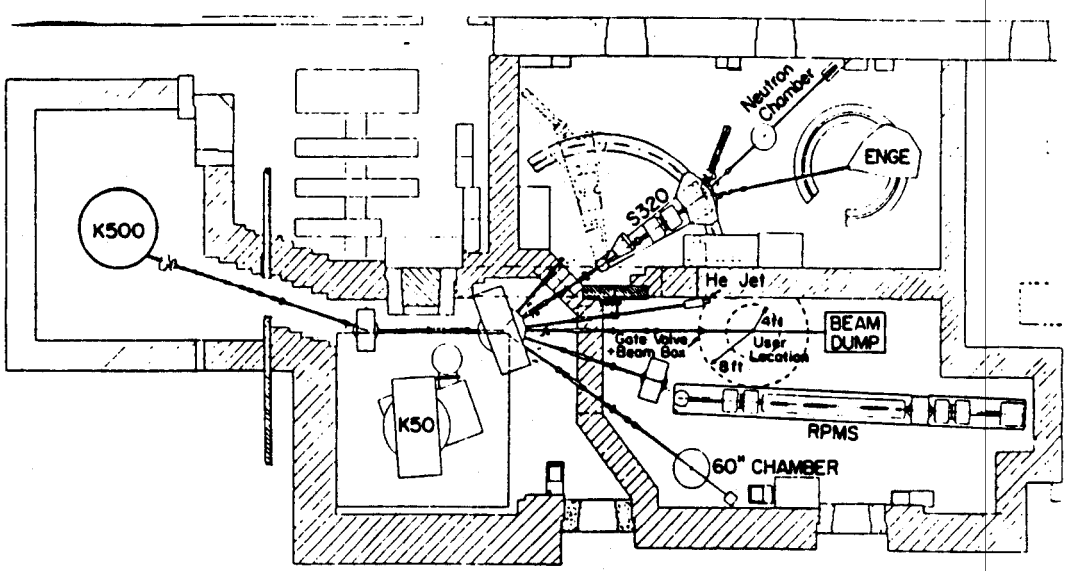

Figure 4.2.1. Layout of the NSCL experimental facilities. The heavy fragment experiment was performed on the S320 line.

Table 5. Relevant dimensions and associated flight times for TOF systems in the ^{14}N + ^{nat}Ag experiment.

System	$(E/A)_{BEAM}$ (MeV/u)	d_{START} (cm)	d_{TOF} (cm)	d_{GAS} (cm)	$t_{TOF}[(E/A)_{BEAM}]$ (nsec)	Beam Velocity $t_{TOF}[1\ MeV/u]$ (nsec)
TOF 1	20	42.6	88.2	9.47	14.5	63.7
	30				11.9	
	35				11.0	
TOF 2	20	30.5	90.1	9.78	14.8	65.1
	30				12.2	
	35				11.3	

two ion chamber gas lines were connected in series and used P10 gas, which has a composition of 90% Argon-10% methane (CH_4), at 70 Torr. The ion chamber in TOF1, placed at more forward angles, was a Grenoble designed ion chamber while TOF2 utilized a Heidelberg designed ion chamber. The stop detectors were 400μ surface barrier detectors. A comment is in order regarding the interplay between the TOF measurement and ΔE-E measurement. Since the low energy component comprises the bulk of the cross section for the intermediate mass fragments, it was deemed important to measure fragments down to the Coulomb Barrier energy, and this requirement led to the choice of ion chambers. The energy loss was designed to be extremely small ($\cong$ 0.5-10 MeV) in the ion chamber, and thus the flight time was not appreciably altered by coupling the TOF measurement with the energy measurement. If the SSD stop detectors had been placed in front of the ion chamber then it would not have been possible to measure down to the Coulomb Barrier. The E detectors were 5 mm Lithium drift detectors. The solid angle subtended by each TOF detector system was defined by the aperture of the ion chamber window support to be .15 msr. The Grenoble ion chamber window was a 50 $\mu g/cm^2$ mesh supported polypropelene window, while the Heidelberg ion chamber window consisted of an unsupported 200-250 $\mu g/cm^2$ aluminized mylar window.

Secondly, a three element solid state detector arrangement was also used to obtain mass identification for light masses ($A \leq 15$)

while preserving high efficiency and subtending a comparatively large solid angle (6.5 msr).

Thirdly, a two element Lawrence Berkeley Laboratory (LBL) ion chamber (for a review see Barrette et al. (BAR 75)) was used to measure intermediate mass fragments ($6 \leq Z \leq 24$). Although it was indeed possible to measure low energy heavy mass fragments, only Z resolution was obtainable. Two advantages of this detector system were its relatively large solid angle (5.8 msr) and yet small physical size permitting operation within the scattering chamber. The path length of gas traversed by a fragment was $\cong$ 6.8 cm. Again, P10 was used at pressures of 70 and 90 Torr, corresponding to more backward and more forward angles respectively. The E detector was a partially depleted 1 mm surface barrier detector. The window was a mesh supported polypropelene window ($\cong$ 100 $\mu g/cm^2$).

4.2.3 Physical Arrangement

The physical relationship of the detectors, chamber, wedge, and target are illustrated in Figure 4.2.2. The TOF detectors required 1 meter flight paths; therefore they were situated in the wedge. The large angular range of the wedge assembly permitted the larger angle TOF measurements. The smaller detectors were placed closer to the target inside the scattering chamber, which allowed them to be moved independently of the spectrograph assembly. The close-in geometry detectors (three element SSD and two element LBL IC) are situated in the target chamber and are positioned on a cylindrical collar which is attached to the target ladder assembly.

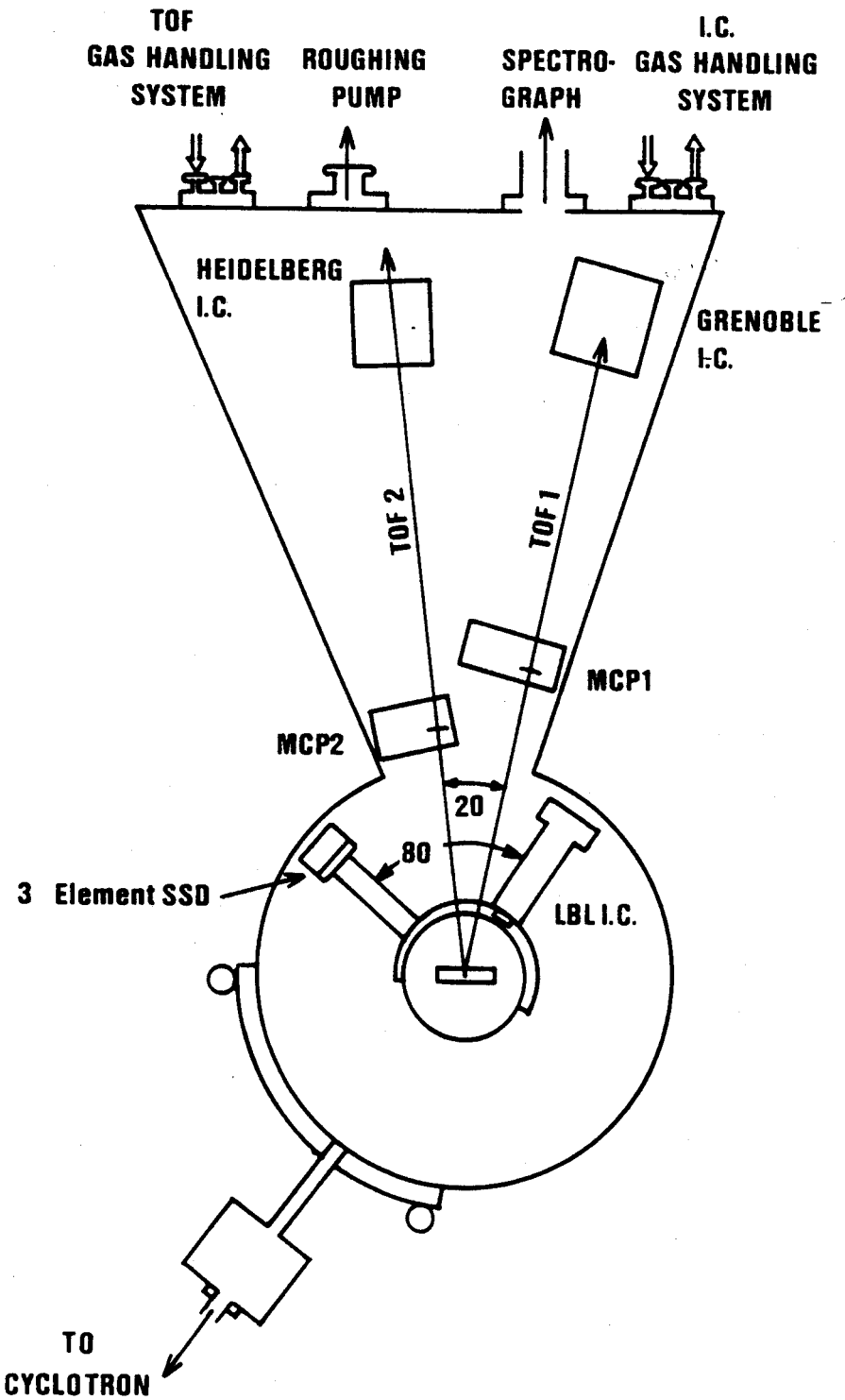

Figure 4.2.2. **Physical arrangement of the detector systems for the heavy fragment NSCL experiment. The experiment was performed using the S320 line and the associated target chamber and wedge assembly.**

Two radial arms project from the cylindrical collar on which the two detectors are mounted. The TOF assemblies are mounted in the wedge and rotate with the spectrograph, independently of the target movements. The wedge contains a removeable plate with radial grooves in which we mounted trays for both the MCPs and the ICs which allowed radial alignment with a transit. The quadrupole magnets did not permit use of the transit in the alignment of TOF1 directly; instead it was necessary to position a laser with an appropriate x-z mount and a position indicator which reflected the laser light so that it could be ultimately cross referenced to the transit. After careful alignment, the horizontal position of the target-MCP-IC was accurate to ± 1 mm while the vertical position was accurate to within ≅ 1.5 mm.

Roughing vacuum was achieved by a mechanical roughing pump and normal operating vacuum was maintained by a cryo-pump which was positioned on the wedge. The vacuum required by the MCP is ≅ $1 \cdot 10^{-6}$ Torr, and preferably $5 \cdot 10^{-7}$ Torr. Since our detectors employed gas filled ICs, vacuum monitoring of the target chamber was essential. The sliding seal provided good vacuum when stationary. However, during spectrograph rotations it was neccessary to lower the voltages on the MCPs. To preserve our targets, carbon foils, and IC windows we found it necessary to regulate venting and pump down rates very carefully. Two MSU built gas handling systems were used to maintain an even flow rate and correct pressure within the TOF ICs and the two element IC.

4.2.4 Experimental Procedure

Three incident energies, 20A, 30A, and 35A MeV, of ^{14}N were run utilizing a 1.0 mg/cm^2 ^{nat}Ag target. The thickness and uniformity were checked using an α source and an SSD to measure the shift in energy centroids due to passage through the target. The computer program DONNA was used to determine the thickness which agreed with the nominal thickness to within 10%; uniformity was better than 4% over the target face. The two element ion chamber and three element SSD telescopes covered angles $\cong$ 20°-60° at 10° intervals while TOF measurements were made at angles $\cong$ 20°-50°, also at 10° intervals. Pressures in the TOF ion chambers were fixed at 70 Torr of P10 (90% Argon and 10% Methane) while the close-in geometry ion chamber was run at 90 Torr for 20° and 30° and 70 Torr for 40°, 50°, and 60° since less energetic particles are emitted at these backward angles.

The TOF time resolution was determined to be $\cong$ 400 ps from elastic scattering of 20A MeV ^{14}N on ^{197}Au. The on-line efficiencies were determined to be $\cong$ 7% averaged over all fragments, with energy dependence of the efficiency measured in one of the TOF telescopes for charges $4 \leq Z \leq 10$ as shown in Figure 4.2.3. This was obtained by comparison of the start-stop coincidence scaler and the stop scaler, assuming the stop detector (SSD) was 100% efficient. The behavior of the efficiencies mirrors the dependence of energy loss on energy and fragment charge, i.e. the energy loss increases with increasing fragment charge and decreases with increasing

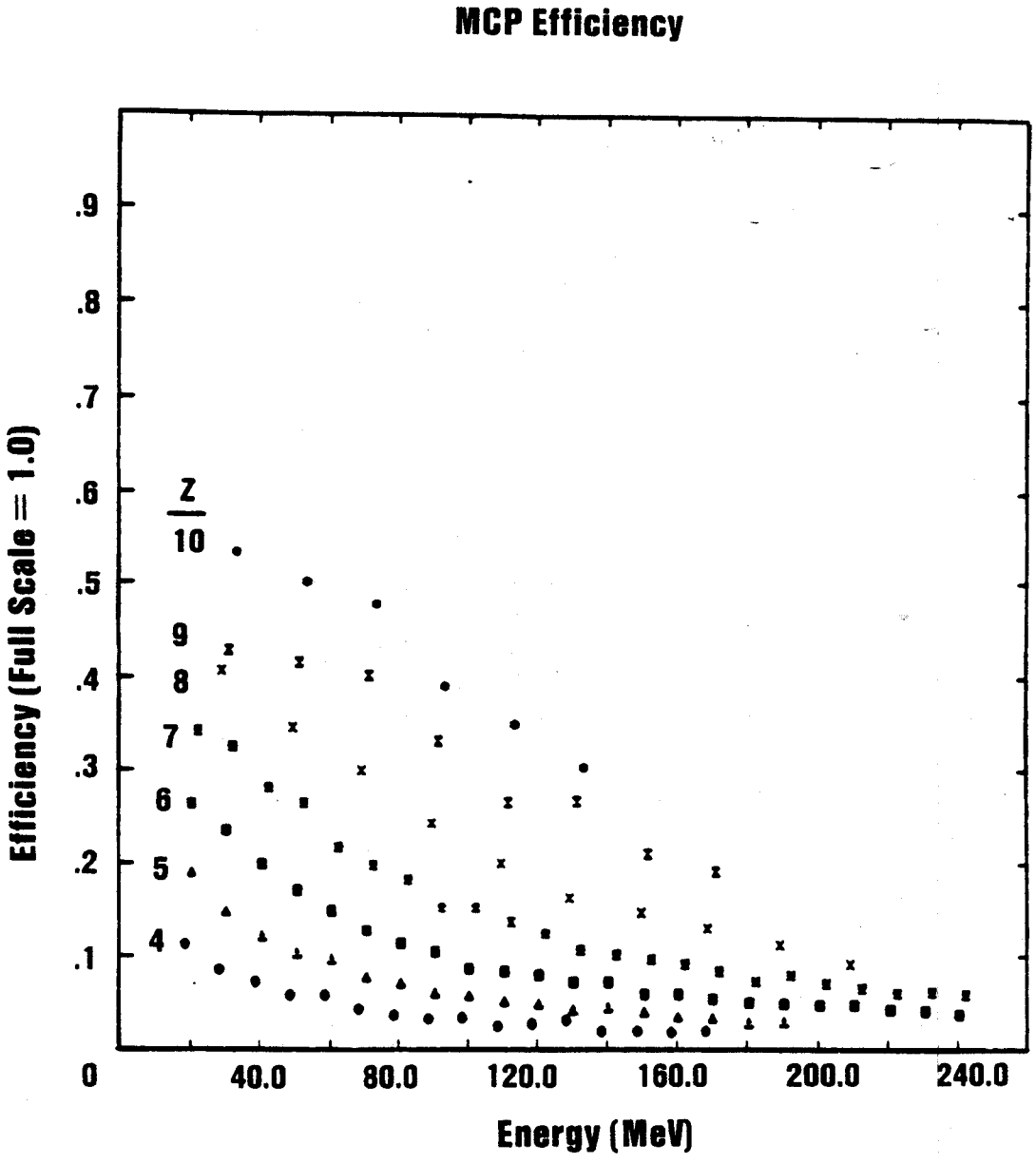

Figure 4.2.3. **The Micro Channel Plate (MCP) efficiency is illustrated as a function of fragment energy for $4 \leq Z \leq 10$.**

incident energy for a given charge. We conclude that the efficiencies reflect the amount of energy lost in the carbon foil by the fragment. If less energy is deposited then fewer secondary electrons are ejected, hence producing a weaker signal.

A typical spot size was roughly 3mm x 5mm on target. Typical beam intensities available during our run were:

20A MeV ^{14}N : 150 enA

30A MeV ^{14}N : 50-150 enA

35A MeV ^{14}N : 10-15 enA .

Blank target frames were inserted to estimate the contribution from the background and stray beam particles or "halo" striking the supporting frame. Since the beam was well collimated, these effects were found to be negligible. Measurements were also taken with a carbon target since carbon deposits were noticed on the target as the experiment progressed.

4.2.5 Data Reduction

Immediately after the experiment a pulser-chopper and Time to Amplitude Converter (TAC) calibrator were used to determine energy and time calibrations, respectively. The solid state detector was calibrated using a calibrated capacitor-chopper unit driven by a tail pulse generator. In the case of the ion chamber the calibration was determined by constructing several narrow energy gates on the energy spectra of the solid state detector immediately behind the ion chamber and projecting the resultant ion chamber spectra.

The peaks corresponding to different charges were compared to a range energy calculation (DONNA) to determine an energy calibration.

Analysis of the spectra was carried out with the program SMAUG (a data analysis tool developed at NSCL). One particularly useful feature of this program is its capability for setting a gate on a two dimensional spectrum and projecting onto either axis. The two element ion chamber analysis consisted of setting gates on the individual charge spectrum of a ΔE_{IC}-E ($= \Delta E_{IC} + \Delta E_{SSD}$) plot and projecting the energy spectrum onto the E axis. An example of a two dimensional ΔE_{IC}-E plot is displayed in Figure 4.2.4.

The direct result of gating and projection onto the E axis is shown in Figure 4.2.5 for energy bins of 1 MeV for the case of carbon isotopes at $\theta_{LAB} = 60°$. Differential cross sections as a function of energy exhibit a steady exponential increase for decreasing energy until a maximum is reached at an energy attributed to the Coulomb barrier, beyond which the cross section falls off. However, as the energy is decreased beyond approximately 25 MeV the cross section appears to increase once again. This increase occurs for all fragments measured. The reason for this behavior becomes evident from an examination of the $\Delta E1 - \Delta E2$ color display (not shown). A bright band corresponding to high statistics extends over the entire $\Delta E1$ energy range where fragments were detected. However, the $\Delta E2$ energy range is confined to the narrow range corresponding to particles. Therefore, we ascribe this bright band, not to an actual increase in the cross section, but rather to an accidental

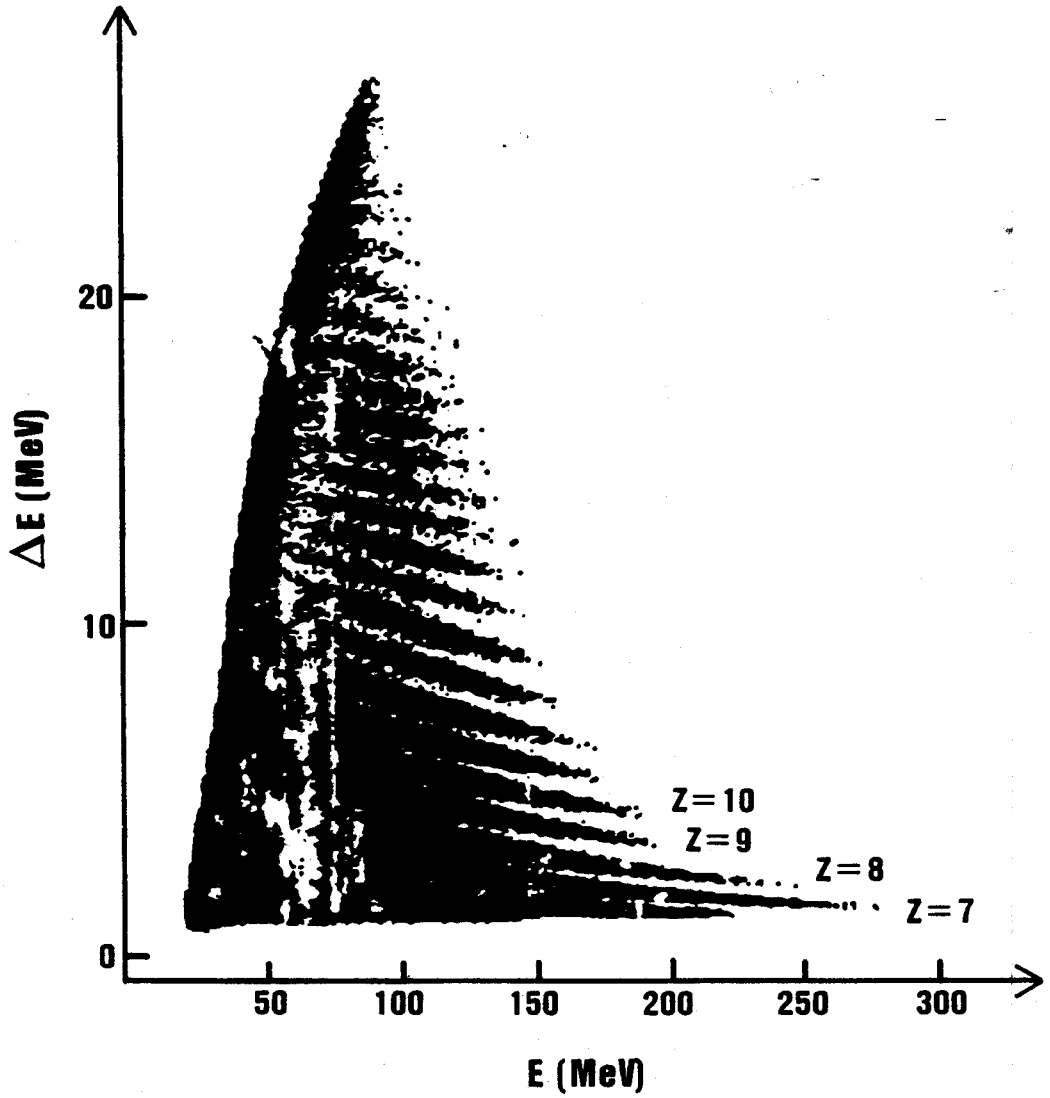

Figure 4.2.4. **A typical ΔE-E plot from the IC-SSD telescope. The lines correspond to differently charged fragments.**

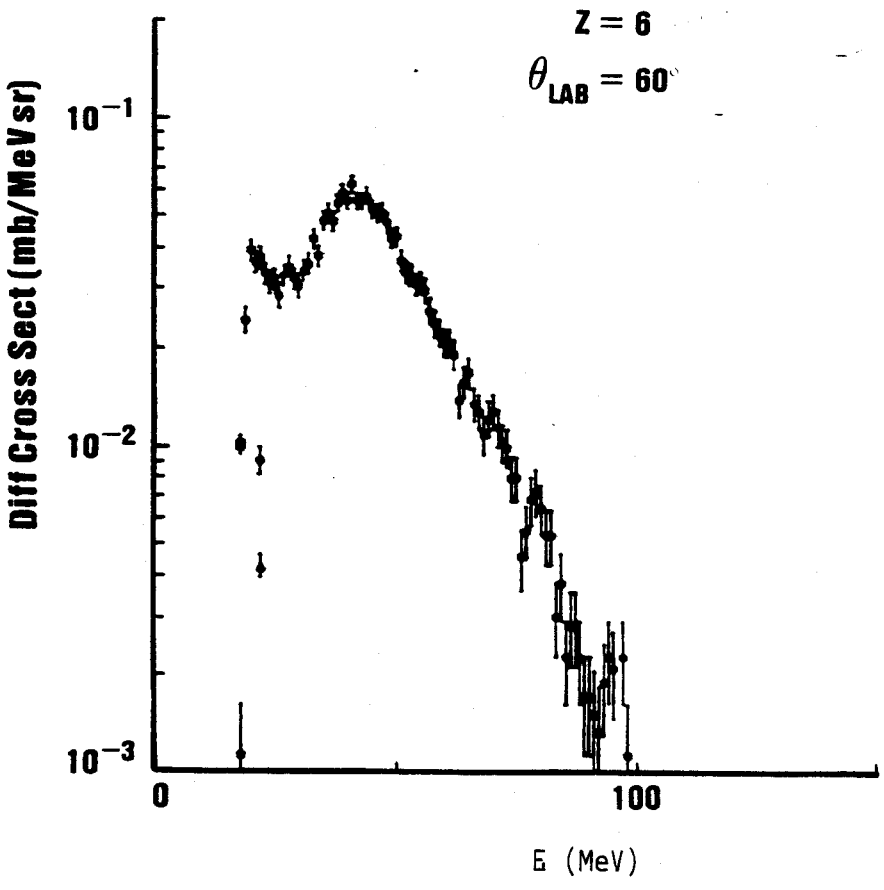

Figure 4.2.5. **Projection of carbon isotopes onto the E − axis for θ_{LAB}=60° . It is important to note the increase at low energy (E ≤ 25 MeV) in the differential cross section. This unphysical behavior is due to accidental coincidences between α particles and heavier fragments which are only detected in the gas.**

coincidence of a heavy fragment detected in the gas ($\Delta E1$) (but not the SSD ($\Delta E2$)) and an α particle detected in both elements ($\Delta E1$ and $\Delta E2$). For this reason, the low energy portions of the spectra are truncated, but the determination of the cross section is not significantly influenced since this region is well below the Coulomb Barrier energy. The Coulomb Barrier in the lab frame is lowest for the lightest element ($Z = 6$) measured at the most backward angle ($\theta_{LAB} = 60°$), due to the decreasing effects of kinematical energy shifts in the laboratory frame.

The analysis of the three element solid state detector was more complicated, since a valid event was defined in this case from the second element, thus introducing a pedestal into the spectra of the third detector when a particle stopped in the second detector. To circumvent this problem, gated $\Delta E1 - \Delta E_{TOT}$ ($= \Delta E1 + \Delta E2$) spectra were created with a gate set around the pedestal in the $\Delta E2 - \Delta E3$ two dimensional spectra. The particles which punched through the second detector, leaving a discernible signal in the third detector, are identified by creating a complementary gate excluding both the pedestal and α particles, which gave rise to accidental coincidences of high energy particles with low energy heavy ions stopping in the first detector. The filtered data were subsequently used to generate a $\Delta E1 - E_{TOT}$ ($= \Delta E1 + \Delta E2 + \Delta E3$) gated spectrum. All isotopic spectra are created by projecting onto the total energy axis. The low and high energy spectra are then combined to produce the total energy spectra. A sample gated two dimensional spectrum of

the three element solid state detector telescope is shown in Figure 4.2.6.

The time of flight energy calibration was performed in the same manner as for the two element ion chamber calibration. As can be seen in Figure 4.2.7, mass separation was achieved for masses with $A \leq 18$ by means of the $t\text{-}E_{TOT}$ plot. The technique for separating isotopes was to create a $t\text{-}E_{TOT}$ two dimensional plot gated on individual charges determined from the $\Delta E_{IC}\text{-}E_{TOT}$ plot. The individual mass lines are then identified to complete the isotope identification, and used to project the associated spectrum onto the E_{TOT} axis. However, the low statistics prohibited useful spectra from being obtained. The beryllium isotopes were used to calibrate the mass identification, since the instability of the ^{8}Be isotope leads to a "hole" in the gated $t - E_{TOT}$ spectra. Incidentally, this missing mass also serves to identify the charge, $Z = 4$, in the $\Delta E_{IC} - E_{TOT}$ plots.

To assess the contamination due to carbon build-up on the target, spectra at two angles were measured at 35A MeV (30° and 50°) and five angles were measured at 30A MeV (20°, 30°, 40°, 50°, and 60°). The 30A MeV Ag run was the last run of the experiment. Since carbon accumulates on the target as a function of the integrated beam current, the carbon deposit should be greatest at the conclusion of the experiment (30A MeV run). The observed $^{14}N + {}^{12}C$ cross sections increase well below the Coulomb Barrier energies of the Ag target fragments; therefore it is possible to obtain an upper limit

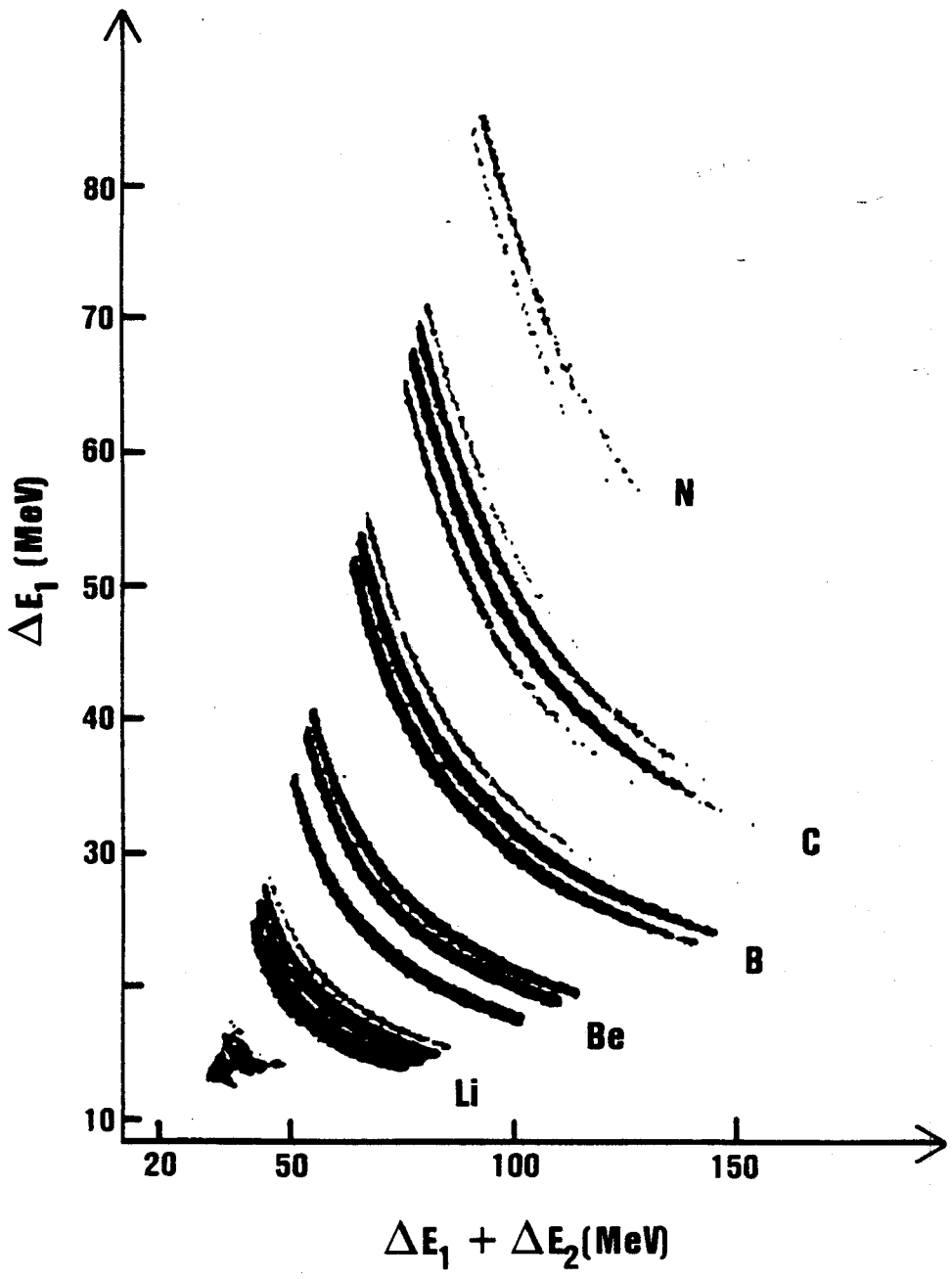

Figure 4.2.6. **A sample ΔE-E display of the triple element SSD telescope (100μ-400μ-5mm) used in the heavy fragment NSCL experiment is shown. The individual masses are clearly discernible.**

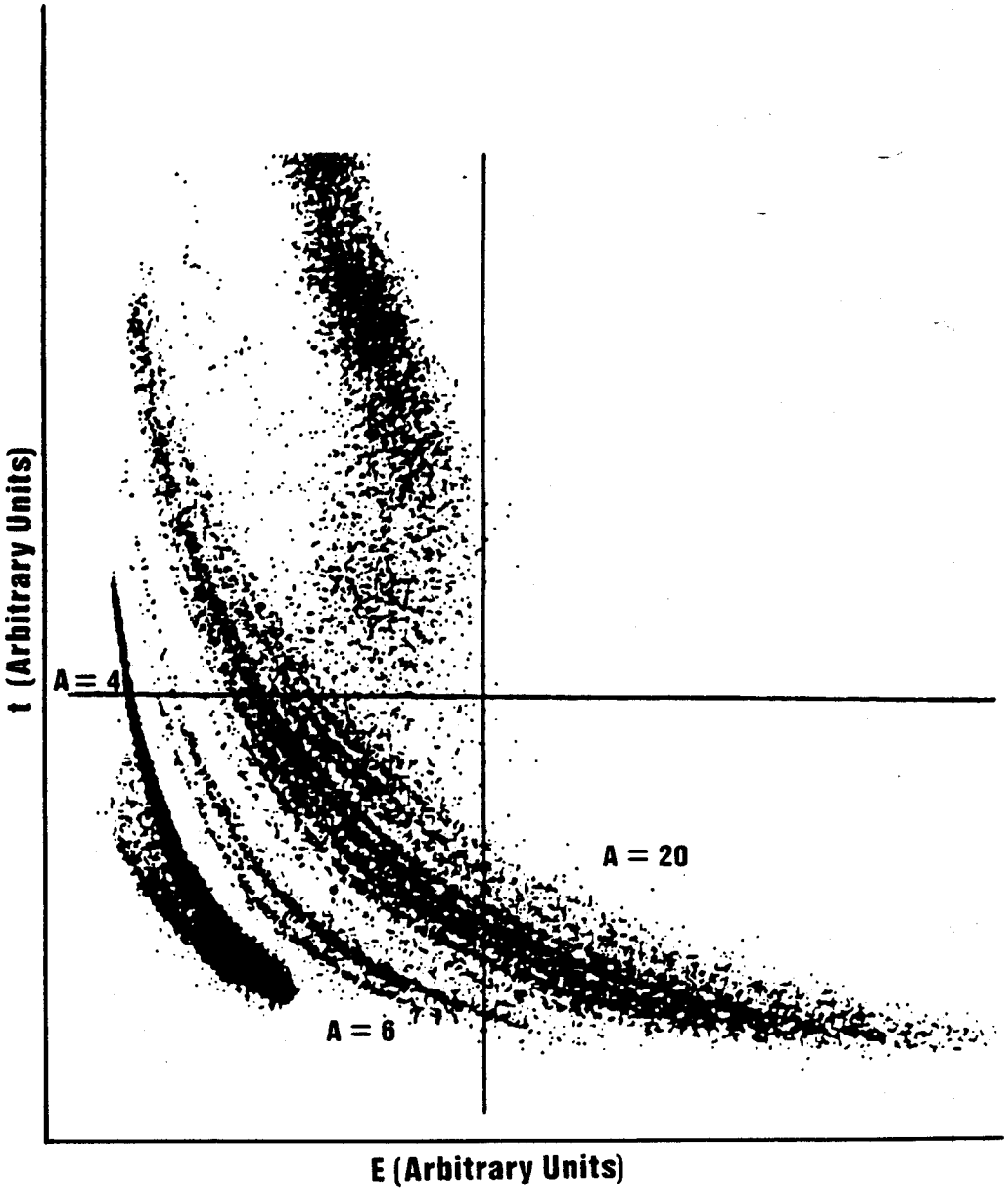

Figure 4.2.7. **TOF vs. total energy spectra obtained in the heavy fragment NSCL experiment, shows the separation of individual masses up to A= 20 .**

on the carbon contamination by selecting a charge from an Ag run (30A MeV) and attributing all of the cross section observed at an energy below the Coulomb Barrier to the carbon contamination present. The resultant maximum at the end of the experiment was 25 $\mu g/cm^2$. At the outset of the experiment, no visible indications of carbon contamination existed, implying a contamination of $< 2\ \mu g/cm^2$. If the resultant maximal errors are computed assuming a linear increase as a function of integrated beam current, we find that for $Z \geq 7$ the contribution for carbon in the differential cross section is $\leq 6\%$, while for $Z = 6$ it increases to $\cong 20\%$ for the 35A MeV data.

CHAPTER 5

RESULTS AND INTERPRETATION

5.1 Introduction

The results of the NSCL experiment designed to measure complex fragment production in reactions of $^{14}N + ^{nat}Ag$ at incident energies of 20A, 30A, and 35A MeV are presented in this chapter. The heavy fragment ($Z \geq 6$) differential cross sections for the two element ion chamber are presented for all energies measured. A logarithmic interpolation is constructed for the purpose of integrating the data over the measured angular interval. The results are presented and discussed, and predictions of the Compound Nucleus, Cold Shattering, and Liquid-Gas Models are compared with the data.

5.2 Heavy Fragment Results and Interpretations

Two dimensional ΔE-E ion chamber data at incident energies of 20A, 30A, and 35A were gated by charge and displayed for the angles measured, which result in energy spectra similar to Figure 5.2.1. These spectra were subsequently integrated over energy to produce the differential cross sections. The cross sections as a function of angle were determined after correcting for dead time and downscale factors, and the angle the target presents to the beam. The double differential cross sections as a function of E and θ_{LAB} for all particles and for all incident energies are shown in Appendix B.

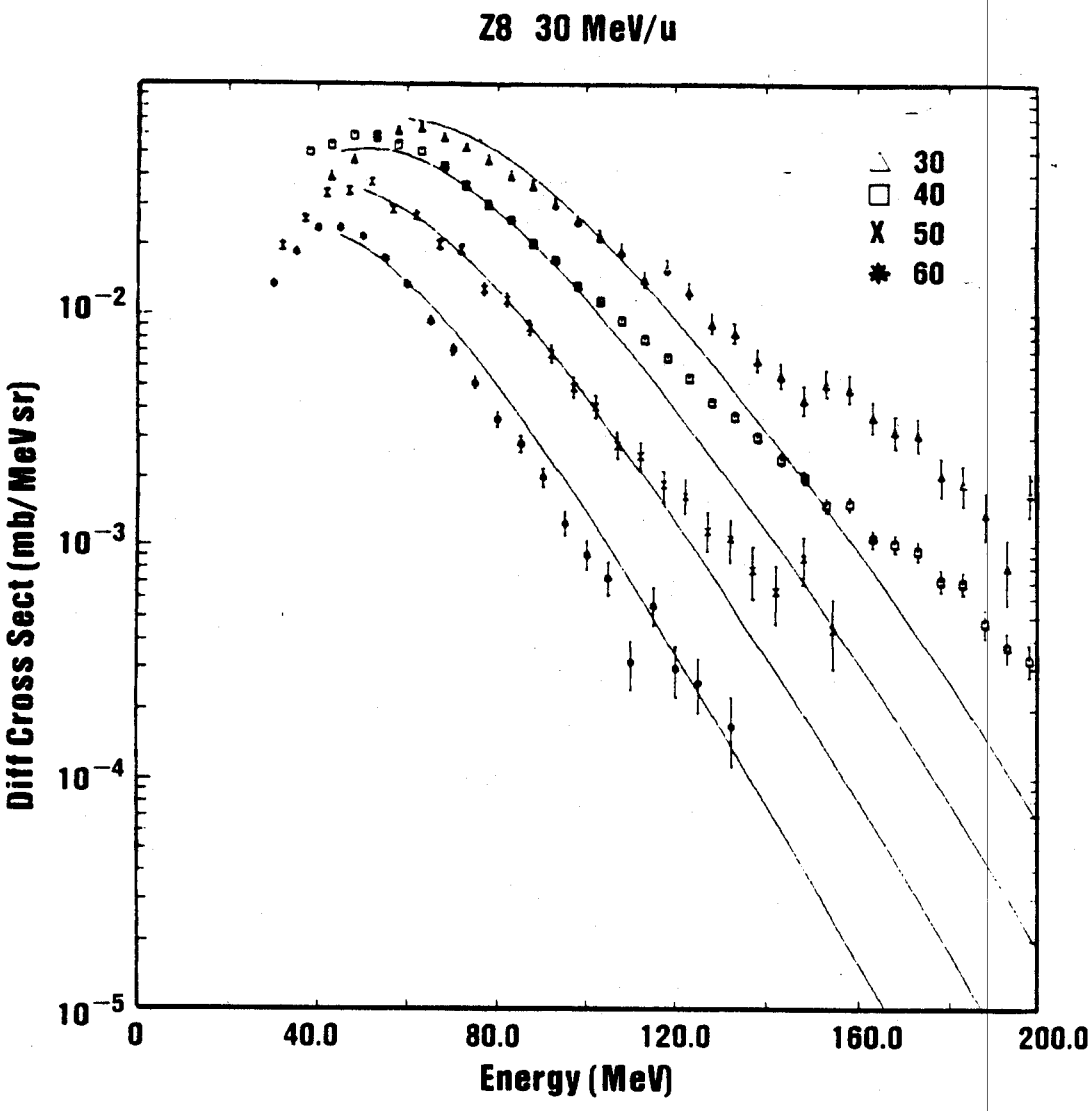

Figure 5.2.1. **An example of the differential cross sections for fragment Z = 8 in the reaction ^{14}N+Ag at E=30A MeV as a function of θ_{LAB} and energy. The solid lines indicate the best moving source fit. (See appendix A.)**

Energy integrated cross sections, $\frac{d\sigma}{d\Omega}$, are shown in Figures 5.2.2, 5.2.3, and 5.2.4 as a function of angle for individual elements at E_{inc} = 20A, 30A, and 35A MeV, respectively. The differential cross sections are found to fall faster than $\cong 1/\sin\theta$, thus implying that $\frac{d\sigma}{d\theta}$ is not constant in the center of mass frame. To illustrate this point, a prediction of the differential cross section in the lab frame for a fully equilibrated Compound Nucleus is shown for Z = 9 in Figure 5.2.2. The prediction is normalized to the 20° data point (an explanation of transformations between the C.M. and lab frames can be found in Marion (MAR 70)). (We recall from Section 3.3 that Compound Nucleus Fission predicts $d\sigma/d\theta$ = constant in the center of mass frame.)

Best fits are obtained for all data utilizing the following functional form

$$\frac{d\sigma}{d\Omega} = \sigma_0 \exp(-\theta/\theta_0) \qquad (5.2.1)$$

where σ_0 and θ_0 are constants to be determined. Results are tabulated in Table 6. Once the best fit constants σ_0 and θ_0 are determined, it is possible to obtain integrated cross sections. To confirm that the best fit representation accurately mirrors the behavior of the data, the data were also integrated point by point using the same functional form. This numerical integration yielded a ± 2% variation on average, the worst case being a 4.6% deviation, from the best fit estimations.

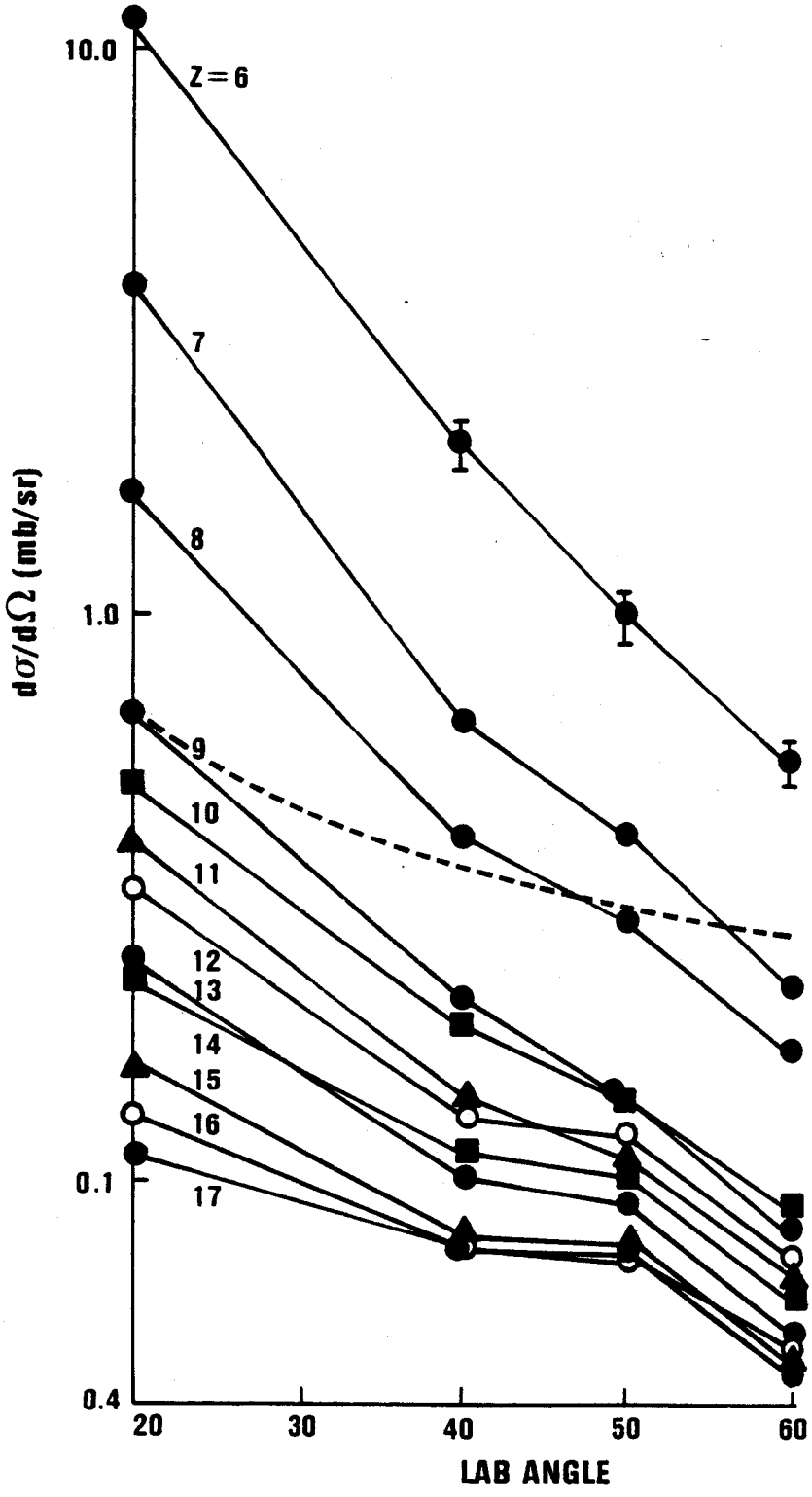

Figure 5.2.2. The differential cross sections $d\sigma/d\Omega$ vs. θ_{LAB} in the reaction $^{14}N+Ag$ at E_{inc} = 20A MeV. The dashed line represents the compound nucleus fission prediction for Z=9 normalized to the 20° data point.

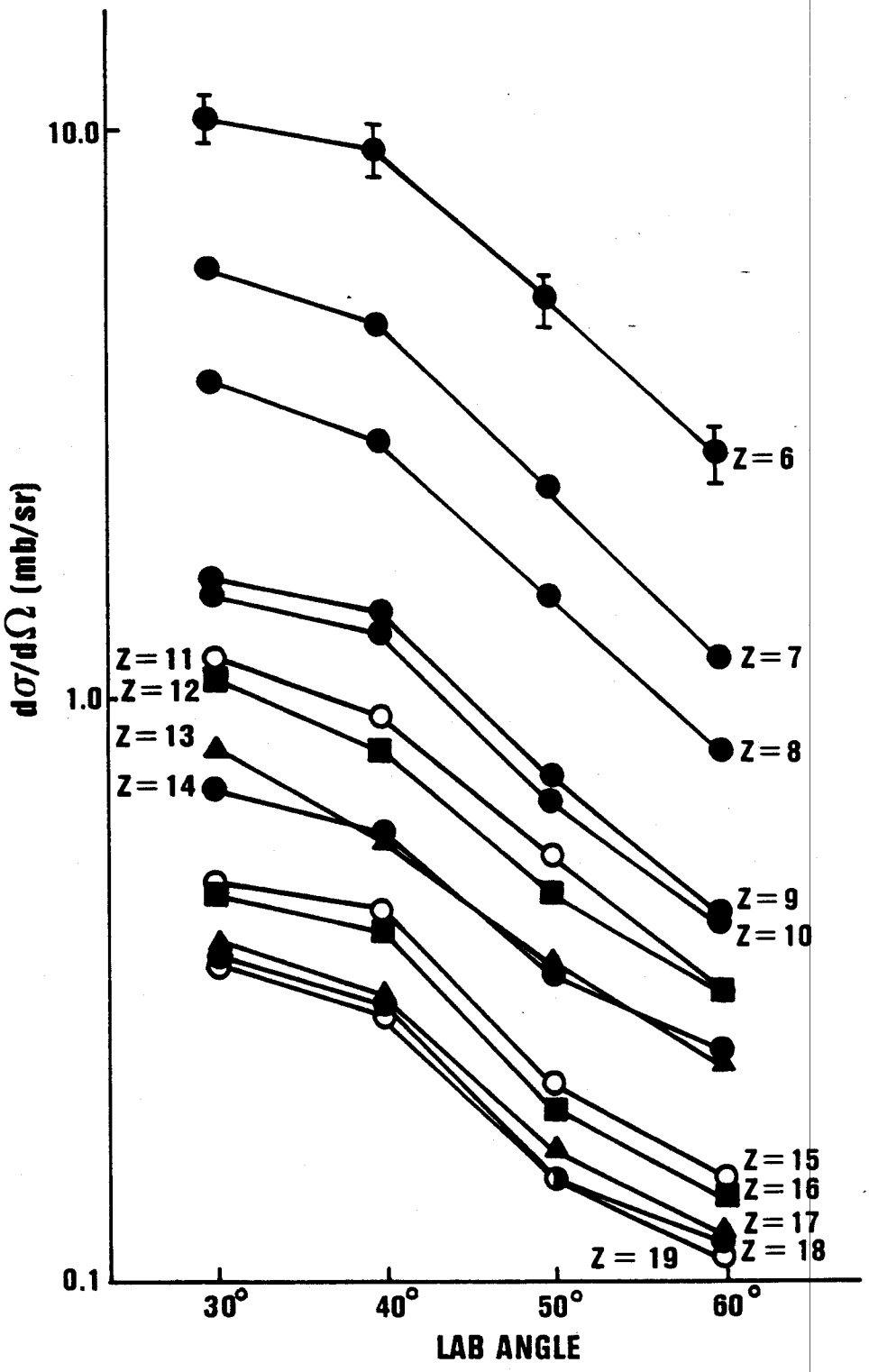

Figure 5.2.3. The differential cross sections $d\sigma/d\Omega$ vs. θ_{LAB} in the reaction ^{14}N – Ag at E_{inc} = 30A MeV.

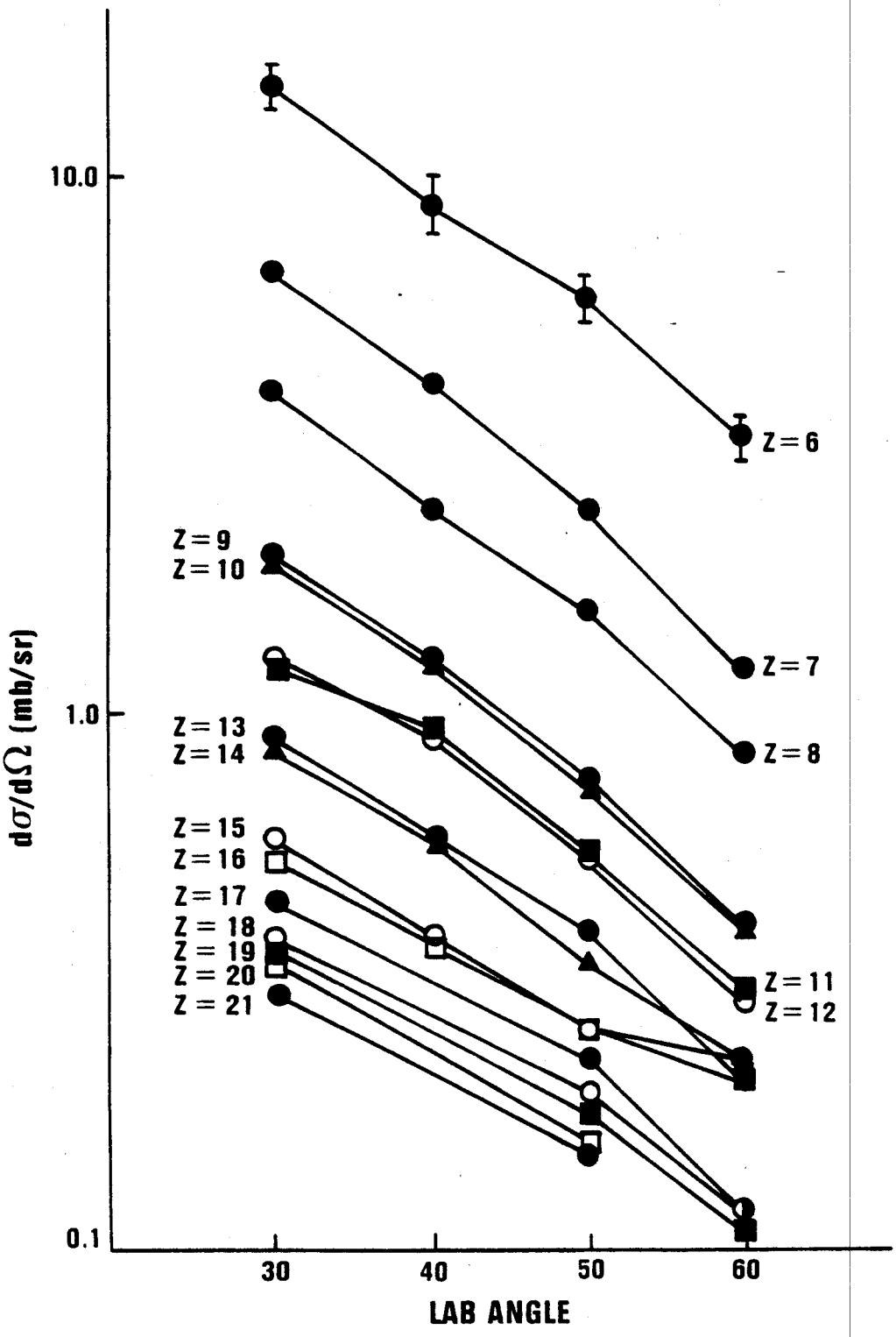

Figure 5.2.4. The differential cross sections $d\sigma/d\Omega$ vs. θ_{LAB} in the reaction $^{14}N + Ag$ at $E_{inc} = 35A$ MeV.

Table 6. The functional form of eq. (5.2.1) was fitted to the data shown in Figures 5.2.2-5.2.4. The best fit values for σ_0 ($\pm$ 10% $Z \leq 14$; $\pm$ 15% $Z \geq 15$) and θ_0 ($\pm$ .5% $Z \leq 14$; $\pm$ 2.5% $Z \geq 15$) are given for all measured charges at all incident energies. Incident energies are shown in parentheses.

Z	σ_0 (20A)	θ_0 (20A)	σ_0 (30A)	θ_0 (30A)	σ_0 (35A)	θ_0 (35A)
6	59	14.0	51	23.6	81	21.0
7	15	15.4	35	20.5	40	19.7
8	5.2	19.2	20	21.8	20	21.5
9	2.0	20.9	8.2	23.3	11	20.5
10	1.2	25.5	7.4	23.8	10	21.0
11	0.87	26.5	5.5	24.0	5.9	23.3
12	0.66	30.9	4.4	25.6	6.3	22.2
13	0.48	32.1	3.2	25.8	4.3	22.7
14	0.41	37.0	2.4	29.5	3.6	24.4
15	0.28	39.5	2.0	25.9	1.7	31.4
16	0.20	51.3	2.1	24.9	1.3	37.2
17	0.17	57.1	1.6	25.9	1.8	25.8
18	0.15	62.1	1.4	26.8	1.3	28.6
19	0.13	71.9	1.4	26.1	1.3	27.6
20			2.3	20.5	1.2	28.1
21			2.2	21.0	0.95	30.3
22					1.4	25.1
23					0.80	33.3
24					0.98	25.6

A further word is in order regarding the functional form. An alternate functional form was tried,

$$\frac{d\sigma}{d\theta} = C \exp(-\theta/\theta_0) , \qquad (5.2.2)$$

but the resultant χ^2 values were significantly worse than for the form in eq. (5.2.1). The two methods agreed to within ± 5% total yield, however.

The specific functional form chosen was used only to interpolate between data points; thus integrated cross sections are given only over the angular range actually measured. Cross section differences attributable to variations in the gate contours produced a maximal difference of ≅ 6% while cross section checks between the ion chamber and the three element SSD at the same angle yielded ± 5% differences. Cross calibration with the TOF system versus the ion chamber and the three element SSD yielded differences of 8.6% and 9.6% respectively. The E_{inc} = 35A MeV data were compared to similar data obtained in another experiment (GEL 85) utilizing the same projectile and target combination at 35A MeV and good agreement was obtained.

A comment is necessary on the differential cross section versus energy spectra. As can be seen in Figure 5.2.1, for Z = 8, the 30° sub-Coulomb barrier cross section appears to fall below the corresponding 40° cross section. Our data at energies both higher and lower than 30A MeV do not behave in this fashion (see

Appendix B). Hence the integrated 30A MeV data at 30° may be low. In fact, the data are low for all Z at 30°, as can be seen in Figure 5.2.3. This behavior may be either a real physical effect or indicative of an experimental problem with the normalization. However, for the purposes of the thesis, only the relative Z-to-Z cross sections are important. All integrated cross sections were compared to the total cross sections extracted from the best moving source fits (see Figure A.3), which have been used with considerable success to extrapolate total cross sections from measurements taken over limited angular ranges and energy. Appendix A gives the derivation of the method for calculating isotropic emission from a moving thermal source, with a functional form which corresponds to surface emission. The results of a single moving source fit to the present data can also be found in Appendix A. The results are shown in Table 7. Thus, we see that the Z-to-Z relative cross sections are stable for a given incident energy. Therefore, we claim that the relative Z-to-Z cross section uncertainties are less than or equal to 10%.

It is important to note that the relative Z-to-Z cross sections determine the value of the apparent exponent and Z_0, the number of charges in the fragmenting system. (A fit using the moving source results yields values of the apparent exponent viz., 2.8 (20A MeV), 2.9 (30A MeV), and 2.7 (35A MeV), commensurate with the results of this chapter; further explanation can be found in Appendix A.) The relative cross sections define the shape whereas

Table 7. A comparison of $\Delta\sigma(30°\text{-}60°)$ to σ_{TOT} (moving source) for each energy is given. The maximum deviation of any given element from the average is given in parentheses. The maximal Z-to-Z uncertainty in the data is 7% when compared to the single moving source model.

$(E/A)_{inc}$ (MeV/u)	ΔZ	$\frac{\Delta\sigma\ (30°\text{-}60°)}{\sigma_{TOT}\ (\text{moving source})} \cdot 100$
20	6-14	42 ± 5% (7%)
30	6-17	46 ± 3% (7%)
35	6-20	51 ± 3% (7%)

the absolute cross sections determine the normalization constants present in each of the predictions. The predictions that are central to this thesis rely on the stability of the relative Z-to-Z cross sections.

The total measured cross sections as a function of increasing charge are given in Figures 5.2.5, 5.2.6, and 5.2.7 for incident energies of 20A, 30A, and 35A MeV, respectively. If the best fit parameters are used to extrapolate to all angles, the total cross sections can be estimated. It is also useful to estimate the percentage of cross section actually measured. We find that the percentage remains constant as a function of Z and incident energy, and over the 30°-60° range the percentage is typically 33%-37%. The carbon and nitrogen yields at 20A MeV are the only exceptions and they are 24% and 27% respectively. Since the percentage of data measured is approximately constant with respect to the total, the apparent exponents should remain constant and this is indeed the case. The apparent exponent of the 20A MeV data increases slightly as anticipated, since the fraction of data measured decreased for Z = 6 and 7. Utilizing both the moving source best fit and the functional form of eq. (5.2.1) to extrapolate total cross sections indicates that the fraction of the cross section actually measured is relatively constant for all charges for any given energy. However, the absolute cross sections predicted by the moving source model are consistently smaller than those predicted utilizing eq. (5.2.1). Since lighter fragments are expected to originate from

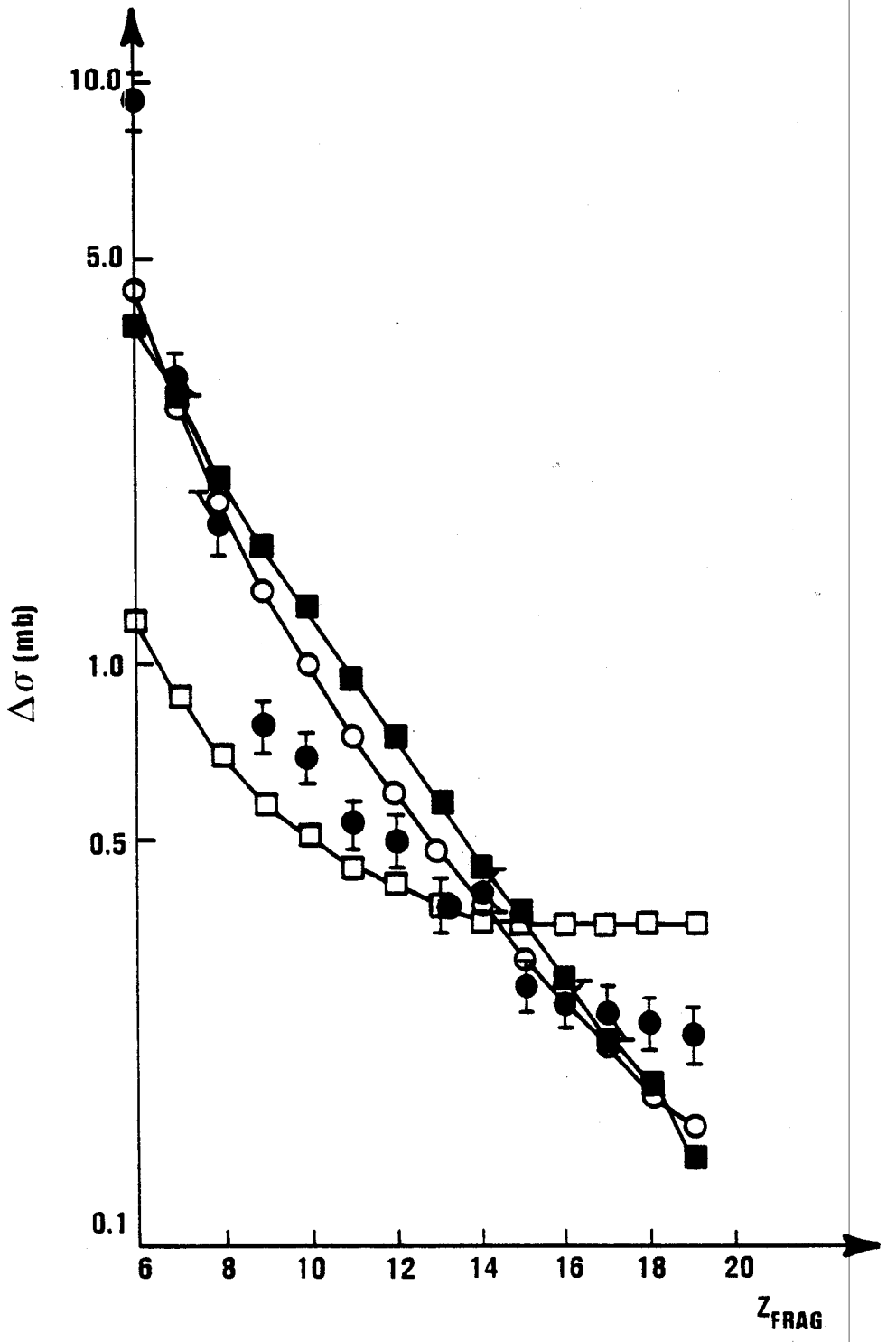

Figure 5.2.5. **The total measured cross sections as a function of increasing charge (●) for the 20 A MeV data. The best fit parameterizations for the compound nucleus (□), cold shattering model (■), and a macroscopic liquid gas parameterization with an apparent exponent (○) are also depicted. Error bars are shown at 10%.**

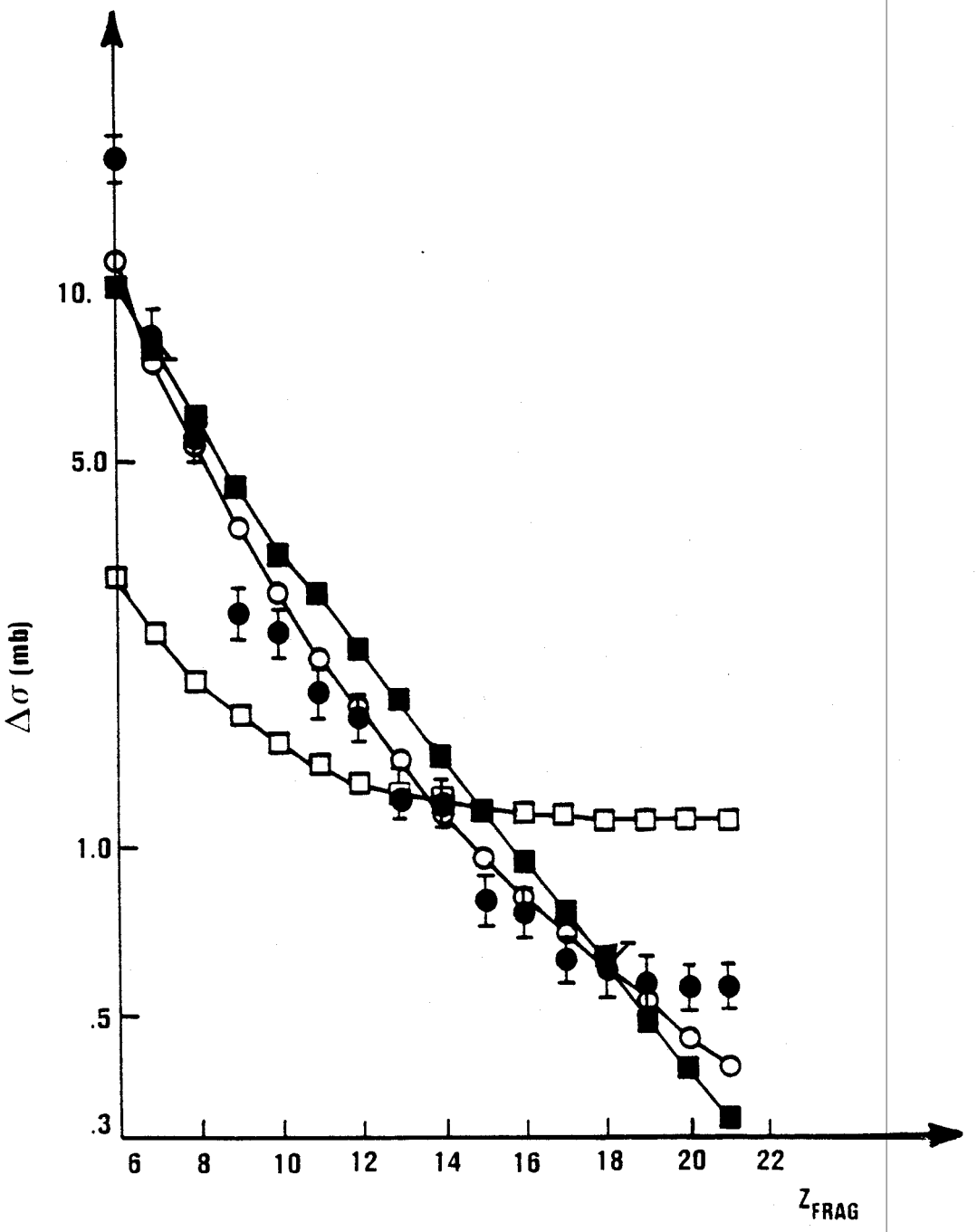

Figure 5.2.6. The total measured cross sections as a function of increasing charge (●) for the 30 A MeV data. The best fit parameterizations for the compound nucleus (□), cold shattering model (■), and a macroscopic liquid gas parameterization with an apparent exponent (○) are also depicted. Error bars are shown at 10%.

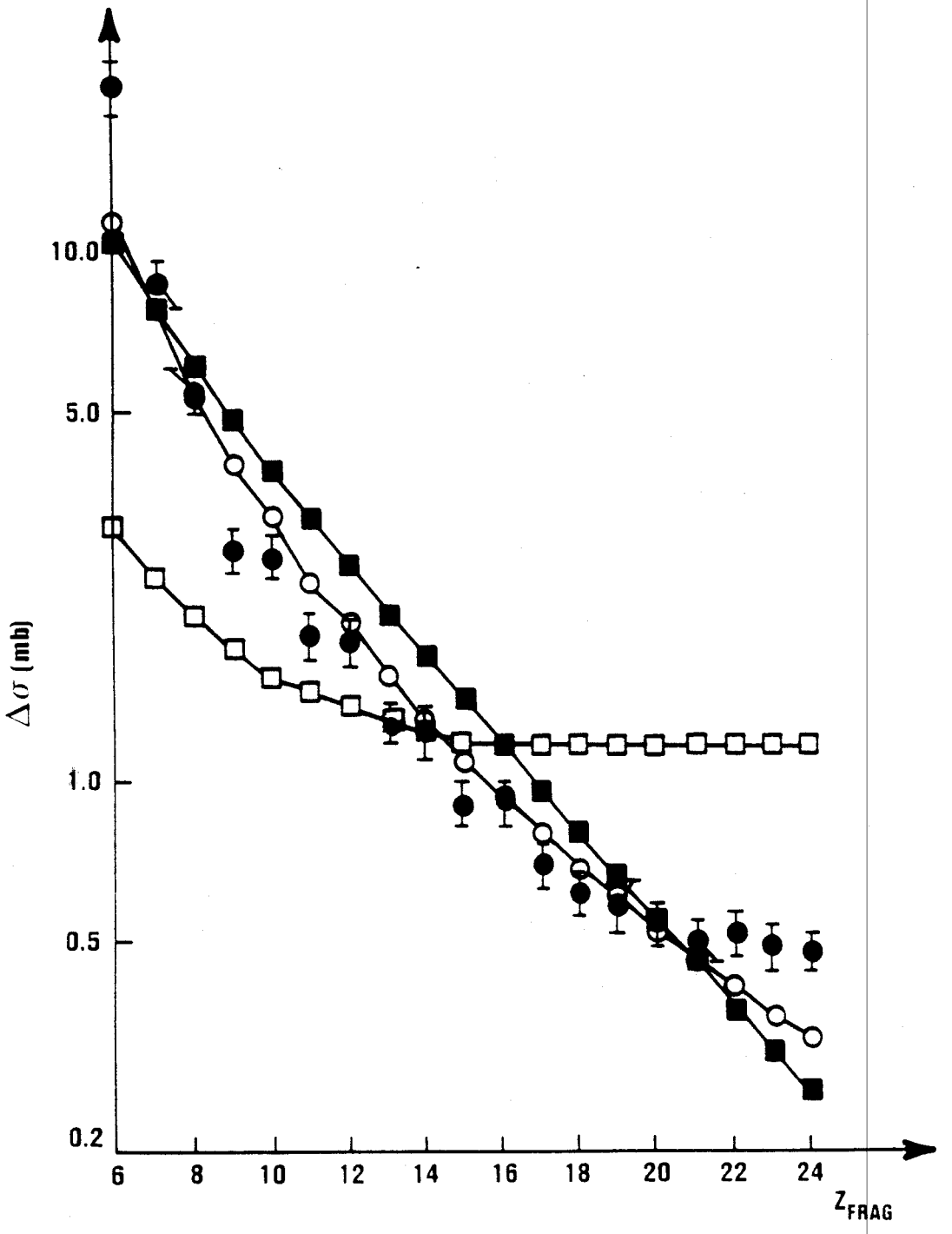

Figure 5.2.7. The total measured cross sections as a function of increasing charge (●) for the 35 A MeV data. The best fit parameterizations for the compound nucleus (□), cold shattering model (■), and a macroscopic liquid gas parameterization with an apparent exponent (○) are also depicted. Error bars are shown at 10% .

a different mechanism and since the data from the three element SSD do not include the Coulomb energy region where most of the yield occurs, only $Z \geq 6$ cross sections are fitted to the apparent exponent. Subsequently the $Z \geq 6$ data were fitted to the functional form $Y = CZ^{-\tau}$, where τ is the apparent exponent, analogous to the procedure described in Section 2.2.2.

The resultant best fit parameters are tabulated in Table 8 and the resultant fits displayed, together with the associated data, in Figures 5.2.5, 5.2.6, and 5.2.7. The values of the apparent exponent obtained in the current work (N + Ag at 280, 420, and 490 MeV incident energy) are shown in Figures 5.2.8 and 5.2.9, in the context of other values obtained in heavy ion and proton induced collisions (GRE 80; GRE; WES 78; FIN 82; POS 71; CHI 83). Several additional data points (^{18}O + Au, Ag at 1.5 GeV; C + Au, Ag at 0.58, 1.0 GeV; Ne + Au, Ag at 960 MeV) have been recently measured (SAN 84; TRO 85) and are included in Figures 5.2.8 and 5.2.9. The range of Z measured in these cases is small ($3 \leq Z \leq 13$) and hence the apparent exponent uncertainty is large. A discrepancy regarding the temperature assignment of the ^{18}O + Ag data at 84A MeV incident energy remains. In the work of Sann et al. (SAN 84) a temperature of 15.5 MeV was assigned, while Trockel et al. (TRO 85) assign a 17.4 MeV temperature. This single high energy data point is the only data point not clustered about $T \cong 15$ MeV.

For our data, the temperatures were determined in the same way we described in Section 2.2.2, i.e. a Fermi gas approximation was

Table 8. The best fit values of C and τ, the apparent exponent, are tabulated. The functional form is $Y(Z) = C \cdot Z^{-\tau}$.

$(E/A)_{inc}$(MeV/u)	C (mb)	τ
20	765	2.89
30	1,380	2.68
35	1,130	2.54

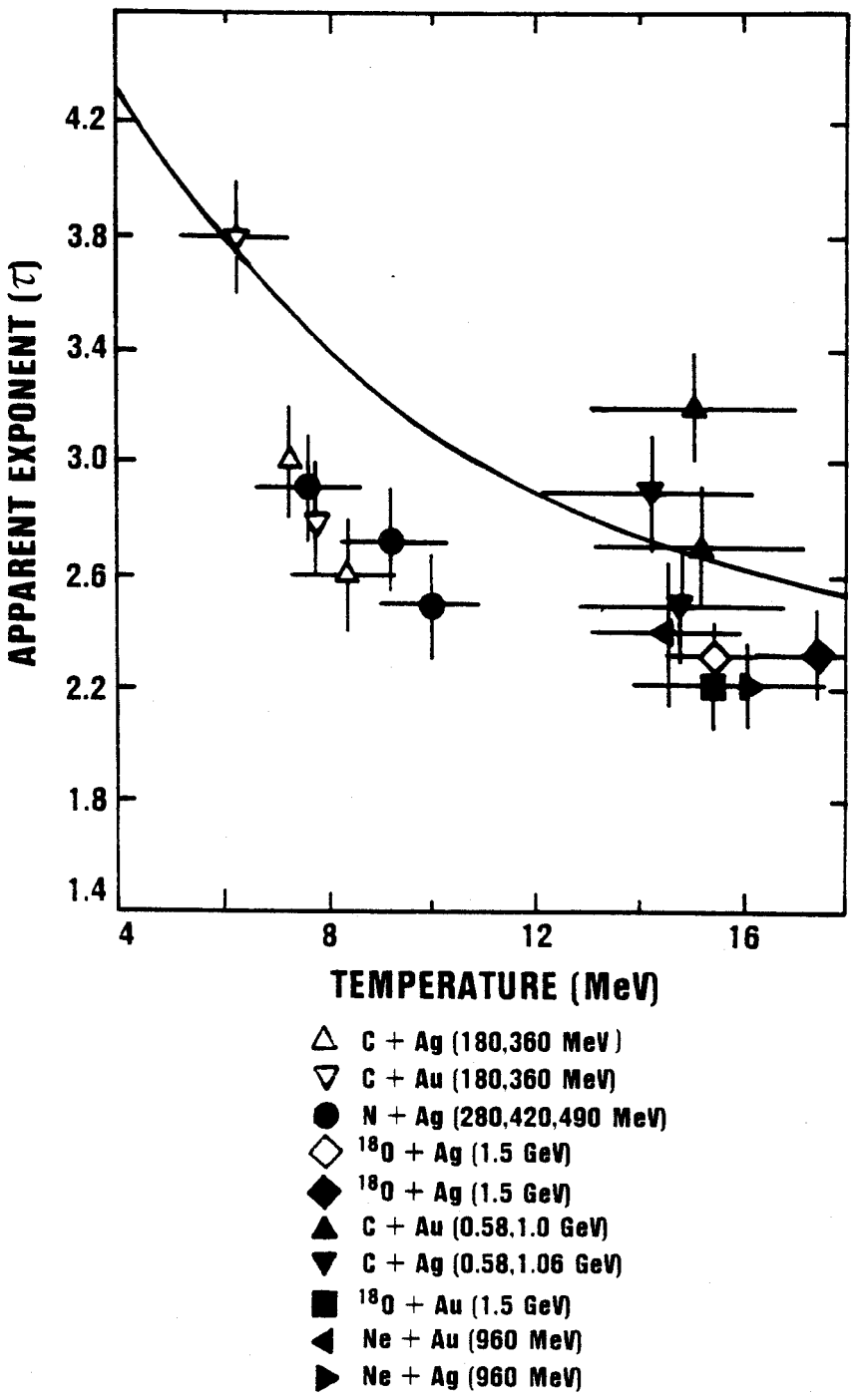

Figure 5.2.8. The apparent exponent vs. temperature for a variety of heavy ion induced reactions.

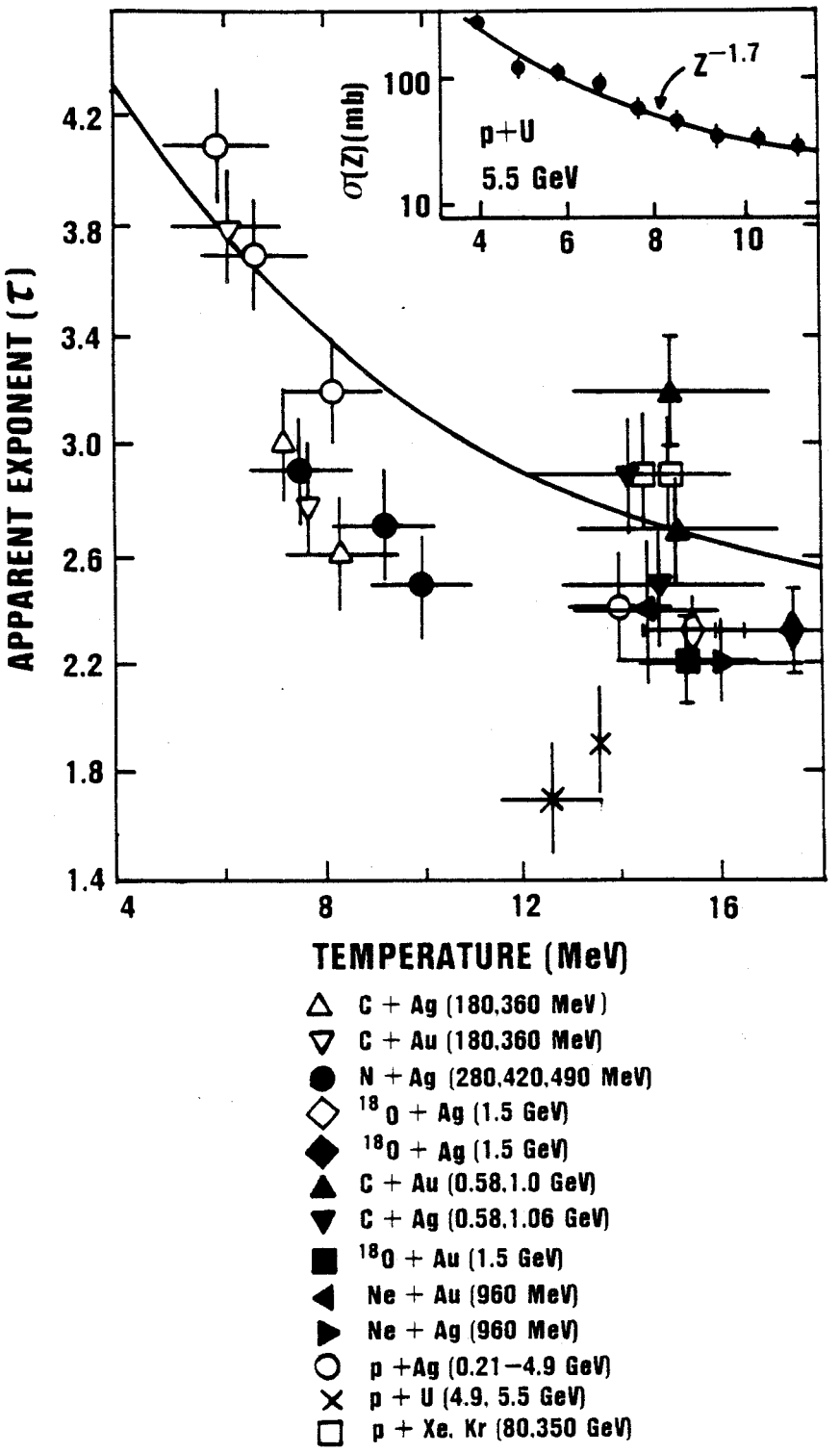

Figure 5.2.9. The apparent exponent versus temperature for heavy ion and p-induced reactions.

used to determine the temperature of the emitting system. A source size of 80 nucleons, approximately twice the size of the largest emitted fragment, was assumed. The temperature assignment probably represents the largest uncertainty regarding the conditions under which the fragments were formed. However, as stated in Section 2.2.2, the temperature of a given projectile-target system is expected to increase monotonically with increasing incident energy. The low energy behavior ($E_{inc} \leq 35A$ MeV) has now been explored with a consistent projectile-target combination, while the high energy branch is composed of several projectile-target combinations, none of which spans an appreciable temperature range. The recent results for the high energy branch, in conjunction with our added results for the low energy branch in Figure 5.2.8, serve to highlight the anomalous behavior between 10 and 14 MeV, but is is less clear that the complete assembly of data demonstrate the existence of the minimum of Figure 2.2.3. Thus, experiments utilizing the same projectile-target combination (N + Ag) at incident energies $\geq$ 40A MeV would be very useful. The heavy ion data are displayed in Figure 5.2.8 along with the Coulomb Tunneling predictions. It is readily apparent that if we are to rely solely on heavy ion induced reaction data, the range of temperatures between 10 and 15 MeV must be explored to ascertain whether a minimum or a saturation occurs. Recall that in Section 2.2.2, one characteristic of a liquid-gas phase instability is just such a minimum and that this minimum should occur at $\cong$ 12 MeV.

Although several arguments against utilizing proton induced reactions have been mentioned, for completeness we also compare the apparent exponent obtained with our results, bearing in mind these caveats (e.g. possible lack of compressional effects and limited energy deposition). The results are displayed in Figure 5.2.9. It has been pointed out that the two points for p + U, which are much lower than the remaining data points, may be anomalous because the emitted fragments must tunnel through a much larger Coulumb Barrier (BOA 84a). However, this argument may itself be flawed in light of the more recently acquired data (e.g. the ^{18}O and Ne + Au data) which have values of the apparent exponent similar to the other data and possess a comparable Coulomb Barrier.

The data are fitted to the functional form of eq. (2.2.16) and the parameterization (2.2.19) (PAN 84), viz.

$$Y(Z) = CZ^{-1.7} \exp[-b(1 - \frac{T}{T_C})^2 Z^{2/3}] \qquad (5.2.3)$$

allowing only the normalization and the parameter b to vary, while keeping the critical exponent constant (k = 1.7) and the critical temperature constant (T_C = 12 MeV). Since $T < T_C$ the surface form of the macroscopic liquid-gas formulation is used. The best fit values of C and b are listed in Table 9; the best fits from this functional form are found to be worse than the values obtained with the $Y = CZ^{-\tau}$ functional form.

Compound nucleus predictions of the form

Table 9. The best fit values used in the Fisher model of a liquid-gas phase transition where k and T are fixed a priori at the values 1.7 and 12 MeV as obtained by Panagiotou et al. (PAN 84). The temperatures are deduced from a Fermi gas approximation assuming a source size of 80 nucleons.

$(E/A)_{inc}$ (MeV/u)	C (mb)	b	T (MeV)
20	765.1	3.7	7.5
30	1,380.2	7.9	9.2
35	1,130.0	12.0	9.9

$$\sigma(Z) = \sigma_0 \exp(-\Delta E/T) \qquad (5.2.4)$$

are also plotted in Figures 5.2.5, 5.2.6, and 5.2.7 where the mass of the fragment is assumed to reflect the N/Z ratio of the projectile target combination and ΔE is the energy released during compound nucleus formation (see Section 3.3). The compound nucleus temperatures calculated by means of a Fermi gas approximation are 6.1, 7.5, and 8.0 MeV for incident energies of 20A, 30A, and 35A MeV, respectively. The normalization is considered a free parameter.

If the differential cross sections, $d\sigma/d\theta$, are plotted as a function of the center of mass angle of the compound system, then it is clear that all cross sections fall at backward angles; hence the emission occurs prior to full equilibration of the compound nucleus. This can also be seen upon examination of $d\sigma/d\Omega$ $(= (2\pi \sin\theta)^{-1} d\sigma/d\theta)$ versus θ_{LAB} (see Figure 5.2.2).

A best fit to the cross section predicted by the Shattering Model (see Section 3.4) as a function of Z is also depicted in Figures 5.2.5-5.2.7; the corresponding best fit parameters are tabulated in Table 10. Clearly, the approximately linear behavior of large Z fragments predicted in eq. (3.4.4), viz.,

$$\ell n\sigma \cong - \frac{1.28}{\sqrt{Z_0}} Z + \ell n\sigma_0 \qquad (5.2.5)$$

is not observed.

Table 10. The best fit values are tabulated for the Cold Shattering Model as applied to the current data. σ_0 is a normalization constant while Z_0 is indicative of the number of charges in the fragmenting system.

$(E/A)_{inc}$ (MeV/u)	σ_0 (mb)	Z_0
20	11.77	29.57
30	25.74	37.81
35	20.32	49.74

Finally, the cross sections for elements $6 \leq Z \leq 19$ are plotted as a function of increasing total incident energy imparted to the colliding system in Figure 5.2.10. It is interesting to note that the production cross sections rise sharply between 20A MeV and 30A MeV incident energy and appear to saturate between 30A MeV and 35A MeV incident energy. This could be interpreted as evidence for the onset of limiting fragmentation. Limiting fragmentation (BEN 69; SCO 80) is defined as a saturation of the production cross section as the incident energy supplied to the system increases. This behavior may indicate that only a limited amount of energy can be supplied to the system using heavy ion collisions.

A note of caution regarding this interpretation is in order, since only the cross sections over the 30° to 60° angular range are shown. The fraction of the total cross section represented by this finite angular range may vary as a function of the incident energy. The best fit with the functional form of eq. (5.2.1) indicates that the fraction of data in the 30° to 60° range is relatively constant. However, further experiments which measure cross sections over a larger angular range will be required before a definitive conclusion can be reached.

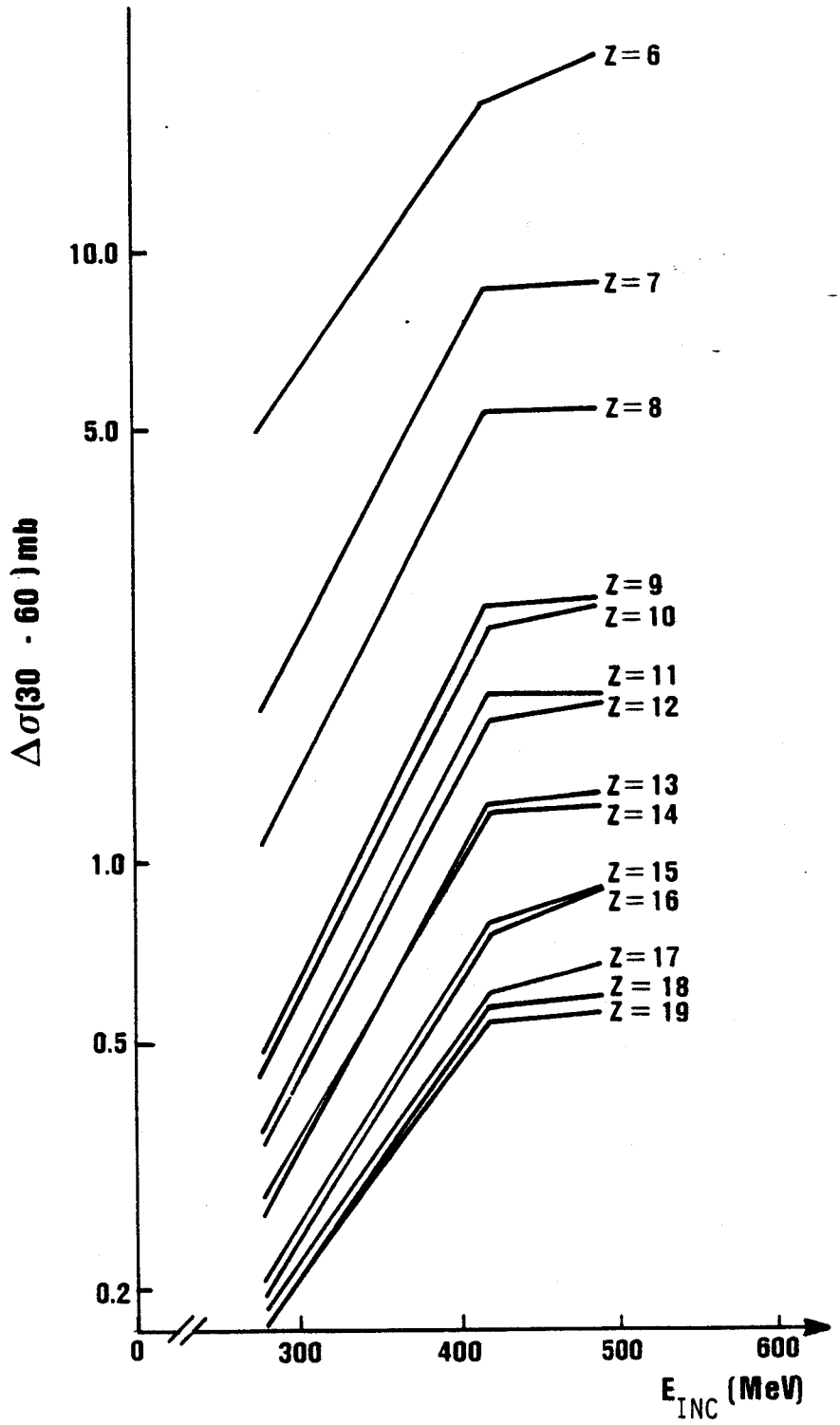

Figure 5.2.10 $\Delta\sigma$ vs. E_{INC} for the heavy fragment NSCL experiment are presented for fragment charges $6 \leq Z \leq 19$. The data indicate that a limiting fragmentation mechanism in heavy ion collisions may set in above 35A MeV for ^{14}N induced reactions.

CHAPTER 6

CONCLUSIONS AND FUTURE PROSPECTS

A variety of light ion fragment experiments (WES 82; WES 83) show that reactions at high incident energies dominantly produce fragments with $1 \leq A \leq 4$ as anticipated from thermal and coalescence model predictions. However, as the incident energy is decreased the relative yield of α particles increases relative to the lighter fragment production cross sections. Two possible explanations were proposed (CUR 83a) which raise some ambiguities regarding light fragment production and subsequent interactions. One possible explanation of the increase in yield stems from the greater relative importance of binding energy effects at low energy densities (CUR 82a). Another explanation is a possible liquid-gas phase transition. It was believed that measurements of heavier fragments could help to resolve the ambiguities. A further unattractive feature of the light fragments is the subsequent contamination of the primary distribution by sequential decays of heavier fragments.

A simple Compound Nuclear model does not agree well with the data, predicting as it does an essentially flat distribution of ln (Z) as a function of Z for $Z \geq 12$ whereas the data continue to fall with increasing Z as can be seen in Figures 5.2.5-5.2.7. The angular distributions also indicate that full compound nuclear

equilibration does not take place and that only a fraction of the total system is thermalized.

Coincidence experiments could clarify whether the reactions under consideration are binary or not. Further theoretical work exploring the effects of angular momentum on fission processes is also necessary. (We recall that the simplified treatment shown in Section 3.3 ignored contributions from angular momenta other than $\ell = 0$.)

The macroscopic model of a Liquid-Gas Phase Transition shows a measure of agreement with the data; however, the data only reinforce the original observation that the region $10 \leq T \leq 15$ MeV is the critical region of interest. The heavy ion data, at present, do not clearly indicate whether or not the apparent exponent decreases with increasing energy and then abruptly saturates at a constant level, or decreases and then increases for further incident energy increments. The new data (SAN 84; TRO 85) do, however, indicate a very rapid change of the apparent exponent over a small temperature interval near $T = 15$ MeV. It is interesting to note that the data obtained over incident energies from 48A MeV to 84A MeV produce little variation of the deduced temperature. This behavior could indicate an onset of saturation of the temperature. It is clear from our results, combined with other recent experiments, that further information pertinent to a liquid-gas phase transition will come from heavy ion collisions at $35A \leq E_{inc} \leq 50A$ MeV. Higher

energy measurements should also serve to indicate whether the behavior approaches the limit of the coalescence model.

Sequential decays will depopulate the heavier fragments while populating the lighter fragments, thus increasing the apparent exponent. This effect will become more pronounced as the temperature increases. If the temperature increases with increasing incident energy then the net result will be to reduce the increase in the apparent exponent. This effect could tend to mask the signature of a liquid-gas phase transition.

It is also useful to remove ambiguities associated with temperature assignments to various reactions. To this end, it is desirable to use a single projectile-target combination over a wide range of incident energies. Our work marks the first step in such a program. The light projectiles and medium mass targets provide kinematically clean spectra and a large Z range which is uncontaminated by fission processes. Observation of the yields versus fragment charge in the reaction $^{12}C + ^{197}Au$ at incident energies of 15A and 30A MeV (CHI 83), exhibit the characteristic exponential fall off for increasing Z until a minimum is attained followed by an increase in the yields for further increments in Z. A similar trend is observed for other reactions on many targets (GRO 82; HUF 84). It is generally believed that this increase is due to fission processes.

One proposed feature of the liquid-gas phase transition is a diminishing size of the largest emitted fragment mass as a function

of increasing temperature (SCH 83). The theory predicts that as the temperature of the system increases the size of the largest stable fragment diminishes until the largest fragment consists of a single nucleon which defines the critical temperature (T_c). The formulation is similar to an in-medium evaporation model. However, the data in Figures 5.2.5 through 5.2.7 and Table 6 seem to indicate that the maximum fragment size produced increases slightly as the incident energy increases, in contradiction to this prediction.

It would appear that the cross sections saturate with increasing total incident energy. One possible effect of limiting fragmentation is that only a limited amount of the initial projectile kinetic energy can be deposited in the overlap region. If this limited amount of energy produces a temperature less than the critical temperature required for a liquid gas phase transition then the possibility of observing such a transition utilizing heavy ion collisions is remote. It is important to note that this comment does not address whether a system of nuclear matter undergoes a phase transition or not, but rather whether heavy ion collisions will convey information pertinent to such a transition.

One possible observable of a mechanical instability, as opposed to a chemical instability, is the rapid onset of d and t production with increasing incident energy; however, the data do not clearly indicate that this occurs. A new version of the mechanical instability model (LOP 84) which combines an initial mechanical instability and a subsequent chemical instability at or near "freeze

out" has been proposed. Coincidence measurements will be needed to ascertain possible energy dependences of the "freeze out" volumes (CHI 85). The yields presumably will have a similar behavior to those anticipated for a liquid-gas phase transition. Thus the present results are not inconsistent with this model. While it is difficult to imagine an evaporative model reproducing the observed behavior of the apparent exponent, this possibility cannot be definitely ruled out, given that predictions exist only for $Z \leq 10$ (see Friedman and Lynch (FRI 83) and Chitwood et al. (CHI 83) for a comparison to data). Equally difficult is the task of reconciling the data with the Coulomb Tunneling Model which predicts a less severe fall off for the apparent exponent as a function of increasing temperature than indicated in the data, and furthermore predicts no minimum or discontinuity in the apparent exponent.

Currently some controversy exists regarding the basic assumptions of the theoretical approach based on information theory which is inherent in the Cold Shattering Model of the cold breakup of nuclear matter. A more elaborate treatment may significantly alter the conclusions which were drawn from previous data (SOB 85a). Aside from this particular controversy, a fundamental discrepancy exists regarding the absence of characteristic γ rays (see Section 3.5.3 and Morrissey et al. (MOR 84)) anticipated if $\rho = \rho_0$ nuclear systems are produced by a system at a given temperature. The temperatures deduced from such experiments (< 1 MeV) are much lower than temperatures deduced from moving source fits ($\cong$ 8-9 MeV).

The argument relies on the fact that a given pair of quantum levels, which are not daughters of higher lying states, should be populated in a true thermal system, to an extent allowed by the Boltzmann factor. If the higher state cannot be fed from higher lying states and decays only to the ground state then the relative population of the two states, after normalizing the ground state for population enhancement due to other decay channels, should yield a determination of the temperature. One must be careful to ensure that no particle unstable states decay into the higher lying state, or else that these decays are adequately taken into account in order to ensure that the measurement applies to the initial system. Since the cold nuclear matter breakup involves $\rho = \rho_0$ matter, it is difficult to explain observations in terms of this model. However, models involving changes in the density have no such difficulty since the quantum levels are themselves altered. This point was discussed in Section 3.5.3 in dealing with experimentally complicating factors.

Even setting aside these objections, it seems clear that comparison of the data with a theory, based on a minimal information approach for the yields versus charge, indicates that this is not the mechanism responsible for the observed yields. As stated in Section 3.4, the prediction of the theory is approximately linear in the $Z \geq 10$ region on a semilog plot of cross section versus Z. It was established that a power law yields a superior fit to the data.

It is important to note that the liquid-gas phase transition is not the only theory which predicts the critical behavior of an apparent exponent. Recently, it was shown that a percolation phase transition, which predicts behavior similar to the trends of the inclusive fragment yields, could also explain the data (BAU 85; CAM 85). This is a nonequilibrium phase transition in contrast to the equilibrium liquid gas phase transition.

In the percolation model (as discussed in Section 2.2.3), the nuclear medium is described in terms of a lattice. Two applications of the percolation philosophy have been proposed. One describes the critical behavior in terms of the normalized probability that bonds between adjacent points are intact or broken (BAU 85) while the other describes the normalized probability that a given lattice site is occupied or vacant (CAM 85). The functional form of the yields behave exactly as described in the Fisher prescription (FIS 67). Insofar as the functional forms of the percolation and liquid gas phase transition predictions are the same, the comments regarding a comparison of the liquid gas theory to the data are also equally applicable to the percolation theory predictions. Additional constraints attempting to simulate nuclear bonds and the behavior of nuclear fragments have been incorporated into the traditional percolation theory (CAM 85). For an estimate of the equivalent temperature where critical behavior manifests itself, note that each occupied site corresponds to the release of $\cong$ 8 MeV, and hence the total energy supplied to the system is 8Np, where N is the maximum

number of possible occupied sites. A Fermi energy corresponds to $AT^2/8$ MeV where A becomes the number of vacant sites remaining in the system; hence A is equal to $N(1 - p)$. Thus we see that the effective critical temperature associated with a percolation theory is $8[p_c/(1 - p_c)]^{1/2}$. Examination of three dimensional systems yields a value $p_c \cong 0.7$ inferring critical behavior could be anticipated at an effective critical temperature of approximately 12 MeV. This result is in good agreement with our experimental data. Of course, it is not correct to interpret this quantity as a true temperature; rather the comparison allows the reader to interpret the percolation theory within the framework we have used to describe the data.

Interatomic potentials exhibit long range attractive and short range repulsive characteristics similar in nature to the nuclear potential. Recently, such a potential was used to simulate heavy ion collisions (VIC 84). Although the apparent exponent in this model also exhibits a minimum as a function of the incident energy, it is asserted that the minimum does not correspond to behavior near a critical point. Possibly the behavior is more reminiscent of the Mechanical Instability discussed in Section 2.3.

Further comparisons of these various experimental approaches are clearly desirable. Certainly, more experimental data are required to clearly establish when and if an abrupt transition to multifragmentation processes occurs, and whether a phase transition at the critical temperature for a liquid-gas model exists. It is

also important to gain further insight into the final state interactions which govern the evolution from the primary fragment distributions to the fragment distributions observed in our detectors. This will not only require extensive experimental investigation, but also theoretical calculations of the evolution, which becomes especially difficult if greater than normal nuclear densities are involved. And if the barriers to reaching the goal of experimentally accessible signatures are eventually overcome, subsequent refinements of the theoretical framework of phase transitions will also be essential.

APPENDICES

APPENDIX A

SINGLE MOVING SOURCE ANALYSIS

APPENDIX A

SINGLE MOVING SOURCE ANALYSIS

We assume isotropic emission in the rest frame of the emitting system, given by

$$\frac{d^2\sigma}{dEd\Omega} = \sigma_0 E \exp(-E/T) \qquad (A.1)$$

where T is the ambient temperature of the emitting system, E is the kinetic energy in the rest frame of the source, and σ_0 is a normalization constant. This form corresponds to surface emission. Upon transformation to the laboratory system one obtains the following non-relativistic form (FIE 84),

$$\frac{d^2\sigma}{dEd\Omega} = \sigma_0[(E_{lab} - V_C)E]^{1/2} \exp(-E/T) \qquad (A.2)$$

where

$$E = E_{lab} - V_C + E_S - 2[E_S(E_{lab} - V_C)]^{1/2} \cos\theta_{lab}$$

and

$$E_S = A_F(M_0c^2)\beta_S^2/2 \quad .$$

The quantity E_{lab} is the fragment kinetic energy in the lab frame and β_S is the velocity of the moving source divided by the speed of light.

The differential cross sections of each individual isotope (for the three element solid state telescope) and charge (for the ion chamber) were fitted individually. The resultant source temperatures, masses, and cross sections for the SSD telescope are tabulated in Tables 11 through 13 and the results for the ion chamber data are plotted in Figures A.1 through A.4. Since the angular range sampled in this particular experiment is quite narrow, the extraction of source parameters must be viewed with some caution.

The temperatures of the light fragments are almost constant though the heavier fragments appear to originate from larger sources (see Figure A.1), moving with smaller velocities (see Figure A.2), for the 20A MeV data while the 30A and 35A MeV data show more uniformity. To illustrate the cautionary note of the preceding paragraph, we note that for $Z \geq 16$ at 35A MeV incident energy, the source size parameter exceeds the compound nucleus size which is an absolute upper bound. We must also exercise caution when interpreting the cross section extrapolations for light fragments ($Z \leq 5$), since we did not measure down to the Coulomb barrier for these fragments.

The fits for the heavy fragments show the characteristic A^{-k} dependence yielding values of 2.8 (20A MeV), 2.9 (30A MeV), and 2.7

Table 11. Best fit moving source parameters for the light fragments measured using the triple element SSD telescope for 20A MeV incident energy.

Element	σ_{TOT}(mb)	T (MeV)	A_s	v_s/c
^{6}Li	7.2	7.7	32	.089
^{7}Li	8.9	8.2	34	.085
^{7}Be	2.3	8.6	30	.096
^{9}Be	2.8	9.6	37	.078
^{10}Be	1.3	10.1	37	.078
^{10}B	2.2	9.4	34	.085
^{11}B	3.5	10.0	34	.085
^{11}C	0.64	8.8	33	.088
^{12}C	2.2	9.6	37	.078
^{13}C	1.4	9.9	38	.076
^{14}C	0.42	9.9	40	.072
^{14}N	0.45	10.6	38	.076
^{15}N	0.83	10.4	43	.067

Table 12. Best fit moving source parameters for the light fragments measured using the triple element SSD telescope for 30A MeV incident energy.

Element	σ_{TOT}(mb)	T (MeV)	A_s	v_s/c
^{7}Be	18.5	10.51	40	.089
^{9}Be	18.6	10.55	50	.071
^{10}Be	9.8	10.88	46	.077
^{10}B	13.8	10.94	43	.082
^{11}B	23.2	10.98	46	.077
^{12}B	3.0	10.47	50	.071
^{11}C	4.0	11.6	42	.084
^{12}C	14.8	12.3	46	.077
^{13}C	8.6	12.09	46	.077
^{14}C	3.2	12.63	54	.066
^{14}N	2.9	11.39	38	.093
^{15}N	5.7	11.71	44	.081

Table 13. Best fit moving source parameters for the light fragments measured using the triple element SSD telescope for 35A MeV incident energy.

Element	σ_{TOT}(mb)	T (MeV)	A_s	v_s/c
^{10}B	14.1	14.8	56	.068
^{11}B	25.1	13.9	59	.065
^{11}C	3.7	12.7	43	.089
^{12}C	13.0	12.2	48	.08
^{13}C	9.6	11.9	51	.075
^{14}C	3.2	12.1	54	.071
^{14}N	2.9	14.0	46	.083
^{15}N	8.1	10.8	43	.089

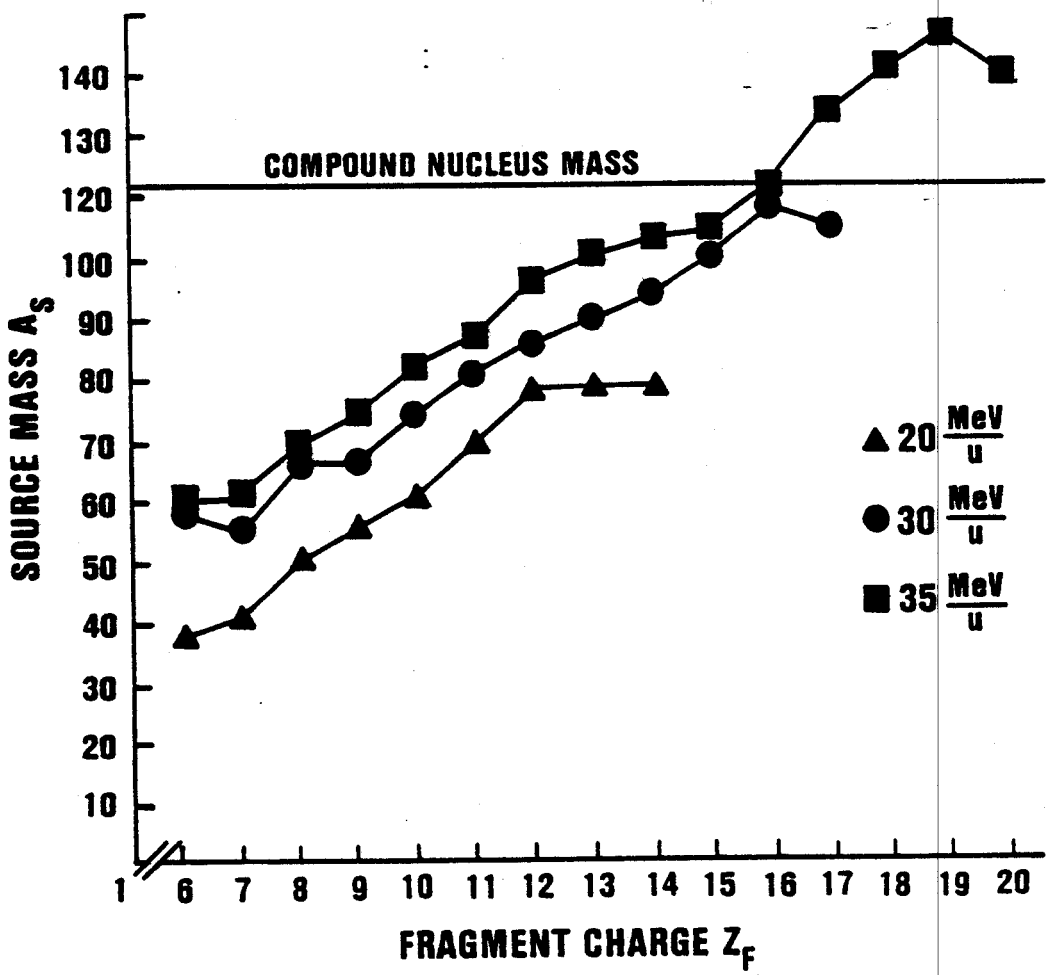

Figure A.1. Source size as a function of fragment charge determined from the best single moving source fit to the data. The compound nucleus mass represents the upper bound on the source size and is indicated in the figure.

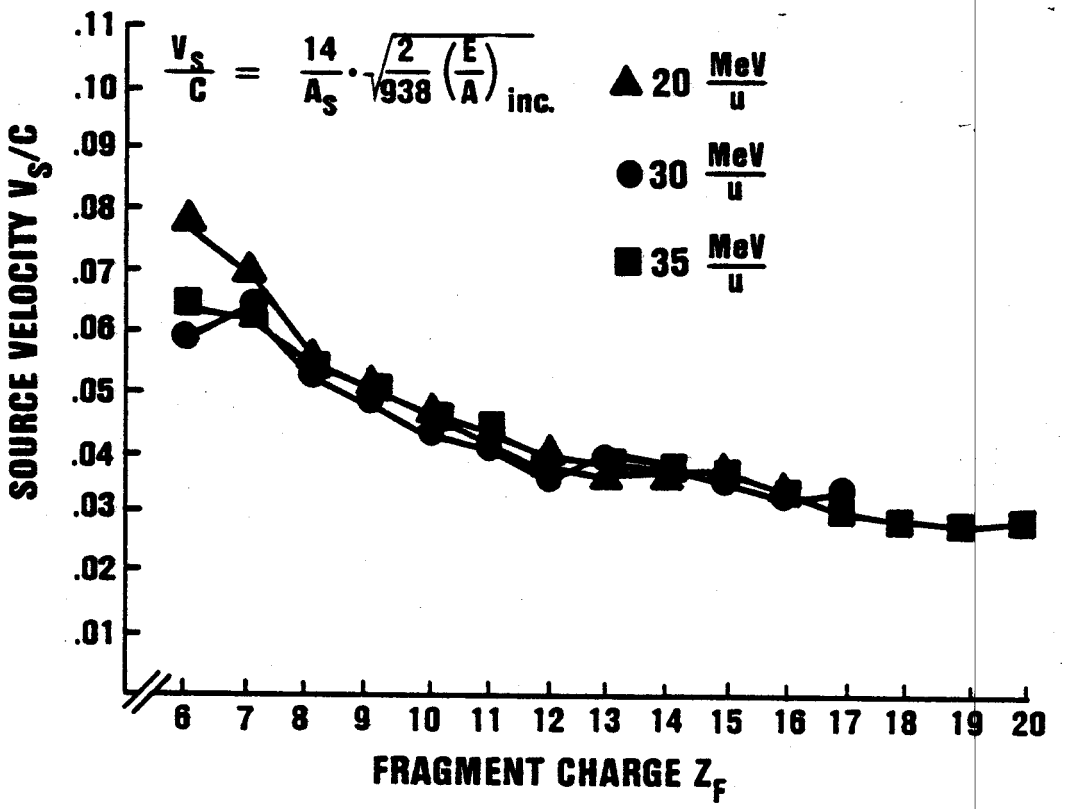

Figure A.2. **Source velocity as a function of fragment charge determined from the best single moving source fit to the data.**

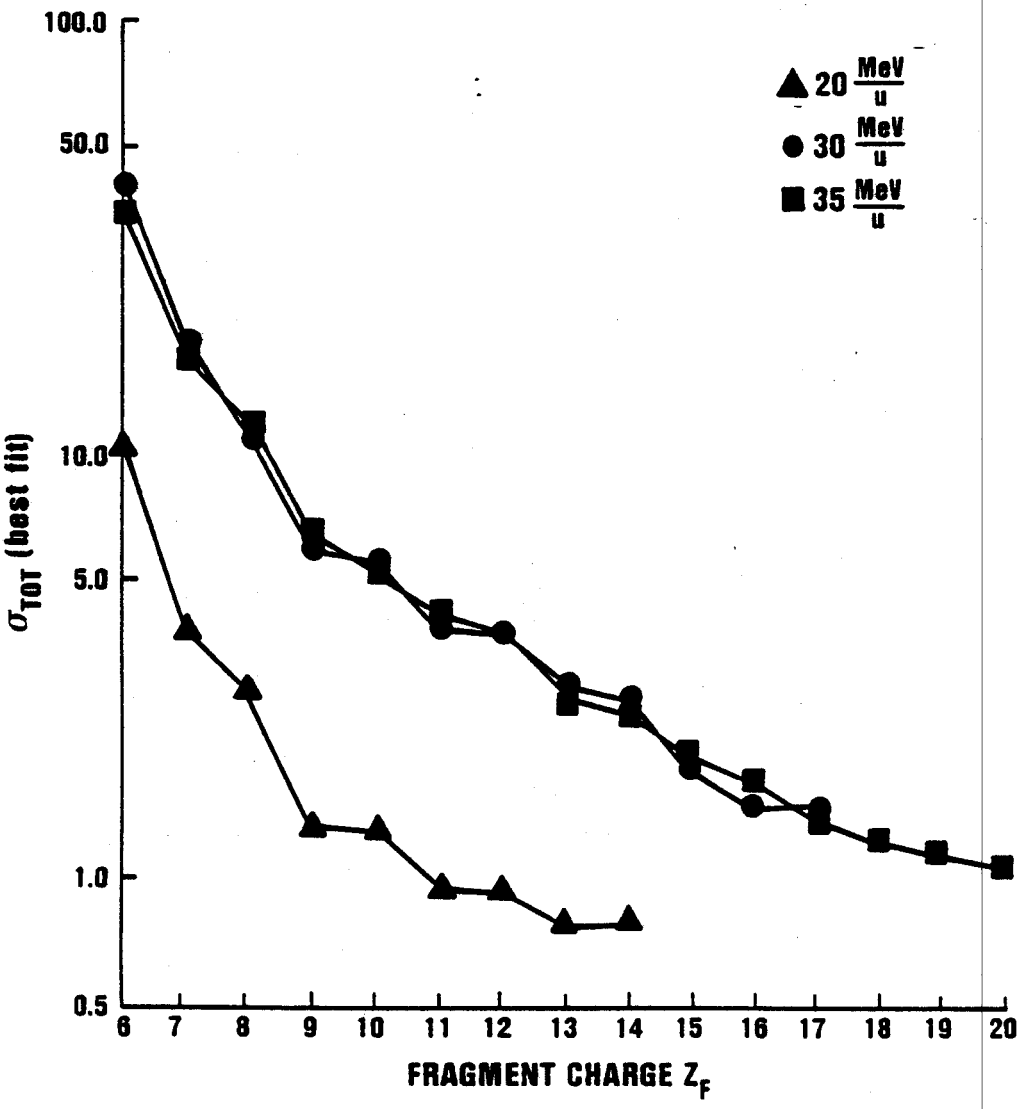

Figure A.3. σ_{TOT} vs. Z_F, the emitted fragment charge, where the cross sections are determined from the best single moving source fits to the data.

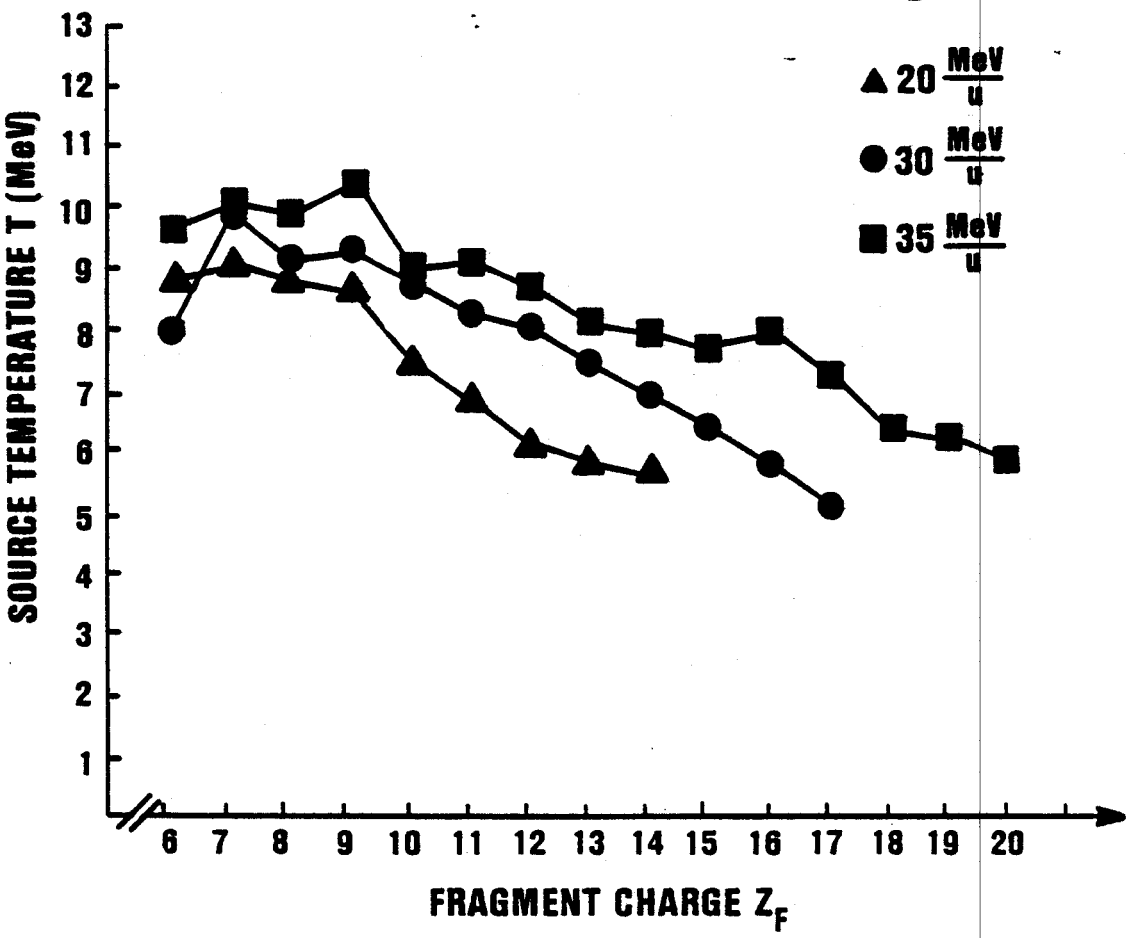

Figure A.4. **Temperature as a function of fragment charge determined from the best single moving source fit to the data.**

(35A MeV), which are commensurate with the results obtained by interpolation over the finite angular range measured (see Figure A.3). Figure A.4 indicates steadily falling temperatures for increasing fragment charge. The velocities were calculated by equating the nonrelativistic momenta of the projectile and the best fit moving source assuming all momentum is imparted to this source. The velocities, thus deduced, are almost constant for a given Z over our range of incident energies (see Figure A.2). However, one can notice a decrease in source velocity as Z increases, perhaps indicating a larger, cooler emitting source.

APPENDIX B

ENERGY SPECTRA

APPENDIX B

ENERGY SPECTRA

The double differential cross sections versus energy for the reaction $^{14}N + ^{nat}Ag$ at incident energies of 20A, 30A, and 35A MeV are presented. Accompanying the data are their best single moving source fits.

The light fragment data from the 20A MeV experiment can be found in Figures B.1 through B.4. Heavy fragment data from this experiment can be found in Figures B.5 through B.8.

The light fragment data from the 30A MeV experiment can be found in Figures B.9 through B.11. Heavy fragment data from this experiment can be found in Figures B.12 through B.15.

The light fragment data from the 35A MeV experiment can be found in Figures B.16 and B.17. Heavy fragment data from this experiment can be found in Figures B.18 through B.21.

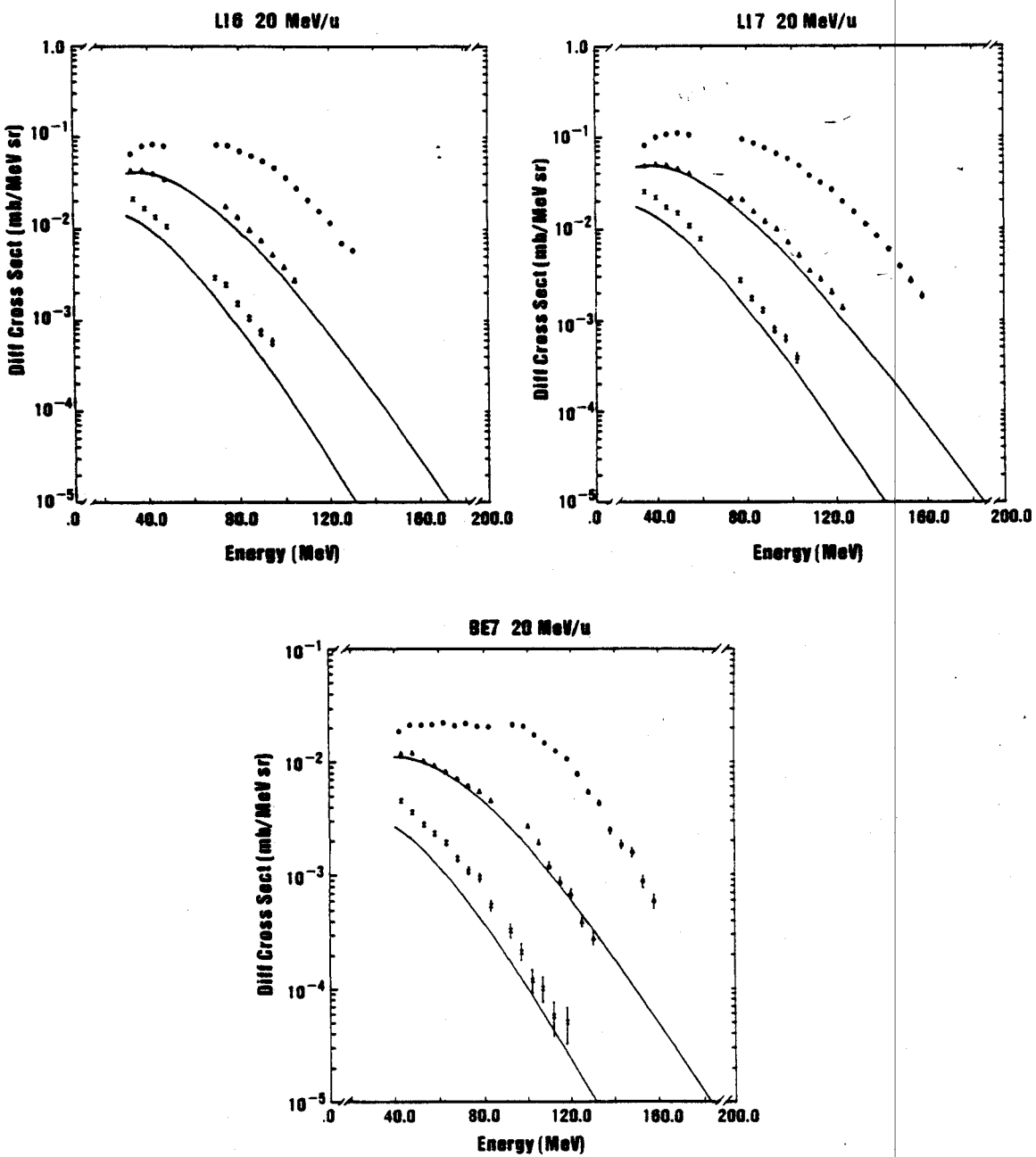

Figure B.1. Double differential cross-sections vs. energy for ^{6}Li, ^{7}Li, and ^{7} Be at laboratory angles of 30°(o), 40°(Δ), and 60°(x). The incident energy was 20 A MeV. Solid lines indicate best moving source fits.

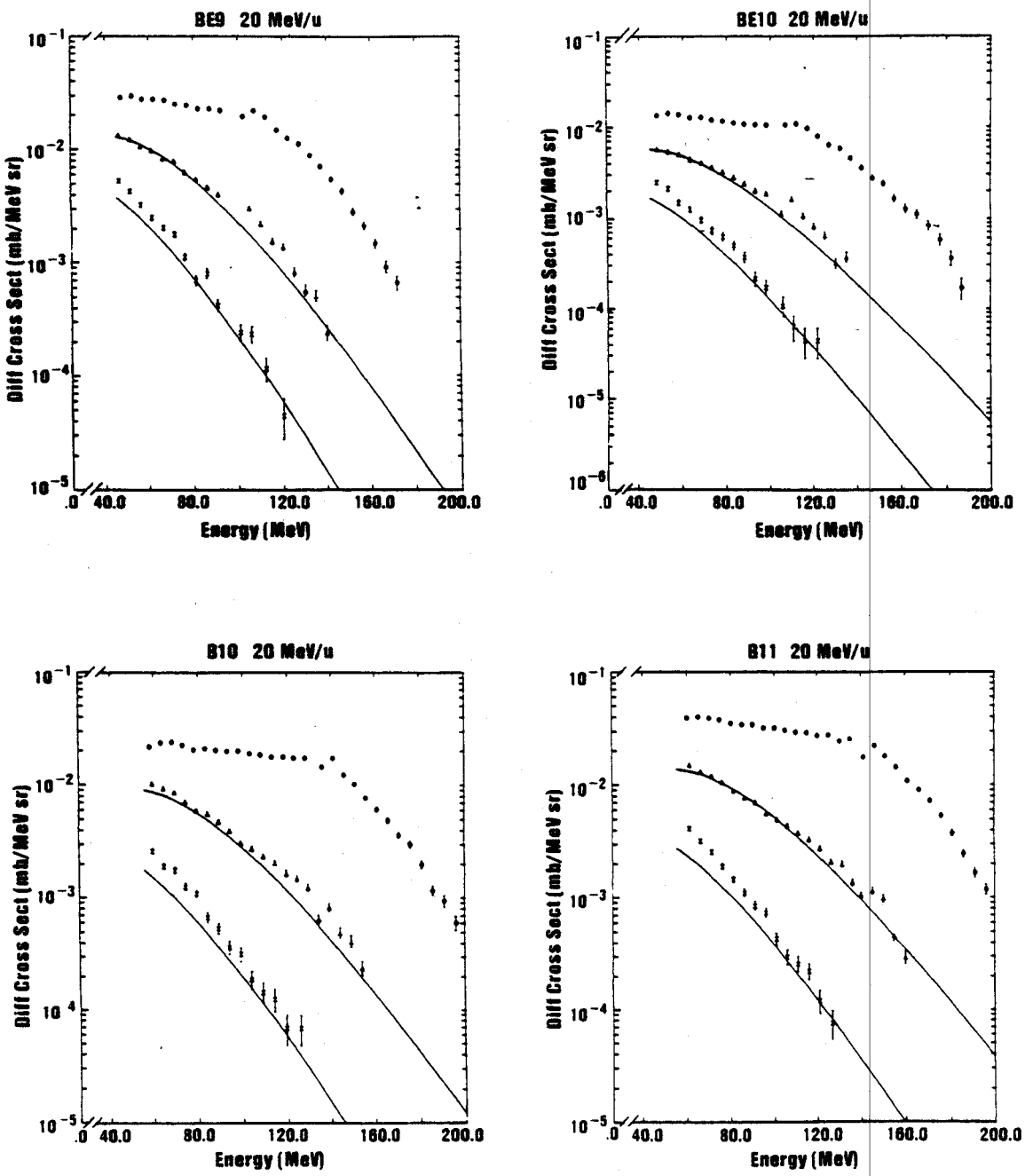

Figure B.2. Double differential cross-sections vs. energy for ^{9}Be, ^{10}Be, ^{10}B, and ^{11}B at laboratory angles of 30°(o), 40°(Δ), and 60°(x). The incident energy was 20 A MeV. Solid lines indicate best moving source fits.

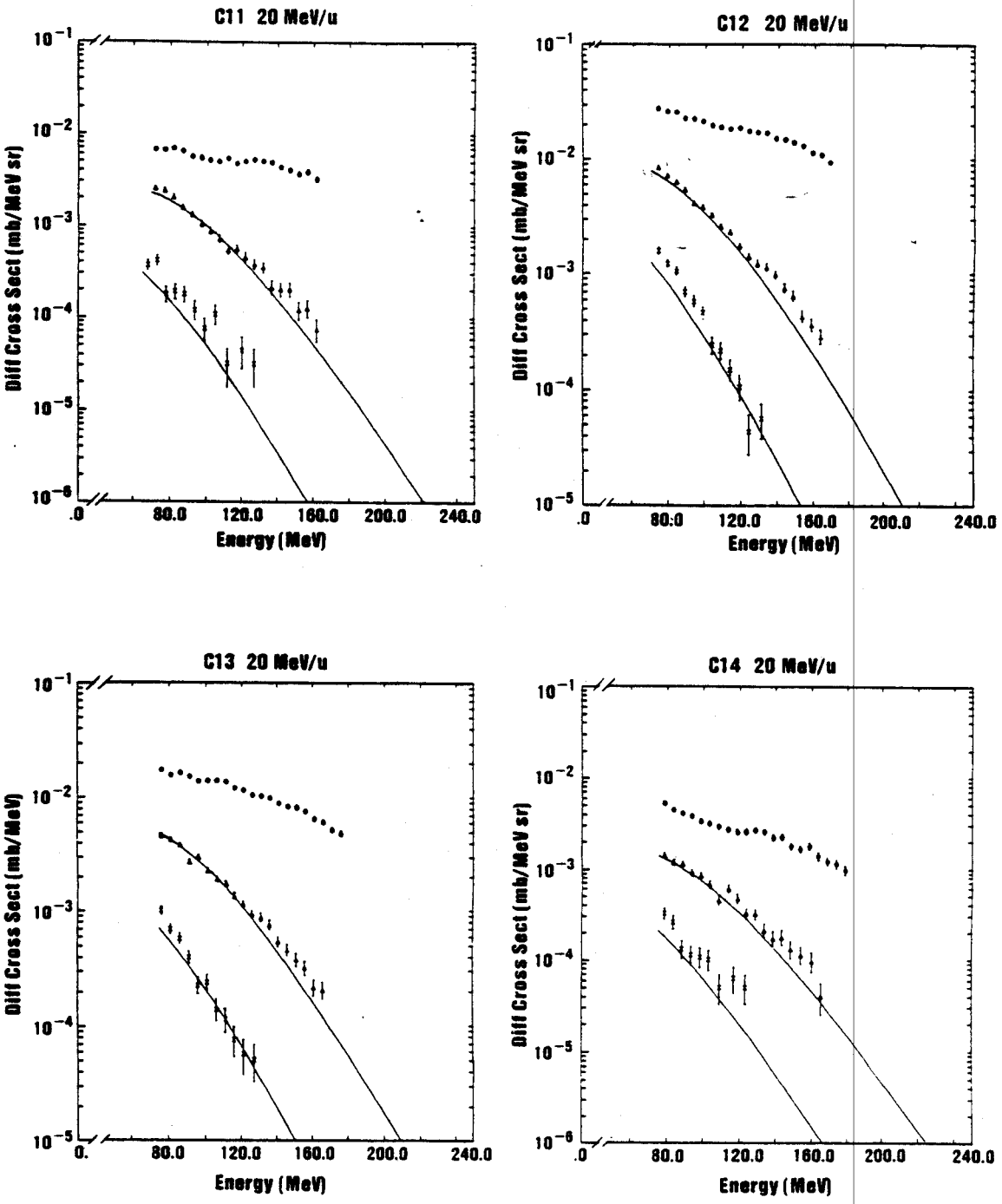

Figure B.3. **Double differential cross-sections vs. energy for ^{11}C, ^{12}C, ^{13}C, and ^{14}C at laboratory angles of 30°(o), 40°(Δ), and 60°(x). The incident energy was 20 A MeV. Solid lines indicate best moving source fits.**

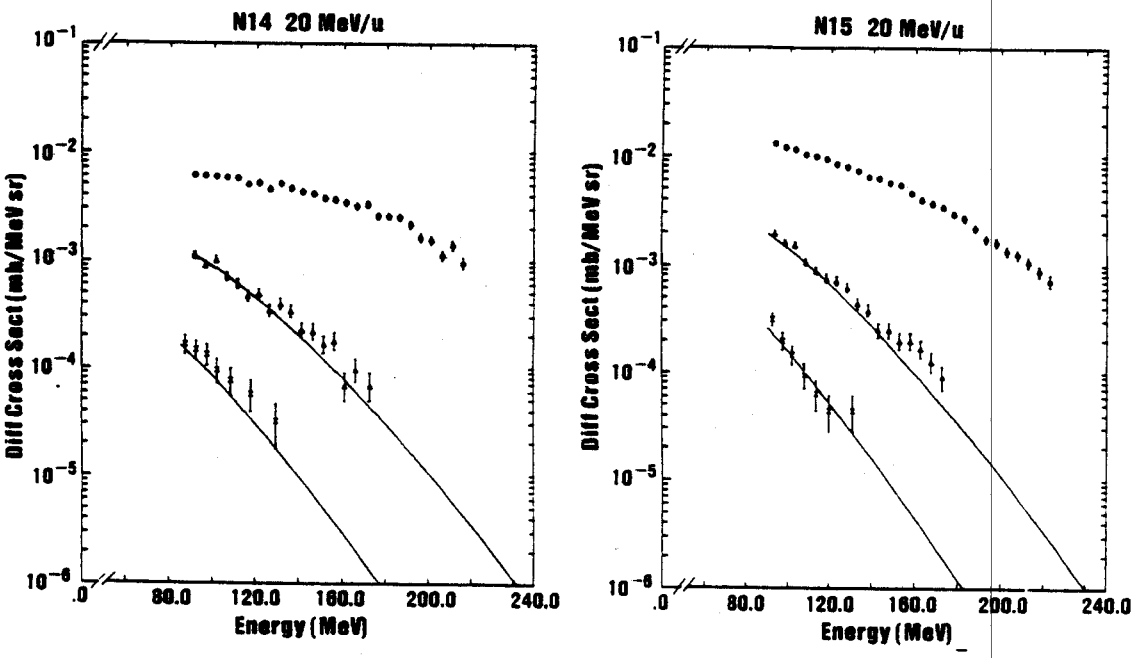

Figure B.4. **Double differential cross-sections vs. energy for ^{14}N and ^{15}N at laboratory angles of 30°(o), 40°(Δ), and 60°(x). The incident energy was 20 A MeV. Solid lines indicate best moving source fits.**

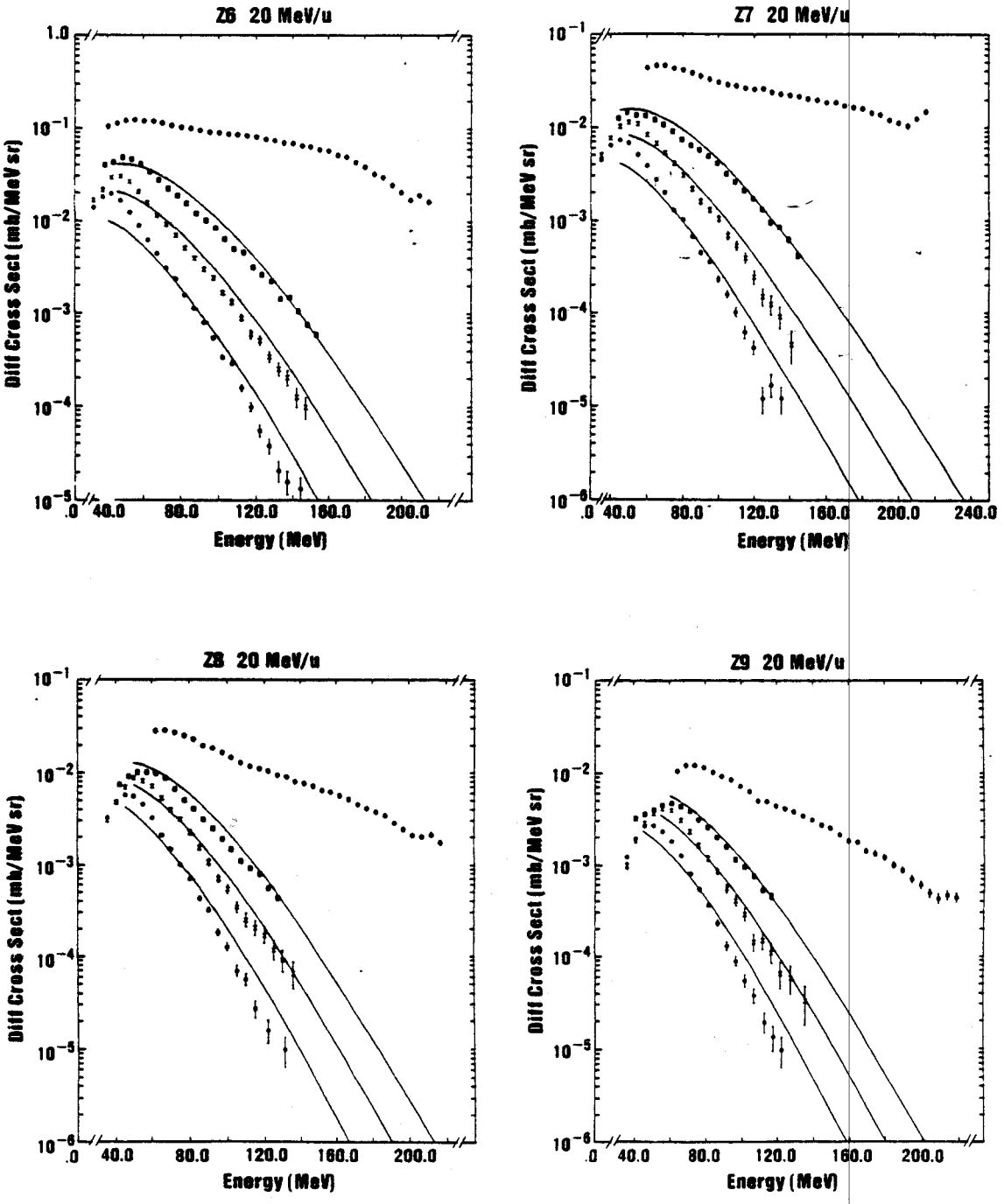

Figure B.5. Double differential cross-sections vs. energy for $6 \leq Z \leq 9$ at laboratory angles of 20°(o), 40°(□), 50°(x), and 60°(+). The incident energy was 20 A MeV. Solid lines indicate best moving source fits.

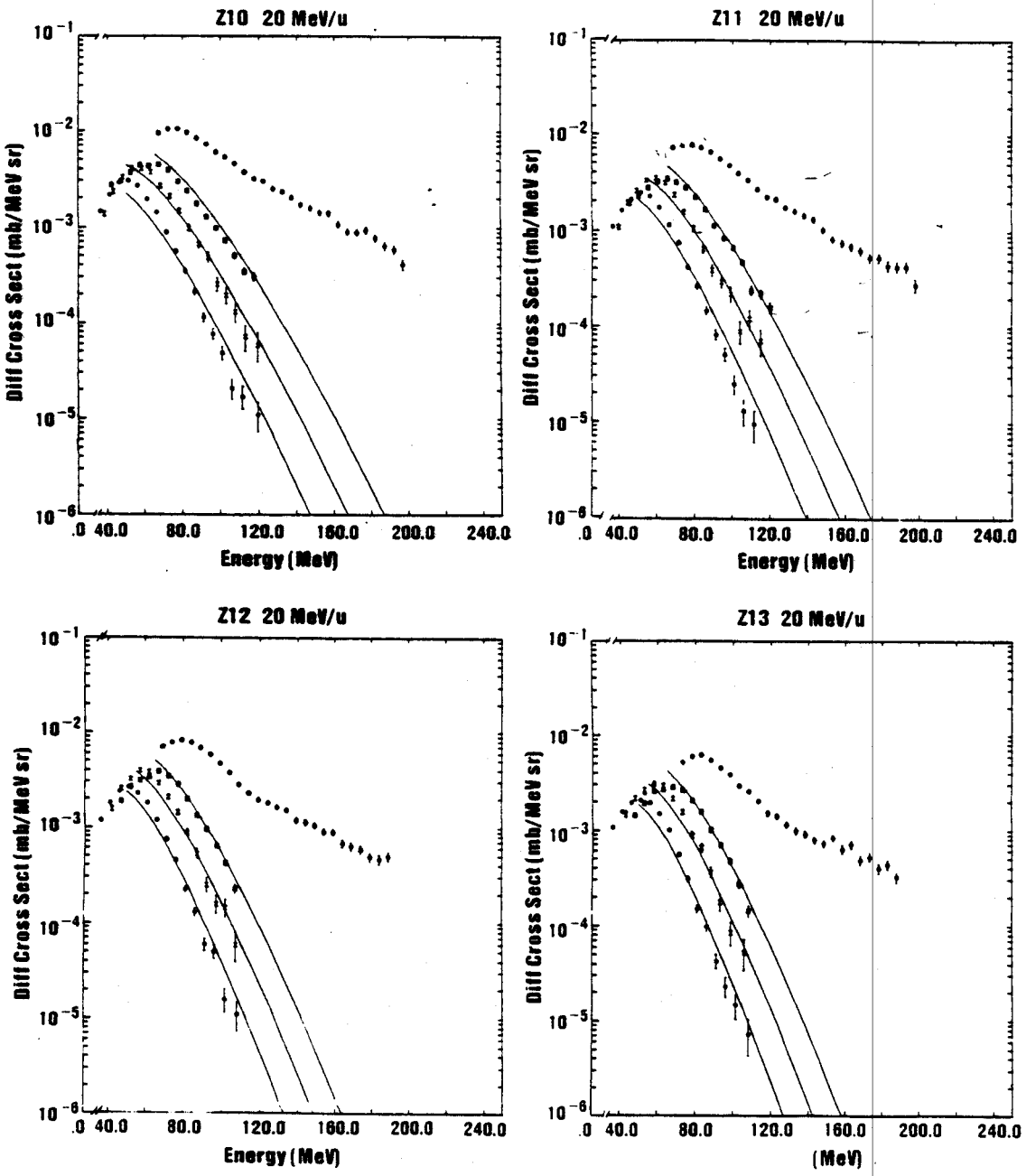

Figure B.6. **Double differential cross-sections vs. energy for $10 \leq Z \leq 13$ at laboratory angles of 20°(o), 40°(□), 50°(x), and 60°(*). The incident energy was 20 A MeV. Solid lines indicate best moving source fits.**

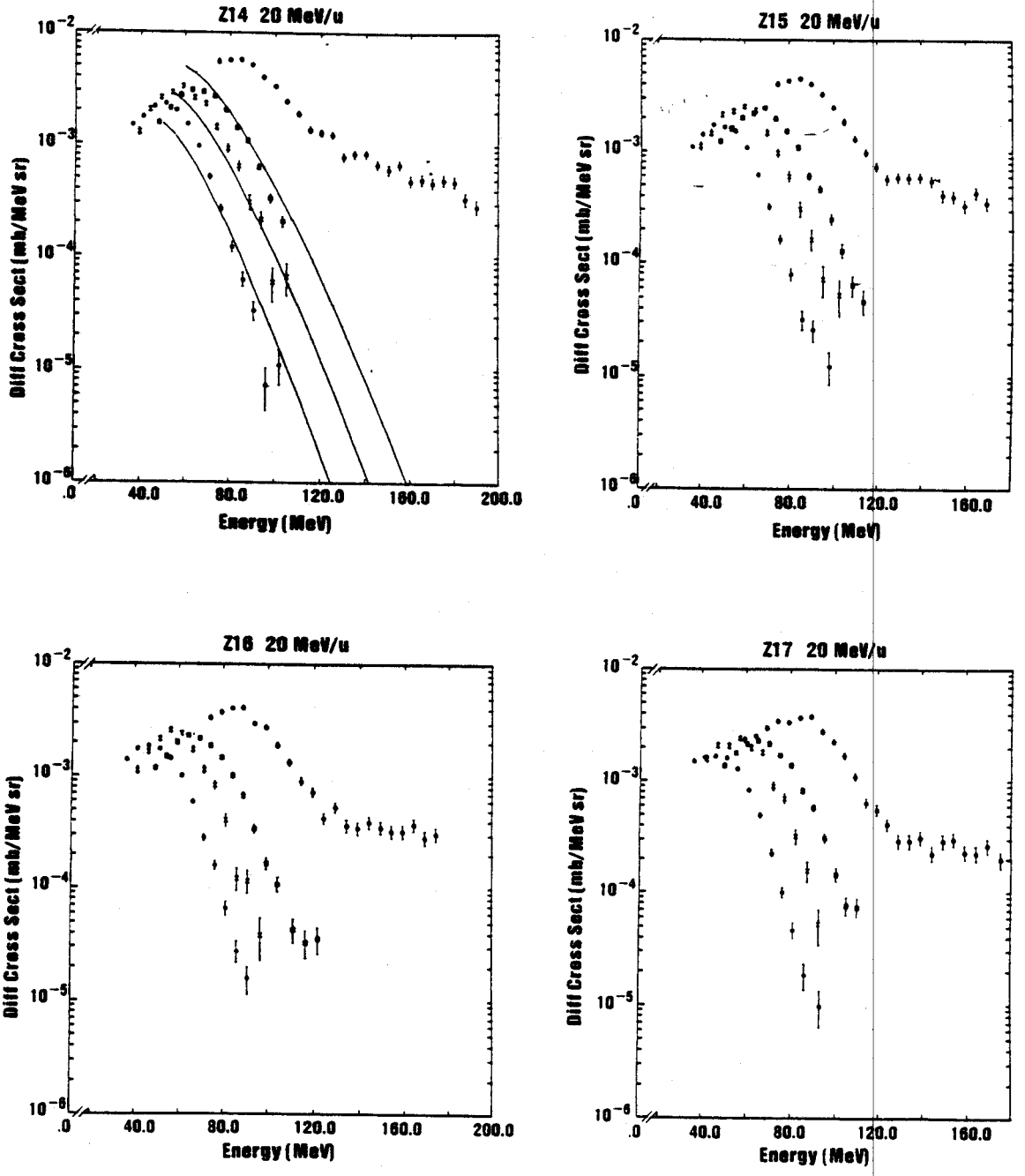

Figure B.7. **Double differential cross-sections vs. energy for $14 \leq Z \leq 17$ at laboratory angles of 20°(o), 40°(□), 50°(x), and 60°(*). The incident energy was 20 A MeV. Solid lines indicate best moving source fits.**

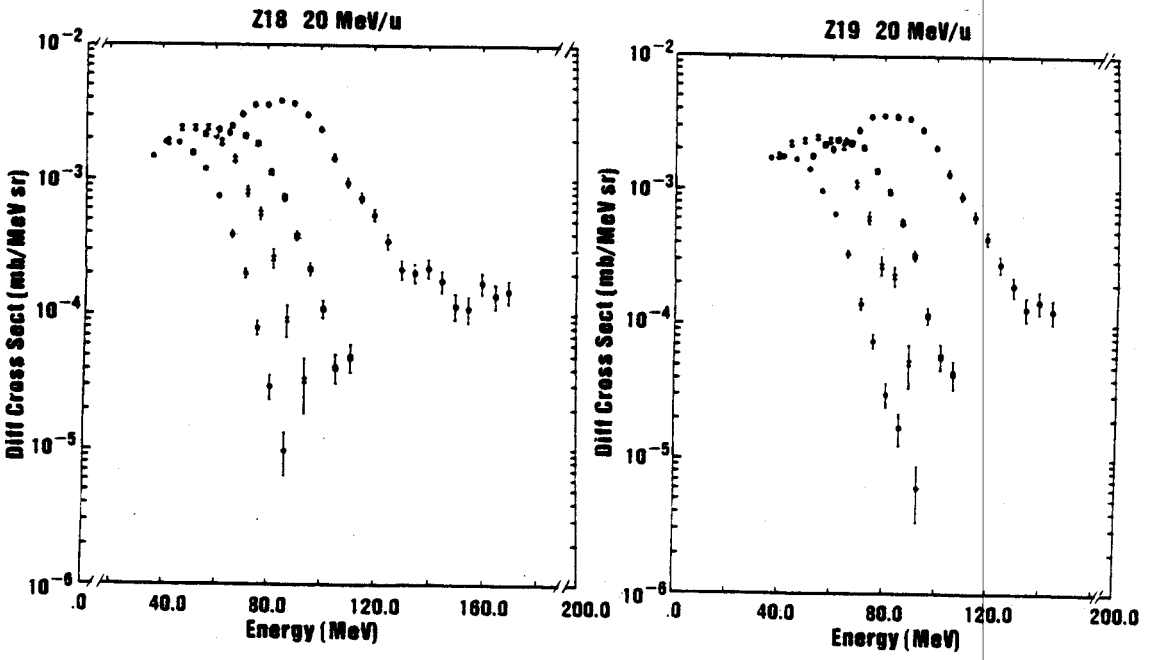

Figure B.8. **Double differential cross-section vs. energy for $18 \leq Z \leq 19$ at laboratory angles of 20°(o), 40°(□), 50°(x), and 60°(*). The incident energy was 20 A MeV.**

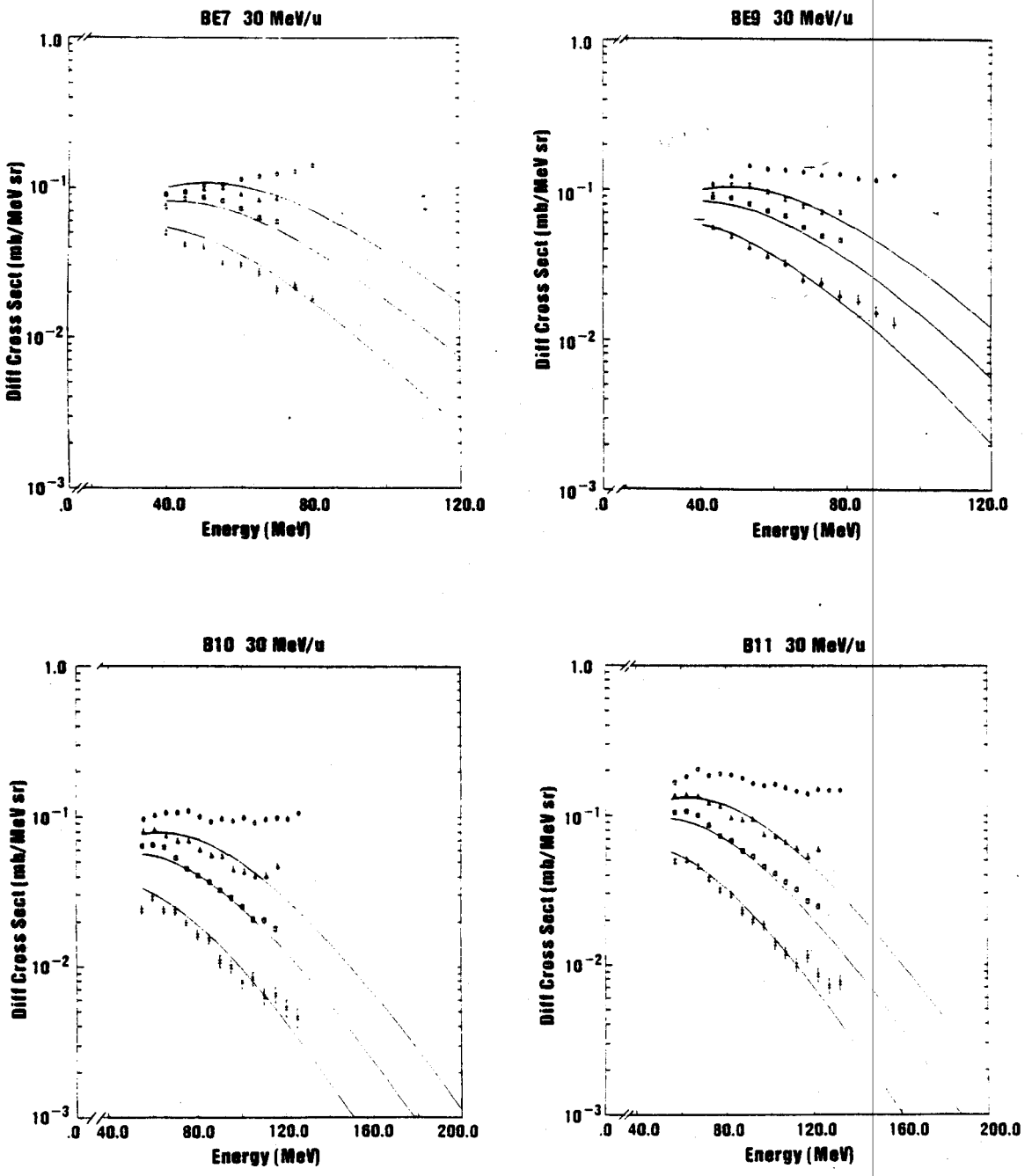

Figure B.9. **Double differential cross-sections vs. energy for ^{7}Be, ^{9}Be, ^{10}B, and ^{11}B at laboratory angles of 20°(o), 30°(Δ), 40°(□), and 50°(x). The incident energy was 30 A MeV. Solid lines indicate best moving source fits.**

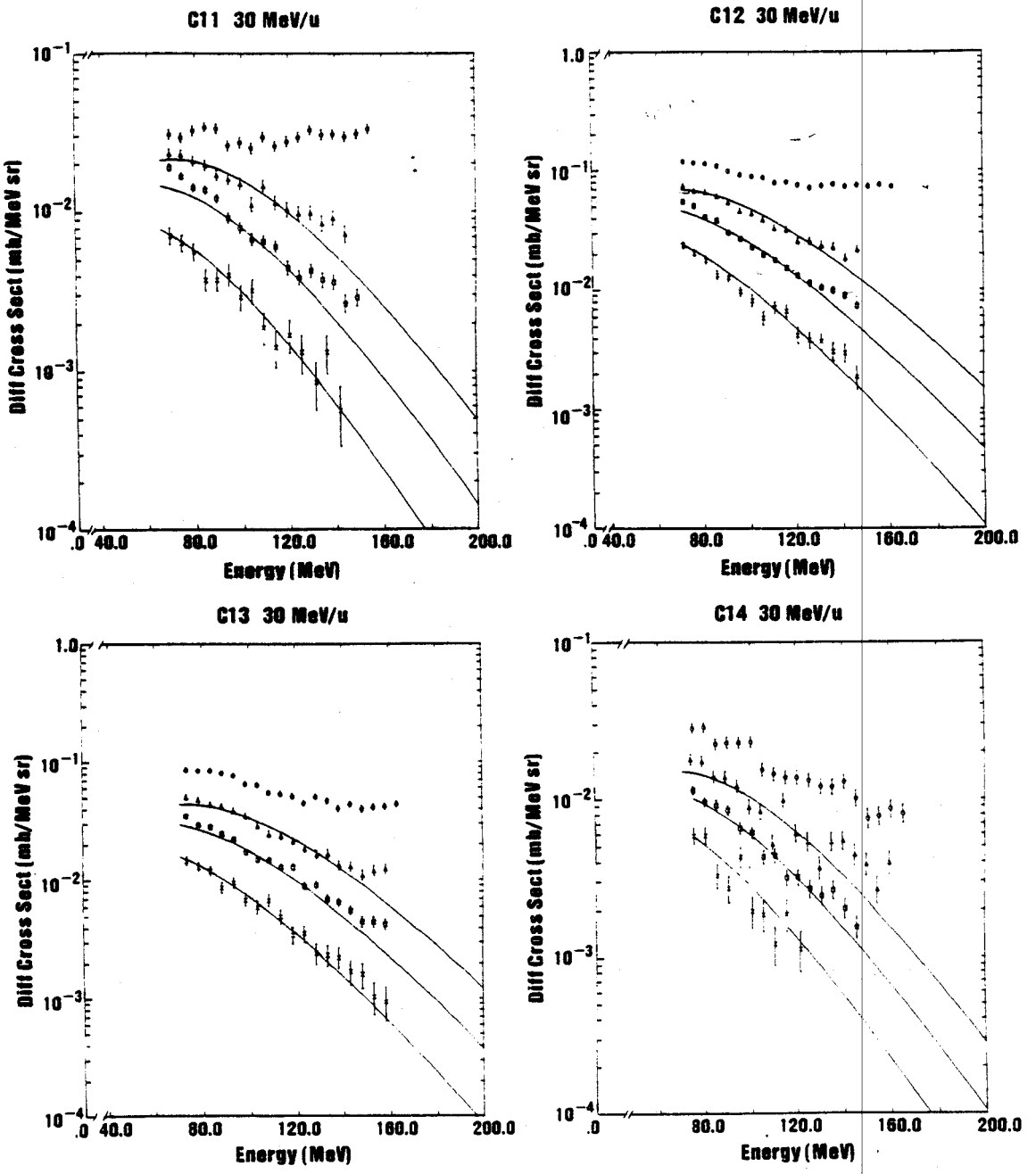

Figure B.10. Double differential cross-sections vs. energy for ^{11}C, ^{12}C, ^{13}C, and ^{14}C at laboratory angles of 20°(o), 30°(△), 40°(□), and 50°(x). The incident energy was 30 A MeV. Solid lines indicate best moving source fits.

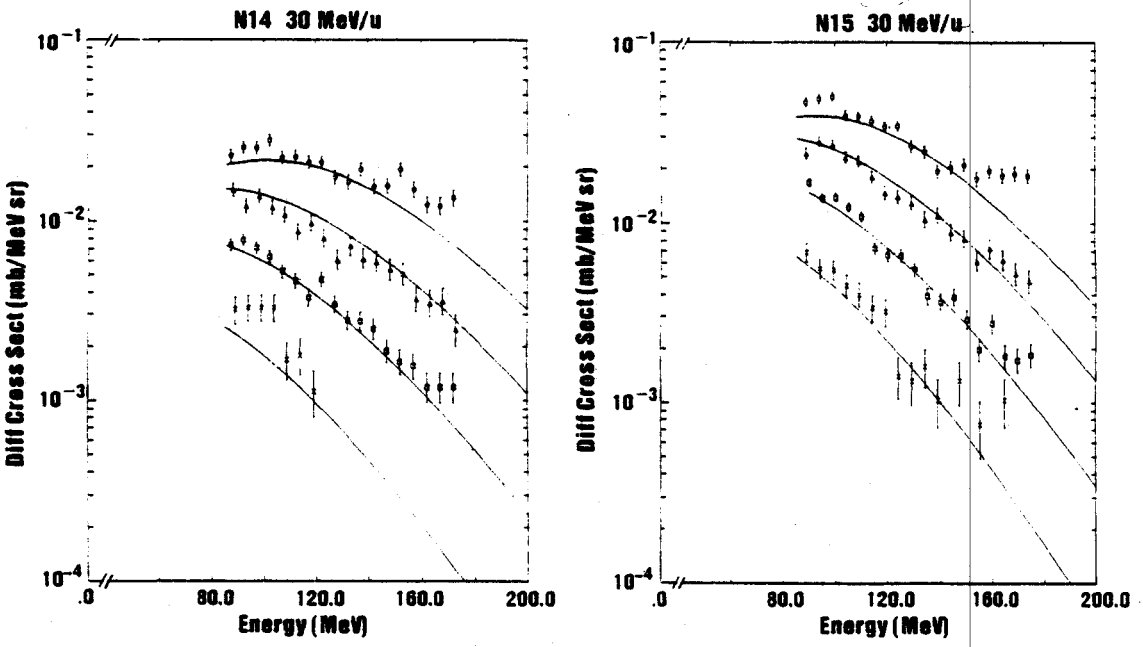

Figure B.11. **Double differential cross-sections vs. energy for ^{14}N and ^{15}N at laboratory angles of 20°(o), 30°(Δ), 40°(□), and 50°(x). The incident energy was 30 A MeV. Solid lines indicate best moving source fits.**

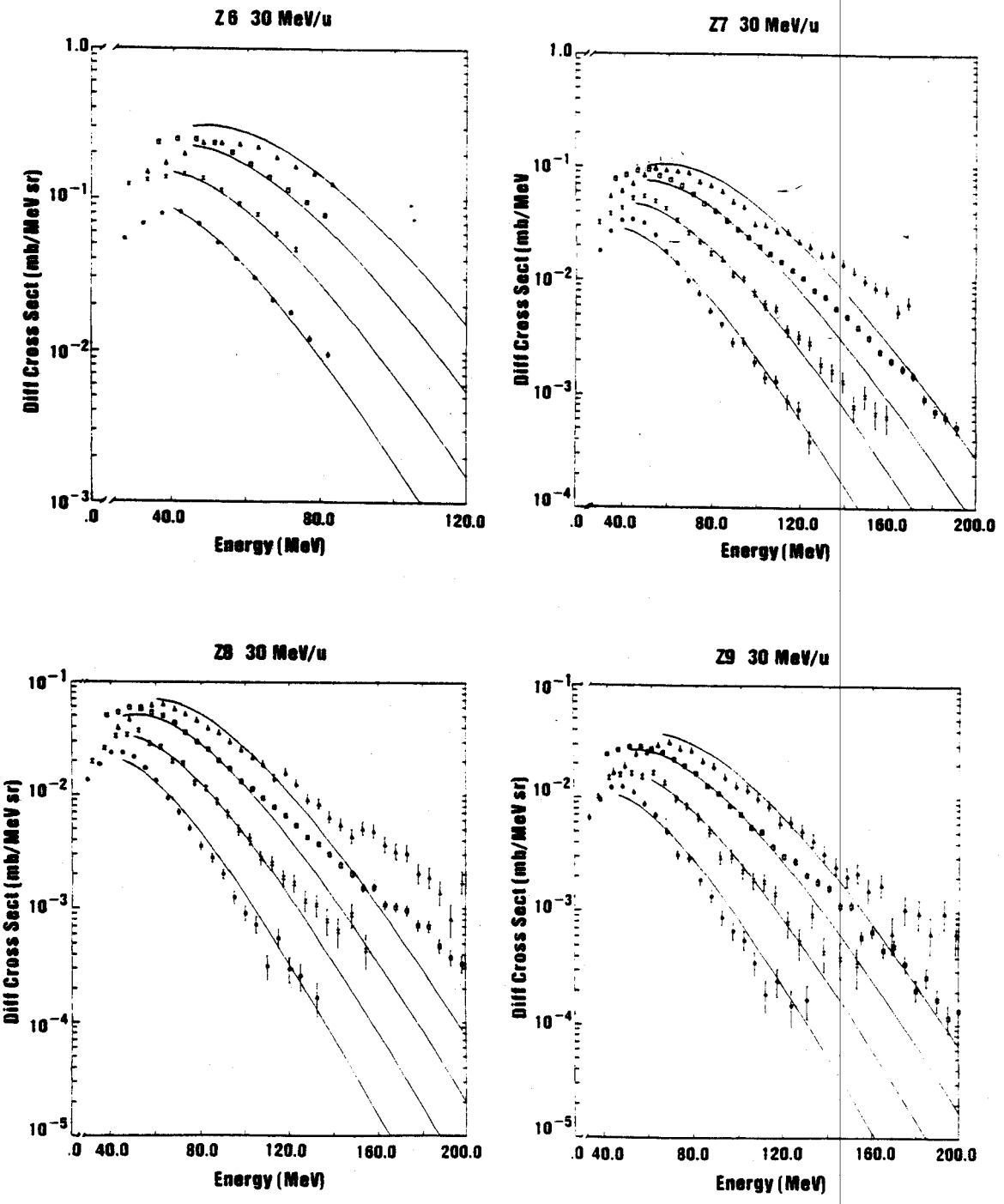

Figure B.12. **Double differential cross-section vs. energy for 6≤Z≤9 at laboratory angles of 30°(△), 40°(□), 50°(x), and 60°(+). The incident energy was 30 A MeV. Solid lines indicated best moving source fits.**

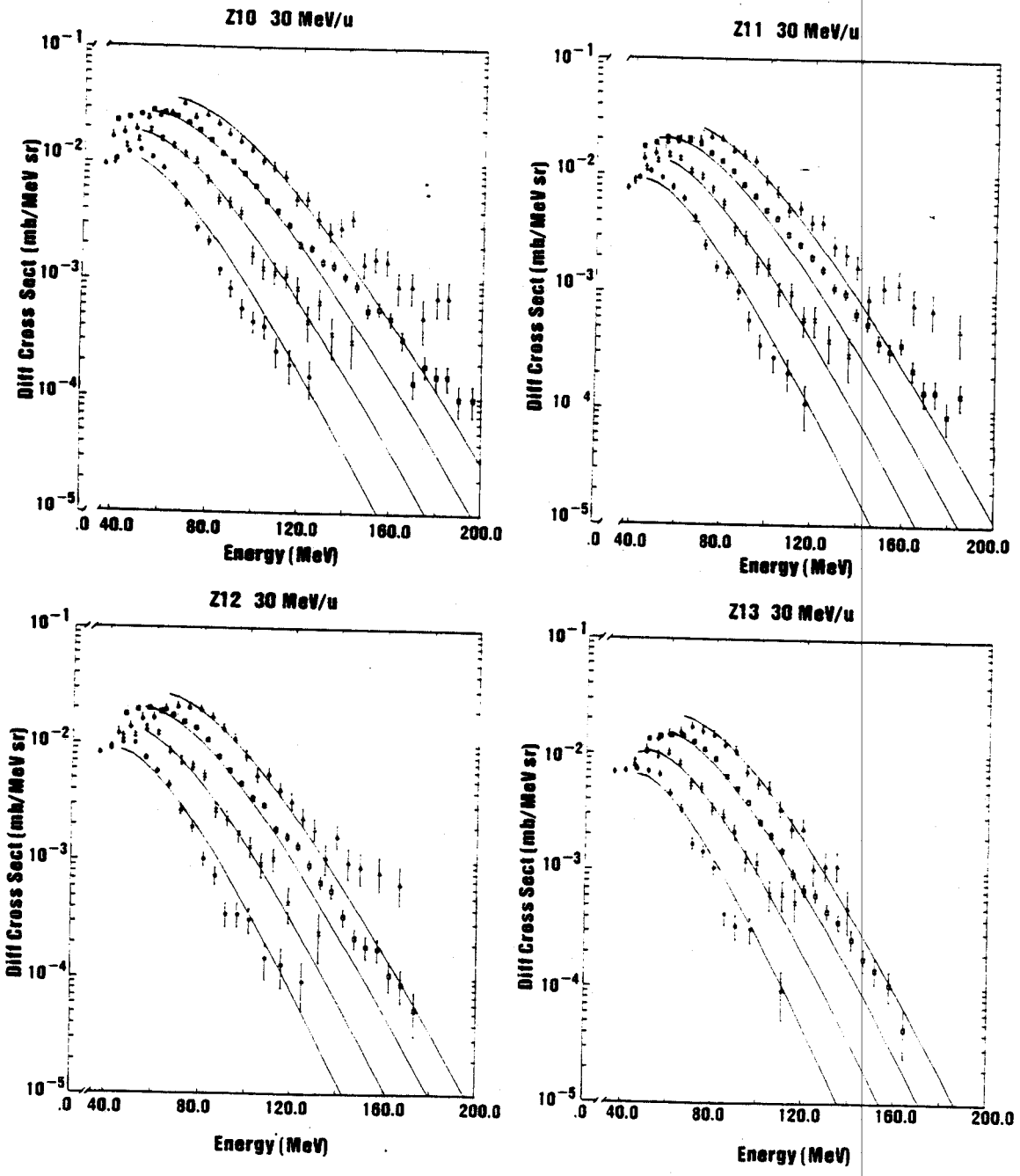

Figure B.13. **Double differential cross-sections vs. energy for $10 \leq Z \leq 13$ at laboratory angles of 30°(△), 40°(□), 50°(x), and 60°(+). The incident energy was 30 A MeV. Solid lines indicate best moving source fits.**

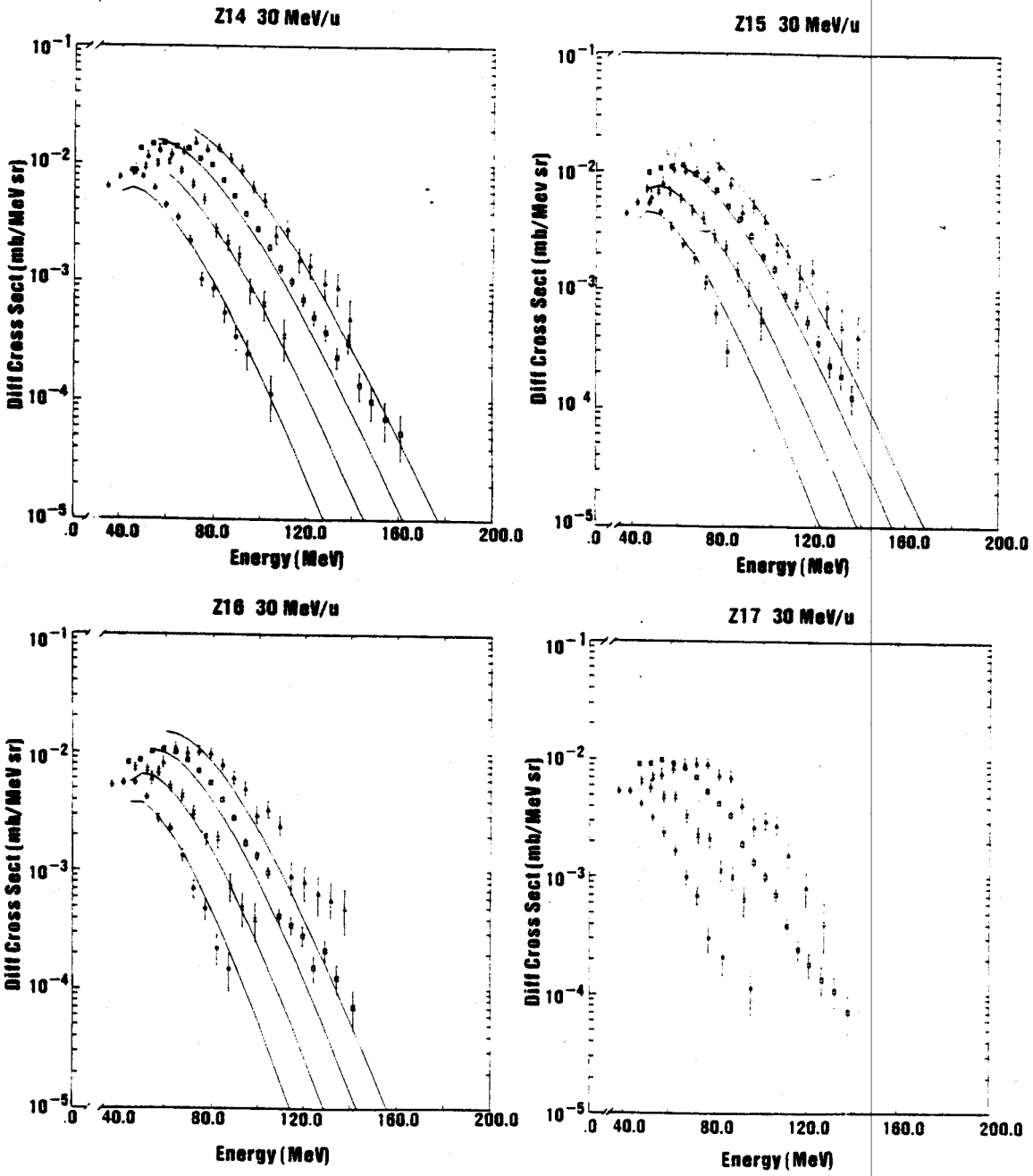

Figure B.14. **Double differential cross-sections vs. energy for $14 \leq Z \leq 17$ at laboratory angles of 30°(Δ), 40°(□), 50°(x), and 60°(*). The incident energy was 30 A MeV. Solid lines indicate best moving source fits.**

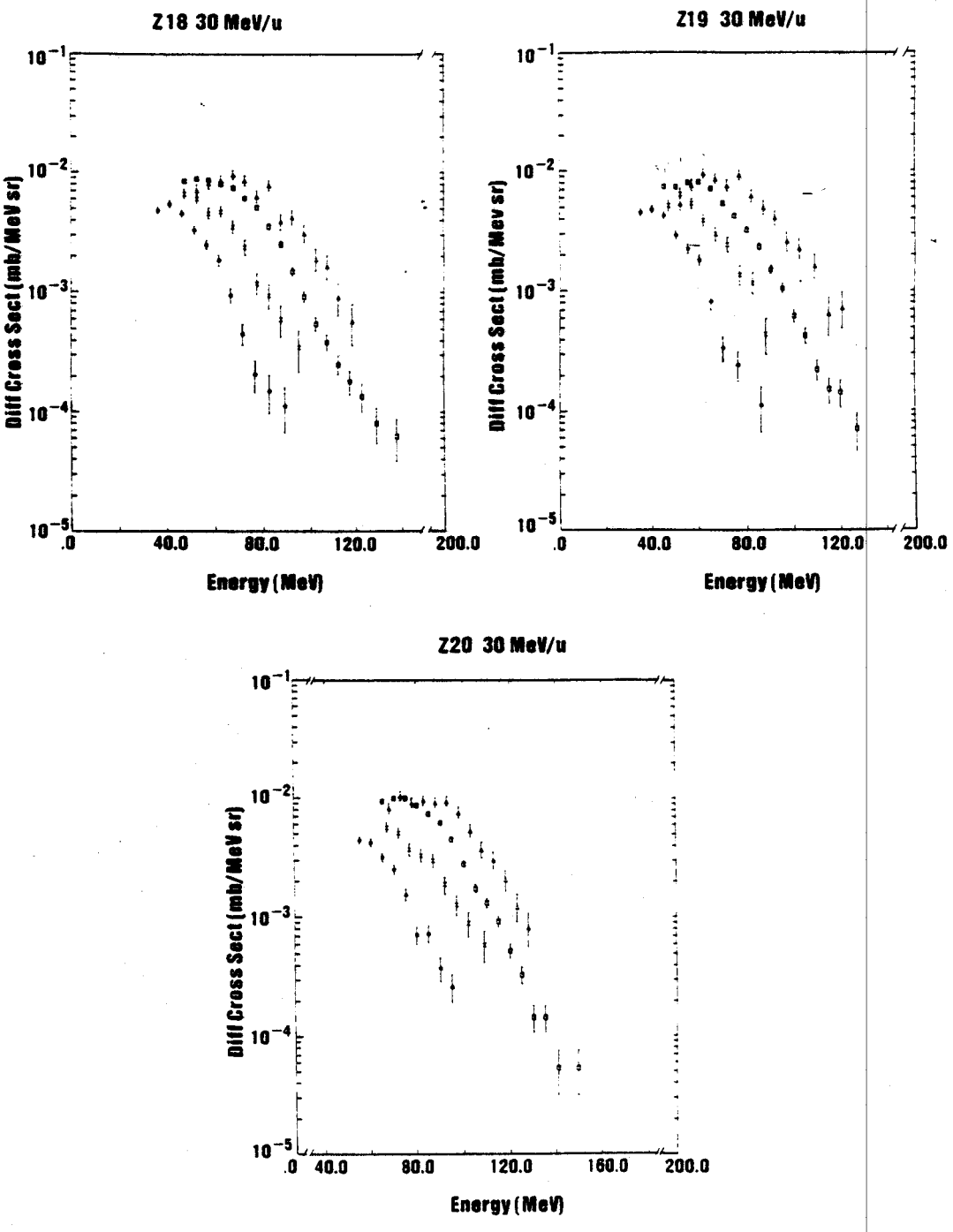

Figure B.15. Double differential cross-sections vs. energy for $18 \leq Z \leq 20$ at laboratory angles of 30°(△), 40°(□), 50°(x), and 60°(*). The incident energy was 30 A MeV.

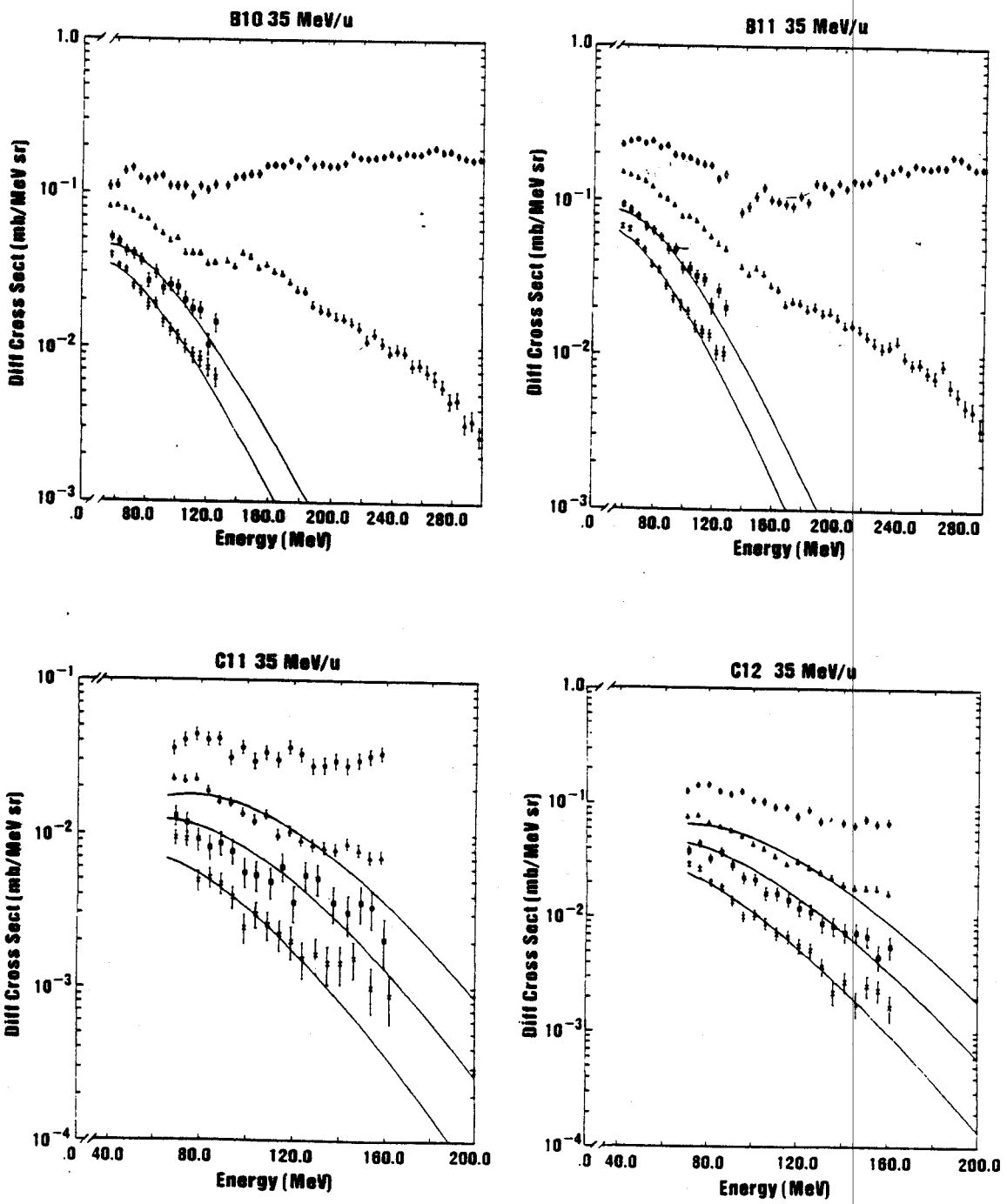

Figure B16. **Double differential cross-sections vs. energy for ^{10}B, ^{11}B, ^{11}C, and ^{12}C at laboratory angles of 20°(o), 30°(Δ), 40°(□), and 50°(x). The incident energy was 35 A MeV. Solid lines indicate best moving source fits.**

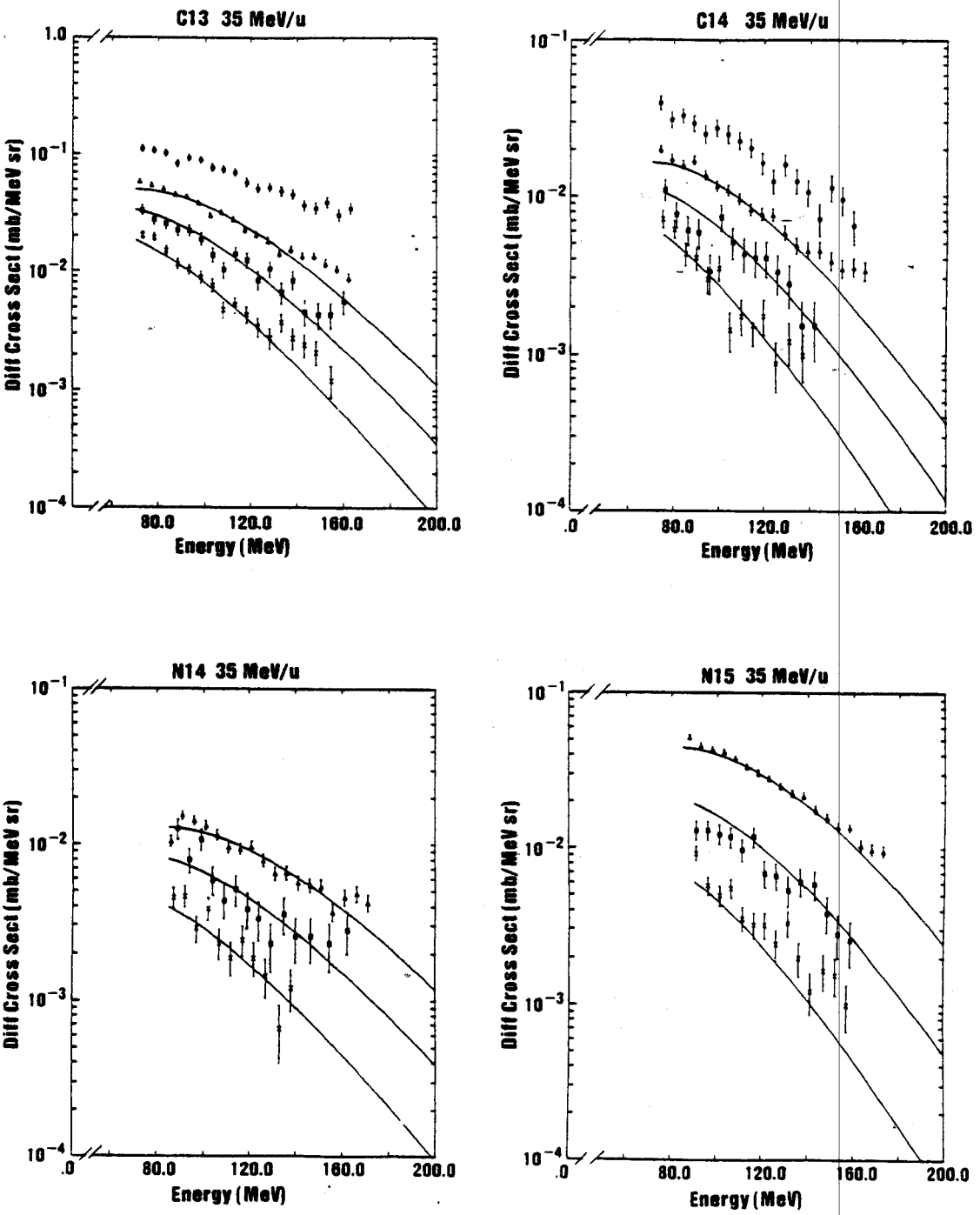

Figure B.17. Double differential cross-sections vs. energy for ^{13}C, ^{14}C, ^{14}N, and ^{15}N at laboratory angles of 20°(o), 30°(Δ), 40°(□), and 50°(x). The incident energy was 35 A MeV. Solid lines indicate best moving source fits.

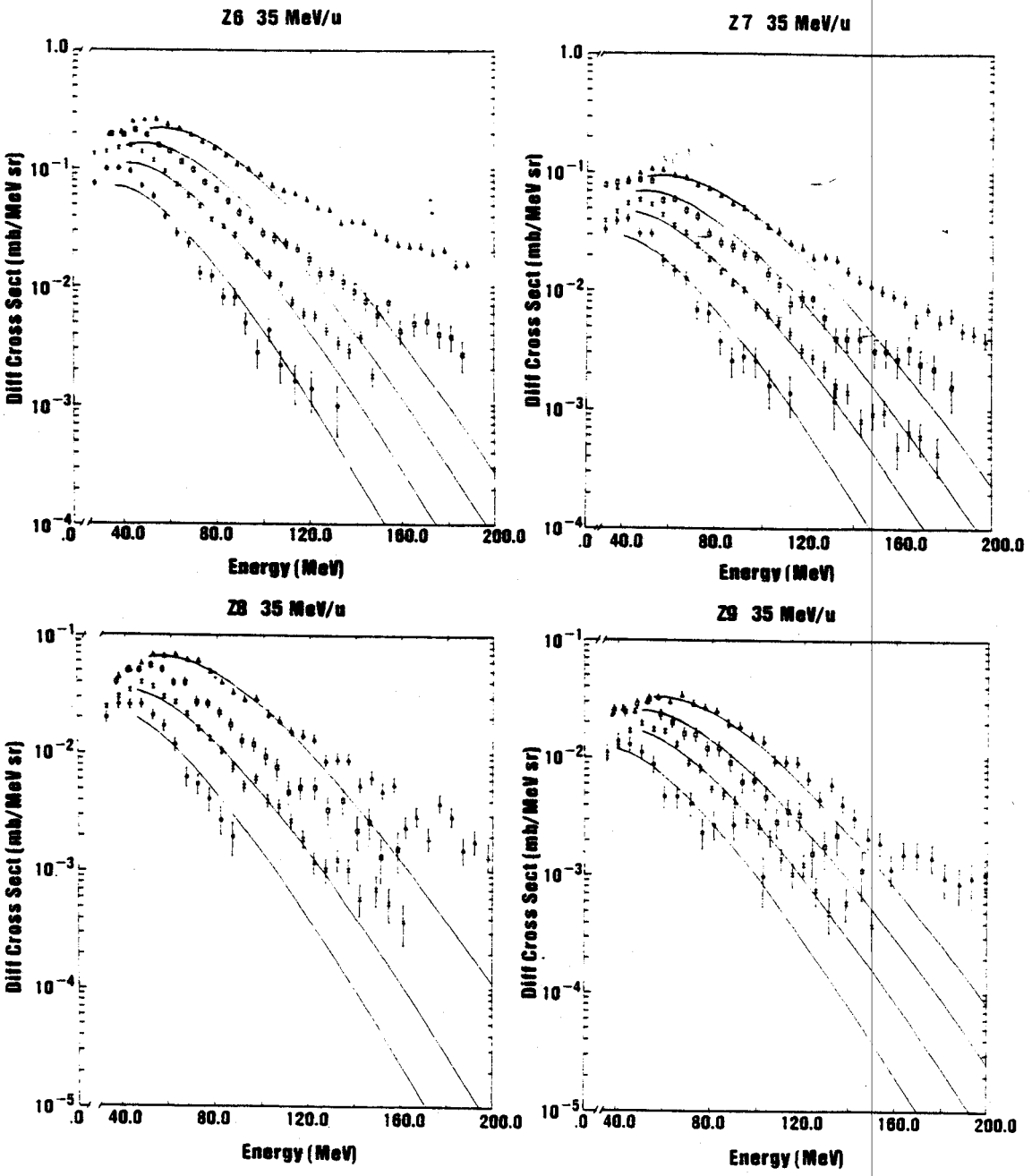

Figure B.18. **Double differential cross-sections vs. energy for $6 \leq Z \leq 9$ at laboratory angles of 30°(Δ), 40°(□), 50°(x), and 60°(∗). The incident energy was 35 A MeV. Solid lines indicated best moving source fits.**

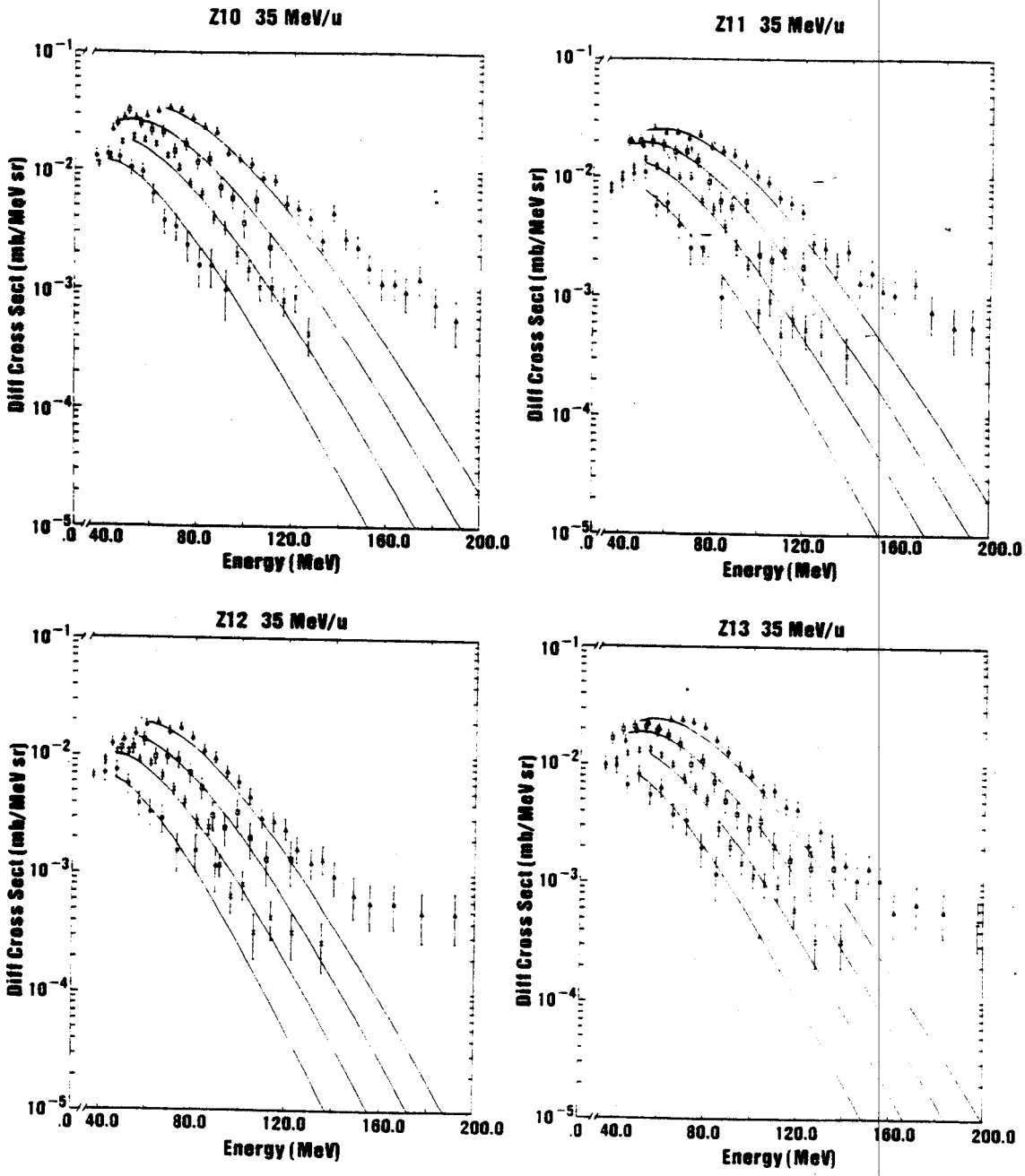

Figure B.19. **Double differential cross-sections vs. energy for $10 \leq Z \leq 13$ at laboratory angles of 30°(△), 40°(□), 50°(x), and 60°(⋆). The incident energy was 35 A Mev. Solid lines indicate best moving source fits.**

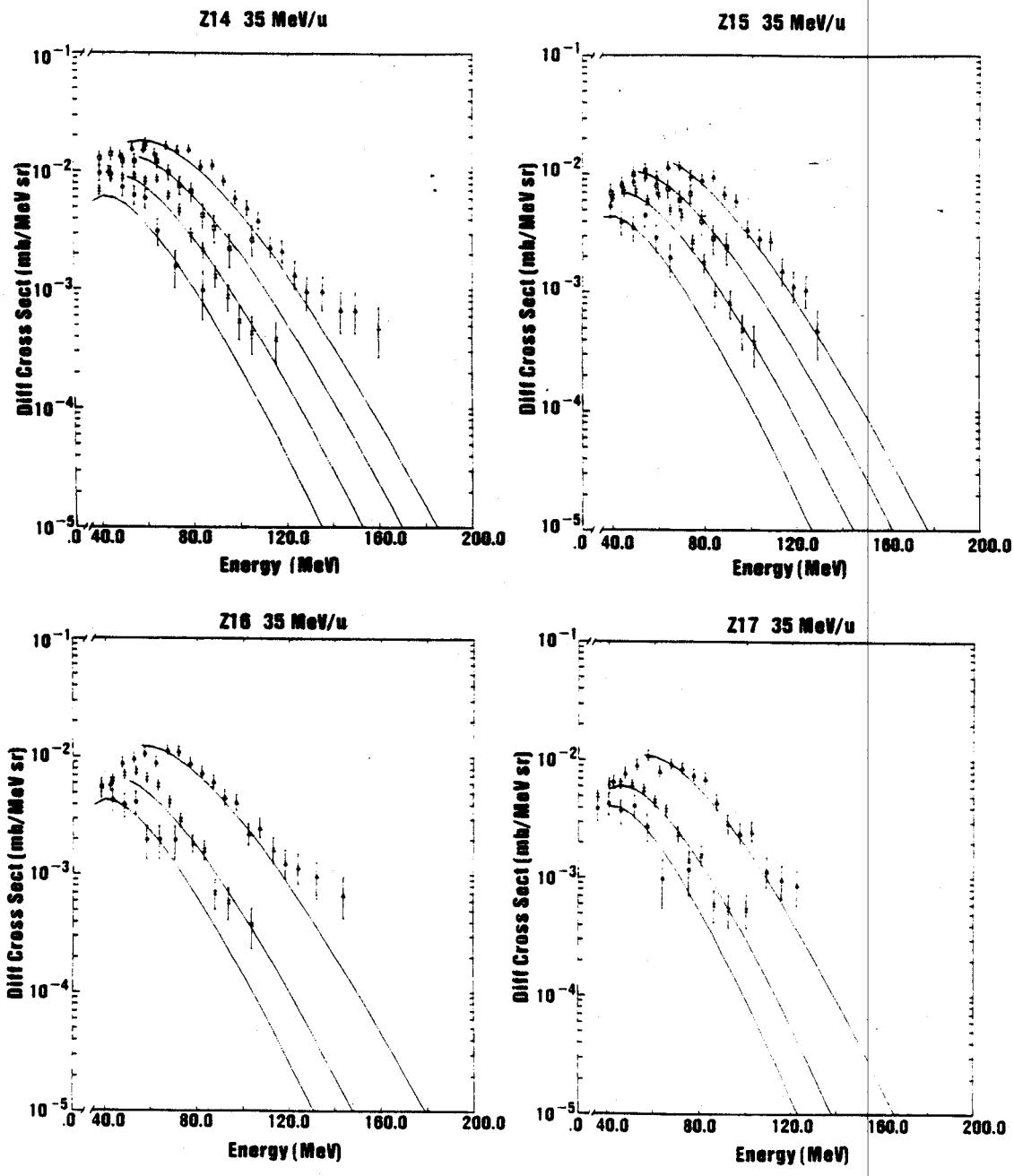

Figure B.20. **Double differential cross-sections vs. energy for $14 \leq Z \leq 17$ at laboratory angles of 30°(Δ), 40°(□), 50°(x), and 60°(*). The incident energy was 35 A Mev. Solid lines indicate best moving source fits.**

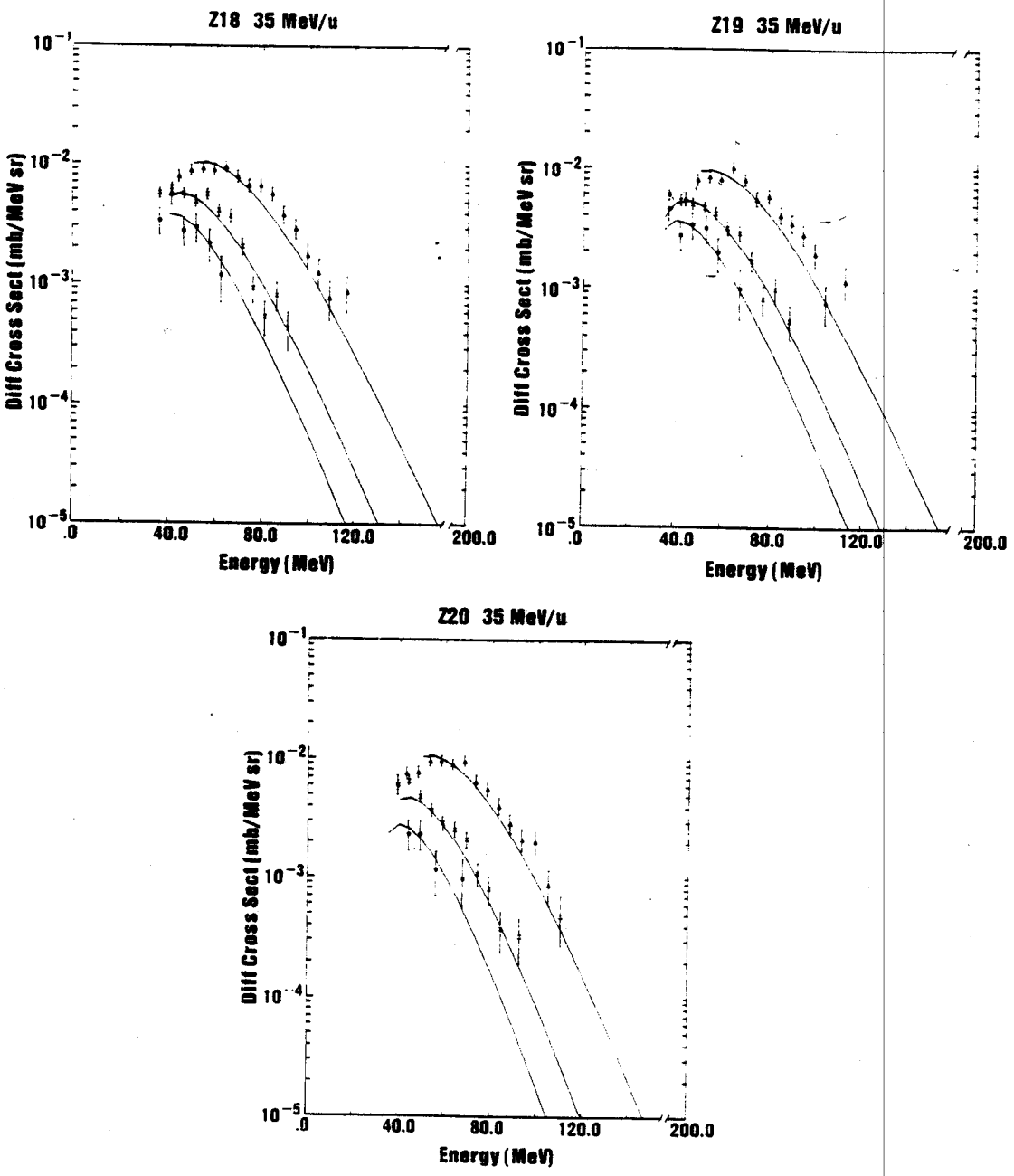

Figure B.21. Double cross-sections vs. energy for $18 \leq Z \leq 20$ at laboratory angles of 30° (Δ), 50° (x), and 60° (*). The incident energy was 35 A MeV. Solid lines indicate best moving source fits.

REFERENCES

REFERENCES

AIC 84a J. Aichelin and J. Hüfner, Phys. Lett. 136B (1984) 15.

AIC 84b J. Aichelin, J. Hüfner, and R. Ibarra, Phys. Rev. C30 (1984) 107.

BAR 75 J. Barrette, P. Braun-Munzinger, and C.K. Gelbke, Nucl. Instr. and Methods 126 (1975) 181.

BAU 85 W. Bauer, D.R. Dean, U. Mosel, and U. Post, Phys. Lett. 150B (1985) 53.

BEN 69 J. Benecke, T.T. Chou, C.N. Yang, and E. Yen, Phys. Rev. 188 (1969) 2159.

BER 81 G.F. Bertsch and J. Cugnon, Phys. Rev. C24 (1981) 2514.

BER 83 G.F. Bertsch and P.J. Siemens, Phys. Lett. 126B (1983) 9.

BLA 74 J.S. Blakemore, Solid State Physics (W.B. Saunders and Co., Philadelphia, 1974) 190.

BOA 84a D. Boal, Phys. Rev. C30 (1984) 119.

BOA 84b D. Boal, MSU Preprint MSUCL-467 (1984).

BOH 70 H. Bohning, Proc. International Conference on Nuclear Reactions Induced by Heavy Ions (North Holland, Amsterdam, 1970) 633.

BON 84 P. Bonche, S. Levit, and D. Vautherin, Nucl. Phys. A427 (1984) 278; and references therein.

CAM 85 X. Campi and J. Desbois, Contribution to Workshop: 7th Heavy Ion Study, GSI, Darmstadt (Oct. 8-12, 1984) Preprint IPNO/TH 85-5.

CHI 83 C.B. Chitwood, D.J. Fields, C.K. Gelbke, W.G. Lynch, A.D. Panagiotou, M.B. Tsang, H. Utsunomiya, and W.A. Friedman, Phys. Lett. 131B (1983) 289.

CHI 85 C.B. Chitwood, C.K. Gelbke, J. Pochodzalla, Z. Chen, D.J. Fields, W.G. Lynch, R. Morse, M.B. Tsang, D.H. Boal, and J.C. Shillcock, MSU Preprint MSUCL-543 (1985).

CUG 84a J. Cugnon, Cargese Summer School Lectures (Sept. 1984).

CUG 84b J. Cugnon, Phys. Lett. 135B (1984) 374.

CUR 82a M.W. Curtin, H. Toki, and D.K. Scott, MSU Preprint MSUCL-373 (1982).

CUR 82b M.W. Curtin, H. Toki, and D.K. Scott, Cyclotron Annual Report, Michigan State University (1982-1983) 46.

CUR 82c M.W. Curtin and J.S. Counseller, Cyclotron Annual Report, Michigan State University(1982-1983) 99.

CUR 83a M.W. Curtin, H. Toki, and D.K. Scott, Phys. Lett. 123B (1983) 289.

CUR 83b M.W. Curtin, H. Toki, and D.K. Scott, MSU Preprint MSUCL-426 (1983).

DAN 79 P. Danielewicz, Nucl. Phys. A314 (1979) 465.

DIG 80 N.J. DiGiacomo, R.M. de Vries, and J.C. Peng, Phys. Rev. Lett. 45 (1980) 527.

FIE 84 D.J. Fields, W.G. Lynch, C.B. Chitwood, C.K. Gelbke, M.B. Tsang, H. Utsunomiya, and J. Aichelin, Phys. Rev. C30 (1984) 1912.

FIN 82 J.E. Finn, S. Agarwal, A. Bujak, J. Chuang, L.J. Gutay, A.S. Hirsch, R.W. Minich, N.T. Porile, R.P. Scharenberg, B.C. Stringfellow, and F. Turkot, Phys. Rev. Lett. 49 (1982) 1321.

FIS 67 M.E. Fisher, Physics 3 (1967) 255.

FRI 81 B. Friedman and V.R. Pandharipande, Nucl. Phys. A261 (1981) 502.

FRI 83 W.A. Friedman and W.G. Lynch, Phys. Rev. C28 (1983) 16.

GEL 85 C.K. Gelbke and W.G. Lynch, private communication.

GOO 83 A.L. Goodman, J.I. Kapusta, and A.Z. Mekjian, LBL Preprint LBL-16471 (1983).

GOS 77 J. Gosset, H.H. Gutbrod, W.G. Meyer, A.M. Poskanzer, A. Sandoval, R. Stock, and G.D. Westfall, Phys. Rev. C16 (1977) 629.

GRE 80 R.E.L. Green and R.G. Korteling, Phys. Rev. C22 (1980) 1594.

GRE 83 R.E.L. Green, R.G. Korteling, and K.P. Jackson, TRIUMF Report No. TRI-PP-83-118 (unpublished).

GRO 82 D.H.E. Gross, L. Satpathy, Meng Ta-Chung, and M. Satpathy, Z. Physik A309 (1982) 41.

GUD 79 K.K. Gudima and V.D. Toneev, Joint Institute for Nuclear Research Preprint E2-12621 Dubna (1979).

HIR 84 A.S. Hirsch, A. Bujak, J.E. Finn, L.J. Gutay, R.W. Minich, N.T. Porile, R.P. Scharenberg, B.C. Stringfellow, and F. Turkot, Phys. Rev. C29 (1984) 508.

HÜF 84 J. Hüfner, Max Planck Institute Preprint MPI-1984-V32 (1984).

JAQ 83 H.R. Jaqaman, A.Z. Mekjian, and L. Zamick, Phys. Rev. C27 (1983) 2782.

JAQ 84 H.R. Jaqaman, A.Z. Mekjian, and L. Zamick, Phys. Rev. C29 (1984) 2067.

KNO 84 J. Knoll and B. Strack, GSI Preprint GSI-84-66 (1984).

KRU 83 H. Kruse, private communication.

LOP 84 J.A. Lopez and P.J. Siemens, Texas A & M Preprint (1984).

MAR 70 J.B. Marion, Classical Dynamics of Particles and Systems (Academic Press, London and New York, 1970), 292-307.

MEK 81 A.Z. Mekjian and S. Das Gupta, Phys. Rep. 72C (1981) 133.

MIN 82 R.W. Minich, S. Agarwal, A. Bujak, J. Chuang, J.E. Finn, L.J. Gutay, A.S. Hirsch, N.T. Porile, R.P. Scharenberg, B.C. Stringfellow, and F. Turkot, Phys. Lett. 118B (1982) 458.

MOR 84 D.J. Morrissey, W. Benenson, E. Kashy, B. Sherrill, A.D. Panagiotou, R.A. Blue, R.M. Ronningen, J. van der Plicht, and H. Utsunomiya, Phys. Lett. 148B (1984) 423.

MOR 85 L.G. Moretto, M.A. McMahan, L.G. Sobotka, and G.L. Wozniak, LBL Preprint LBL-19030 (1985).

NAG 81 S. Nagamiya, M.C. Lemaire, E. Moeller, S. Schnetzer, G. Shapiro, H. Steiner, and I. Tanihata, Phys. Rev. C24 (1981) 971.

NOR 80 W. Norenberg and H.A. Weidenmuller, Introduction to the Theory of Heavy Ion Collisions (Springer-Verlag, 1980) 44.

PAN 84 A.D. Panagiotou, M.W. Curtin, H. Toki, D.K. Scott, and P.J. Siemens, Phys. Rev. Lett. 52 (1984) 496.

PAN 85 A.D. Panagiotou, M.W. Curtin, and D.K. Scott, Phys. Rev. C31 (1985) 55.

POC 85 J. Pochodzalla, W.A. Friedman, C.K. Gelbke, W.G. Lynch, M. Maier, D. Ardouin, H. Delagrange, H. Doubre, C. Gregoire, A. Kyanowski, W. Mittig, A. Peghaire, J. Peter, F. Saint-Laurent, Y.P. Viyogi, B. Zwieglinski, G. Bizard, F. Lefebvres, B. Tamain, and J. Quebert, Phys. Lett. 161B (1985) 275.

POS 71 A.M. Poskanzer, G.W. Butler, and E.K. Hyde, Phys. Rev. C3 (1971) 882.

PRE 75 M.A. Preston and R.K. Bhaduri, Structure of the Nucleus (Addison-Wesley, MA, 1975) 505.

RÖP 82 G. Röpke, L. Münchow, and H. Schulz, Phys. Lett. B112 (1982) 13.

SAN 84 H.J. Sann, Proceedings of Workshop: 7th Heavy Ion Study, GSI, Darmstadt (Oct. 8-12, 1984).

SAU 76 G. Sauer, H. Chandra, and U. Mosel, Nucl. Phys. A264 (1976) 221.

SCH 83 H. Schulz, D.N. Voskresensky, and J. Bondorf, Phys. Lett. 133B (1983) 141.

SCO 80 D.K. Scott, Progress in Particle and Nuclear Physics 4 (1980) 5.

SCO 81 D.K. Scott, Dynamics of Heavy Ion Collisions, ed. N. Cindro, R.A. Ricci, and W. Greiner (North-Holland, Amsterdam, 1981) 241.

SER 80 F. Serr, G.F. Bertsch, and J.P. Blaizot, Phys. Rev. C22 (1980) 922.

SIE 83 P.J. Siemens, Nature (London) 305 (1983) 410.

SOB 85a L.G. Sobotka and L.G. Moretto, Phys. Rev. C31 (1985) 668.

SOB 85b L.G. Sobotka, M.A. McMahan, R.J. McDonald, C. Signarbieux, G.J. Wozniak, M.L. Padgett, J.H. Gu, Z.H. Liu, Z.Q. Yao, and L.G. Moretto, Phys. Rev. Lett. 53 (1984) 2004.

SPI 82 H. Spieler, IEEE Transaction on Nucl. Sci., Vol. NS-29 (1982) 1142.

STA 79 D. Stauffer, Phys. Rep. 54C (1979) 1.

STO 81 H. Stoecker, Lawrence Berkeley Laboratory Preprint LBL 02302 (1981).

STR 84 B. Strack and J. Knoll, Z. Phys. A315 (1984) 249.

TRO 85 R. Trockel, K.D. Hildenbrand, U. Lynen, W.F.J. Mueller, H.J. Rabe, H. Sann, H. Stelzer, R. Wada, N. Brummund, R. Glasow, K.H. Kampert, R. Santo, D. Pelte, J. Pochodzalla, and E. Eckert, GSI Preprint GSI-85-45 (1985).

VIC 84 A. Vicentini, G. Jacucci, and V.R. Pandharipande, University of Illinois Preprint ILL-(NU)-84-50 (1984).

WES 78 G.D. Westfall, R.G. Sextro, A.M. Poskanzer, A.M. Zebelman, G.W. Butler, and E.K. Hyde, Phys. Rev. C17 (1978) 1368.

WES 82 G.D. Westfall, B.V. Jacak, N. Anantaraman, M.W. Curtin, G.M. Crawley, C.K. Gelbke, B. Hasselquist, W.G. Lynch, D.K. Scott, B.M. Tsang, M.J. Murphy, T.J.M. Symons, R. Legrain, and T.J. Majors, Phys. Lett. 116B (1982) 118.

WES 83 G.D. Westfall, Z.M. Koenig, B.V. Jacak, L.H. Harwood, G.M. Crawley, M.W. Curtin, C.K. Gelbke, B. Hasselquist, W.G. Lynch, A.D. Panagiotou, D.K. Scott, and H. Stoecker, MSU Preprint MSUCL-428 (1983).

YOU 81 D.H. Youngblood, P. Bogucki, J.D. Bronson, U. Garg, Y.W. Lui, and C.M. Rozsa, Phys. Rev. C23 (1981) 1997.

ZAM 73 L. Zamick, Phys. Lett. 45B (1973) 313.